SELÇUK ÜNİVERSİTESİ
FEN BİLİMLERİ ENSTİTÜSÜ

SELÇUK
ÜNİVERSİTESİ

T.C.

SELÇUK UNIVERSITY
THE GRADUATE SCHOOL OF NATURAL SCIENCES

PRODUCTION OF ALKALI ATOMS DOPED Cu_2SnS_3 NANOPARTICLES THIN FILMS BASED SOLAR CELLS USING PULSED LASER DEPOSITION SYSTEM

Amina HOUIMI

Ph.D. THESIS
Department of Nanotechnology and Advanced Materials

Sebtember-2022
KONYA
© All Rights Reserved

TEZ BİLDİRİMİ

Bu tezdeki bütün bilgilerin etik davranış ve akademik kurallar çerçevesinde elde edildiğini ve tez yazım kurallarına uygun olarak hazırlanan bu çalışmada bana ait olmayan her türlü ifade ve bilginin kaynağına eksiksiz atıf yapıldığını bildiririm.

DECLARATION PAGE

I hereby declare that all information in this document has been obtained and presented in accordance with academic rules and ethical conduct. I also declare that, as required by these rules and conduct, I have fully cited and referenced all material and results that are not original to this work.

İmza

Amina HOUIMI

Tarih: 08.09.2022

ÖZET

DOKTORA TEZİ

PULS LAZER DEPOZISYON TEKNİĞİ KULLANILARAK ALKALİ ATOMLARININ DOPİNG EDİLDİĞİ Cu_2SnS_3 NANOPARÇACIK İNCE FİLME DAYALI GÜNEŞ PİLLERİNİN ÜRETİMİ

Amina HOUIMI

Selçuk Üniversitesi Fen Bilimleri Enstitüsü
Nanoteknoloji ve İleri Malzemeler Anabilim Dalı

Danışman: Prof. Dr. Hamdi ŞÜKÜR KILIÇ

2022, 140 Sayfa

Jüri
Prof. Dr. Hamdi ŞÜKÜR KILIÇ
Prof. Dr. Bedrettin MERCİMEK
Dr. Öğr. Üyesi Serap YİĞİT GEZGİN
Dr. Öğr. Üyesi Niğmet KÖKLÜ
Dr.Öğr.Üyesi Yasemin GÜNDOĞDU

İnce film tabanlı güneş pilleri için yüksek performanslı, düşük maliyetli ve toksik olmayan elementlere sahip, soğurgan tabakaların geliştirilmesi günümüzde modern çalışmaların ana odak noktası durumundadır. Bu tez çalışmasında, Pulsed Lazer Depozisyon (PLD) tekniği kullanılarak farklı katkılı atomlar ve konsantrasyonları ile Cu_2SnS_3 (CTS) sputter targetler üretilmiştir. Biriktirmede kullanılan hedef, saf toz yapıdaki bakır, kalay ve kükürt numuneler kullanılarak Ball Milling yönteminde öğütülerek karıştırılmış ve devamında. Ortaya çıkan toz karışım preslenerek küçük hedef yapılar üretilmiştir. CTS hedeflerin yapısı üzerinde sıcaklık etkisi incelenmiş ve bu analiz çalışmaları için üretilen hedef yapılar farklı sıcaklıklarda tavlanarak karakterize edilmiştir. 600°C tavlama sıcaklığının CTS hedef yapıları için en uygun sıcaklık olduğu tespit edilmiştir. CTS ince filmlerinin biriktirme işlemi, farklı biriktirme süreleriyle oda sıcaklığında PLD sistemi kullanılarak gerçekleştirilmiş ve ardından filmler, 400°C ile 600°C arasında değişen sıcaklıklarda sülfürizasyon işlemine tabi tutulmuştur. CTS ince filmlerin çeşitli morfolojik, optik, kristal özellikleri ve kompozisyonu üzerinde sülfürizasyon sıcaklığının ve kalınlığının etkileri üzerinde derinlemesine araştırma yapılmıştır. Sülfürizasyon sıcaklığının genel etkisi, üçlü Cu-Sn-S fazları ile amorf yapıdan polikristal yapıya CTS kristal yapısının iyileştirilmesi ve S atomu katılımının artması gerçekleşmiştir. Ancak sıcaklığın yüksek olması, CTS ince filmlerin yapısında ikincil fazların oluşmasına neden olarak olumsuz etki yapmıştır. Biriktirme süresinin yükselmesi, ince filmlerin farklı özelliklerini etkileyen kalınlığı arttırmıştır. CTS ince filmlerinin farklı alkali (Li, Na) atomlar ile katkılanması, farklı özellikler ortaya koymuştur. Burada katkılama işlemi sadece kristal özelliğini, kompozisyonunu ve morfolojisini değil, aynı zamanda CTS ince filmlerinin kalınlığını da etkilediği görülmüştür. Na katkısı kristalleşme özelliğini arttırırken, Li elementinin katkılanması CTS ince filmlerin biriktirme oranını azaltıcı bir etkiye sahip olduğu tespit edilmiştir. n-Si wafer üzerinde büyütülen CTS ince filmleri, bir PN heteroeklem yapısı oluşturmuş ve bu yapının karanlık ve aydınlatmadaki özellikleri detaylı olarak incelenmiştir. Al/n-Si/CTS/Ag yapısı ile Na ve Li atomlarının farklı doping konsantrasyonlarına sahip olacak şekilde hazırlanan güneş pilleri, Na ve Li elementlerinin ince filmlerin farklı özellikleri üzerindeki etkisinden dolayı performansında gelişme göstermiştir. Na ve Li atomlarının farklı konsantrasyon oranlarına sahip güneş pillerinin tüm farklı parametreleri incelenmiştir.

Anahtar Kelimeler: Alkali doping, Cu_2SnS_3, güneş pilleri, PLD, p tipi yarı iletkenle

ABSTRACT

Ph.D THESIS

PRODUCTION OF ALKALI ATOMS DOPED Cu_2SnS_3 NANOPARTICLES THIN FILMS BASED SOLAR CELLS USING PULSED LASER DEPOSITION SYSTEM

AMINA HOUIMI

THE GRADUATE SCHOOL OF NATURAL AND APPLIED SCIENCE OF SELÇUK UNIVERSITY
THE DEGREE OF DOCTOR OF PHILOSOPHY
IN NANOTECHNOLOGY AND ADVANCED MATERIALS

Advisor: Title Prof. Dr. Hamdi ŞÜKÜR KILIÇ

2020, 140 Pages

Jury
Prof. Dr. Hamdi ŞÜKÜR KILIÇ
Prof. Dr. Bedrettin MERCİMEK
Dr. Öğr. Üyesi Serap YİĞİT GEZGİN
Dr. Öğr. Üyesi Niğmet KÖKLÜ
Dr.Öğr.Üyesi Yasemin GÜNDOĞDU

The development of high-performance and earth abundant absorber layer for thin films based solar cells is the main focus nowadays. In this thesis we produced Cu_2SnS_3 (CTS) with different doping atoms and concentrations using pulsed laser deposition technique. The target used in the deposition were prepared using ball milling from; copper, tin and sulfur powders. The resulted powder was pressed into small target and annealed at different temperatures to analyze the effect of the temperature on the structure of CTS targets. It was found that 600°C annealing temperature is the most suitable one for CTS targets. The deposition of CTS thin films was held using PLD system at room temperature with different deposition durations and then the films were exposed to sulfurization treatment at temperatures ranging from 400°C to 600°C. In-depth research was done on the impacts of sulfurization temperature and thickness on the various morphologic, optical structural, and composition aspects of CTS thin films. The overall effect of sulfurization temperature was the improvement of CTS crystallinity from amorphous to polycrystalline structure with ternary Cu-Sn-S phases and the increase of S atom incorporation. However, high temperature showed a negative effect by the formation of secondary phases in CTS thin films structure. The elevation of the deposition time increased the thickness that effected the different properties of the thin films. Doping the CTS thin films with different alkali atoms (Li, Na) element resulted in diverse outcome, where the doping influence not only the crystallinity, composition and morphology but also the thickness of CTS thin films. Na doping enhanced the crystallinity while Li incorporation had a dramatic influence of reducing the deposition rate of CTS thin films. The CTS thin films grown on n-Si wafer formed a PN heterojunction structure and the properties of this structure in darkness and illumination were investigated in details. The solar cells prepared with Al/n-Si/CTS/Ag structure with different doping concentration of Na and Li atoms showed some development in its performance due to the influence of Na and Li on the different properties of the thin films such as improving the crystallinity and varying the deposition rate of the doped CTS thin films. All the different parameters of the solar cells with different concentration ratio of Na and Li atoms were studied.

Keywords: Cu_2SnS_3, solar cells, PLD, Alkali doping, ball milling, p type semiconductors

ACKNOWLEDGMENT

First and foremost, I want to say “Alhamdulillah”. I thank and praise Allah SWT, the Almighty, the Most Gracious, and the Most Merciful, for His blessings that help me to accomplish this life project despise all the difficulties. Allah‘s blessings upon His last Prophets “Muhammad” peace be upon him, his family and his companions.

This research accomplishment can never be a solo work and I have a lot of people to express my thanks and gratitude.

I would like to start with my respectful supervisor **Prof. Dr. Hamdi Şükür KILIÇ**, for his unwavering support, assistance and direction during my work with *Laser spectroscopy Group*. He was always there to assist me in all may studies and life matters so I can be a better and dependable academician.

My deepest gratitude is extended to **Dr. Öğr. Üyesi Serap YİĞİT GEZGİN**, who help, supported in each step of my studies and counseled me to never lose hope in achieving my PhD degree. I would also like to thank **Dr. Öğr. Üyesi Yasemin GÜNDOĞDU** for her priceless and wonderful aid and advices. To **Dr. Yavuz EKİNCİOĞLU**, **Sümeyye KILIÇ**, and **Walid BELAID** and all my Friends I express my biggest appreciations for being wonderful colleges and friends.

I would also want to thank a very precious teacher to mine, a person who help me a lot in the beginning of this journey “**Dr. Öğr. Üyesi MEHMET TAŞER**”. My God bless his soul and grand him the highest havens. he will always be in our prayers.

Most importantly, I want to thank and dedicate this work to the precious and the most wonderful parents, *Nacer HOUIMI* and *Safia HABA*. I am very thankful and bless to be your daughter. Your enormous support, help, guidance and prayers is the reason I am here today. *Thank you.* I can’t forget my brothers and sisters, *Salh, Hiba, Doaa, Arbi* and *Zaied* for their endless love and support. To the HOUIMI and HABA family I would like to thank all of you.

Amina HOUIMI
KONYA-2022

TABLE OF CONTENTS

ÖZET iv

ABSTRACT v

ACKNOWLEDGMENT vi

TABLE OF CONTENTS vii

SYMBOLS AND ABBREVIATIONS x

LIST OF EQUATIONS xii

LIST OF FIGURES xiii

LIST OF TABELS xv

1. INTRODUCTION 1

1.1. Overview of world energy production and consumption 1
1.2. The Structure of The Thesis 3
1.3. Thesis SCOPS and Contributions 4

2. LITERATURE REVIEW 6

2.1. Physics of Semiconductors 6
2.1.1. Formation of allowed and forbidden energy bands 6
2.1.2. Distinction between metal, semiconductor and insulator 7
2.1.3. Distinction between metal, semiconductor and insulator 8
2.1.4. N and P type semiconductors 9
2.2. Photovoltaic Effect 10
2.2.1. PN junction 10
2.2.2. PV effect and solar cells 11
2.2.3. Solar cells parameters 13
2.3. Different Generations of Solar Cells 16
2.3.1. 1st generation 16
2.3.2. 2nd generation 17
2.3.3. 3rd generation 19
2.4. Chalcogenides Semiconductors 20
2.4.1. CIGS 20
2.4.2. CZTS 21
2.5. Cu_2SnS_3 (CTS) 23
2.5.1. Different properties 23
2.5.2. CTS thin films preparation techniques 27
2.5.3. CTS solar cells history and achievements 30
2.6. Alkaline Atoms Doping Effects 31
2.6.1. CIGS 31
2.6.2. CZTS 33
2.7. Pulsed laser deposition technique 35
2.7.1. History of PLD 35

2.7.2. Introduction to laser ablation technique 36
2.7.3. Laser-target interaction during laser ablation 36
2.7.4. Non-thermal phenomena in the interaction laser beam -material 38
2.7.5. Ejection of condensed particles 39
2.7.6. Advantages and disadvantages of PLD 39

3. MATERIALS AND METHOD 41

3.1. Ball Milling 41
3.1.1. Mechanize of BM 41
3.1.2. Parameters of BM 42
3.1.3. The used Ball milling equipment 43
3.2. Target Production 45
3.2.1. Calcination 45
3.2.2. Uniaxial pressing 45
3.2.3. Sintering 46
3.3. Pulsed Laser Deposition technique 47
3.3.1. The PLD system for CTS thin films deposition 47
3.4. Annealing and preserving Processes 50
3.5. Physical Vapor Deposition (PVD) Technique 51
3.6. Characterization of thin films 54
3.6.1. X-ray diffraction (XRD) 54
3.6.2. Scanning Electron Microscopy (SEM) 55
3.6.3. Energy Dispersive X-ray Spectroscopy (EDX) 56
3.6.4. Raman spectroscopy 56
3.6.5. UV-Visible-NIR spectrophotometry 57
3.6.6. Profilometer 57
3.6.7. Characterization of solar cells (Current Density-Voltage (I-V) Measurement): 58

4. Research Results and Discussion 59

4.1. CTS Powder: 59
4.1.1. Experimental Process 59
4.1.2. XRD: 60
4.2. CTS Targets 61
4.2.1. Experimental process 61
4.2.2. XRD analyze 62
4.2.3. SEM-EDX analyze 64
4.3. Undoped CTS Thin Films (Production and Analyze) 65
4.3.1. Experimental process of undoped CTS thin films 65
4.3.2. Effect of annealing temperature on different properties of CTS thin films 67
4.3.3. Effect of deposition time on different properties of CTS thin films 74
4.4. Na and Li Doped CTS Thin Tilms and Solar Cells Properties 79
4.4.1. Experimental Process of Na and Li doped CTS thin films and solar cells 79
4.4.2. Na Doping effect on CTS thin films 81
4.4.3. Effect of Na doping on the characteristics of SNa1, SNa3 and SNa5 88
4.4.4. Li Doping effect on CTS thin films 93
4.4.5. Effect of Li doping on the characteristics of SLi1, SLi3 and SLi5 98

5. GENERAL CONCLUSION 104

REFERENCES 107

CURRICULUM VITAE (CV) ..... Erreur ! Signet non défini.

SYMBOLS AND ABBREVIATIONS

Symbols

CO_2	Carbon dioxide
%	Percentage
d	Interatomic distance
Å	Angstrom
eV	Electron volt
ΔE	Difference in energy
°K	Kelvin Degree
T	Temperature
Eg	Band gap energy
SC	Semiconductor
n	Concentration of electrons in the conduction band
p	Concentration of holes in the valance band
W	Depletion zone
I_{ph}	Photocurrent
η	Energy conversion efficiency
V_{oc}	Open circuit voltage
I_{sc}	Short circuit current
FF	Fill factor
I_0	Saturation current
q	Charge of the electron
K	Boltzmann constant
m	Ideality factor of the diode
P_M	Maximum power
P_{in}	Incident light power
PECVD	Plasma Enhanced Chemical Vapor Deposition
MOCVD	Metal-organic chemical vapor deposition
a-Si	Amorphous silicon
CdTe	Cadmium telluride
CIGS	$CuIn_xGa_{1-x}Se_2$
CZTS	Cu_2ZnSnS_4
CTS	Cu_2SnS_3
h	Planck constant
ν	Wave frequency
E_{Laser}	Laser photon energy
λ_{Laser}	Laser wavelength
°C	Celsius degree
&	And

List of abbreviations

N	Number of atoms
PV	Photovoltaic
PLD	Pulsed laser deposition
BM	Ball milling
MA	Mechanical alloying
BPR	Ball-to-powder ratio
RPM	Rotation-per-minute

ns	Nanosecond
fs	Femtosecond
EB	Electron Beam
XRD	X-Ray Diffraction
SEM	Scanning Electron Microscopy
EDX	Energy dispersive X-ray
S	Sulfur
Cu	Copper
Sn	Tin
Ar	Argon
SLG	Silica Lime Glass
PDT	Post deposition treatment
AM1.5	Air Mass 1.5

LIST OF EQUATIONS

$Idiode = I0\ expeV/mkT - 1$ **Eq 2. 1** 13
$I = Idiode - Iph = I0\ expeVnkT - 1 - Iph$ **Eq 2. 2** 13
$Voc = KTeLog\ [IphI0 + 1]$ **Eq 2. 3** 14
$FF = PmIsc \times Voc$ = Im × Vm Isc × Voc **Eq 2. 4** 16
$\eta = PmPin = Isc \times Voc \times FFPin$ **Eq 2. 5** 16
$EgCIGSex = EgCIS + 0.626x - bx1 - x$ **Eq 2. 6** 21
$x = GaGa + In$ **Eq 2. 7** 21
$h\nu = ELaser$ **Eq 2. 8** 36
$\nu = c\lambda Laser \quad \Leftrightarrow \quad \lambda Laser = 1240ELaser$ **Eq 2. 9** 37

$VR = 2/3VC$ **Eq 3. 1** 43
$VC = 42.3D - d$ **Eq 3. 2** 43
$D = 0.94\lambda/\beta cos\theta$ **Eq 3. 3** 55
$\delta = 1D2$ **Eq 3. 4** 55
$\varepsilon = \beta cos\theta 4$ **Eq 3. 5** 55
$\alpha = 2.303(A/T)$ **Eq 3. 6** 57
$(\alpha h\upsilon)2 = A(h\upsilon - Eg)$ **Eq 3. 7** 57

$2Cu + Sn + 3S \rightarrow 2CuS + Sn + S$ **Eq 4. 1** 60
$2Cu + Sn + 3S \rightarrow 2CuS + Sn + S \rightarrow Cu2SnS3$ **Eq 4. 2** 63
$I = Is\ expqV/mKT - 1$ **Eq 4. 3** 89
$m = qKTdVdlnI$ **Eq 4. 4** 89

LIST OF FIGURES

Figure 1. 1. *Plot of the changing of carbon dioxide CO_2 concentration in the last two decades (Shaftel, 2022).* *1*
Figure 1. 2. *plot of the changing of surface temperature between in the last century (Shaftel, 2022).* *2*

Figure 2. 1.*A schematic explanation of the mechanize of bands formation in solid materials*..... *7*
Figure 2. 2. *Simplified band diagram of insulator, semiconductor and metal.* *7*
Figure 2. 3. *Simplified band diagram of insulator, semiconductor and metal.* *8*
Figure 2. 4. *Energy band diagram and charge distribution in PN junction before and after contact.* *10*
Figure 2. 5. *Schematic graph of the formation of photocurrent in the basics of PV effect* *12*
Figure 2. 6. *Current-Voltage characteristic of a PN junction-based PV solar cell* *14*
Figure 2. 7. *The variation of Voc according to Iph under high and low $luminous$ flux*..... *15*
Figure 2. 8. *I-V characteristics of solar cell and the position of Vm, Im and PM* *15*
Figure 2. 9. *Based configuration of CIGS solar cells* *18*
Figure 2. 10. *CIGSe crystal lattice (Xue ve ark., 2014)*..... *20*
Figure 2. 11. *Kesterite and stannite structure of CZTS (Vanalakar ve ark., 2015b)* *21*
Figure 2. 12. *Gibbs phase triangle for the system Cu –Sn –S (Fiechter ve ark., 2003)* *23*
Figure 2. 13. *Crystal Structures of CTS; a) Monoclinic b) Tetragonal c) Cubic. Atomic concentration: M1(Cu:56.4%/Sn: 43.6%), M2(Cu: 53.7%/Sn: 46.3%), M3(Cu: 66.7%/Sn: 33.3%) (Shen ve ark., 2016)* *24*
Figure 2. 14. *Density of States of CTS material (Zhai ve ark., 2011)* *25*
Figure 2. 15. *(a) Laboratory Vibratory/shaker mills, (b) Laboratory planetary ball mill and (c) Laboratory attritor mill*..... *30*
Figure 2. 16. *Mechanism of laser matter interaction during laser ablation* *37*

Figure 3. 1. *Schematic image of the mechanical alloying of powders* *41*
Figure 3. 2. *Desk-top high speed vibrating ball mill*..... *44*
Figure 3. 3. *Image of the BM Vial (container) and grinding balls* *44*
Figure 3. 4. *The target shaping system (die and punch)*..... *46*
Figure 3. 5. *Hydraulic Pressing machine* *46*
Figure 3. 6*. Schematic image of PLD system*..... *47*
Figure 3. 7. *The PLD system front view and general design.*..... *48*
Figure 3. 8. *ns- Minilite II (Nd:YAG) laser systems* *49*
Figure 3. 9. *Femtosecond laser system* *50*
Figure 3. 10. *Quartz vacuum oven* *51*
Figure 3. 11. *Vacuum chamber* *51*
Figure 3. 12. *Schematic image of PV system* *52*
Figure 3. 13. *Image of PVD system.* *53*
Figure 3. 14. *Image of XRD analyses system.*..... *54*
Figure 3. 15. *Image of SEM analyze device.*..... *55*
Figure 3. 16. *Images of the different parts of I-V measurement system a) Anode and cathode for data collection, b) Keithley source meter, c) Data accusation interface, d) Solar simulator and e) Light source powering system.* *58*

Figure 4. 1. *Schematic image of CTS powder Ball milling process* *60*
Figure 4. 2. *X-Ray diffraction pattern of CTS powder after ball milling process* *61*
Figure 4. 3*. Schematic image of CTS targets doping and pressing processes* *62*
Figure 4. 4. *X-Ray diffraction pattern of CTS targets after annealing at 600°C and 700°C.*..... *63*
Figure 4. 5. *SEM image of a) the fracture side and b) surface side of same CTS target (TP).* *64*
Figure 4. 6. *A) Images of real CTS target plasma during the deposition and b) schematic plot of PLD system.* *66*
Figure 4. 7. *Schematic image of quartz vacuum oven* *67*
Figure 4. 8.*X-ray diffraction of CTS thin films with different annealing temperatures.* *69*
Figure 4. 9. *SEM images of a1&2) F450, b1&2) F550 and c1&2)F600 CTS thin films..* *70*
Figure 4. 10.*Crystal size and thickness of CTS thin films with different annealing temperatures*..... *71*
Figure 4. 11.*Absorbance spectra of CTS thin films with different annealing temperatures* *72*
Figure 4. 12.*Absorption coefficient of CTS thin films with different annealing temperatures*..... *73*

Figure 4. 13. *Plot of* $(\alpha h\nu)2$ *versus* $h\nu$ *of CTS thin films with different annealing temperatures 74*
Figure 4. 14.*Crystalline size and deposition rate of CTS thin films with deposition rate..... 75*
Figure 4. 15. *X-ray diffraction of CTS thin films with different deposition times 75*
Figure 4. 16. *SEM images of a & b) F5, c & d) F15 CTS thin films..... 77*
Figure 4. 17. *Absorbance spectra of CTS thin films with different deposition times..... 78*
Figure 4. 18. *Plot of* $(\alpha h\nu)2$ *versus* $h\nu$ *of F2.5, F5 and F15 CTS thin films 79*
Figure 4. 19. *Structure of CTS solar cells..... 80*
Figure 4. 20. *X-ray diffraction of CTS thin films with different Na doping concentrations 82*
Figure 4. 21. *a) Crystal size and deposition rate and b) density of dislocations and microstrain of CTS thin films with different Na doping concentrations..... 83*
Figure 4. 22. *Raman plot of FP and FNa1 ..... 84*
Figure 4. 23. *SEM images of a) FP, b) FNa1, c) FNa3 and d) FNa5 thin films in addition of EDX mapping images of e) FP and f) FNa1 ..... 85*
Figure 4. 24. *a) SEM and b) EDX mapping images of FNa1 thin film in relatively small area (2*μ*m scale) 86*
Figure 4. 25. *Absorbance spectra of FP, FNa1, FNa3 and FNa5 thin films..... 87*
Figure 4. 26. *Plot of* $(\alpha h\nu)2$ *versus* $h\nu$ *of FP, FNa1, FNa3 and FNa5 thin films..... 88*
Figure 4. 27. *I-V logarithmic plot of SP, SNa1, SNa3 and SNa5 in darkness..... 90*
Figure 4. 28. *I-V logarithmic plot of SP, SNa1, SNa3 and SNa5 solar cells under 1.5GAM illumination..... 91*
Figure 4. 29. *Boxplot of SP, SNa1, SNa3 and SNa5 solar cells parameters 92*
Figure 4. 30. *X-ray diffraction of CTS thin films with different Li doping concentrations 94*
Figure 4. 31. *a) Crystal size and deposition rate and b) density of dislocations and microstrain of CTS thin films with different Li doping concentrations..... 95*
Figure 4. 32. *SEM images of a) FP, b) FLi1, c) FLi3 and d) FLi5 thin films..... 96*
Figure 4. 33. *Absorbance spectra of FP, FLi1, FLi3 and FLi5 thin films..... 97*
Figure 4. 34. *Plot of* $(\alpha h\nu)2$ *versus* $h\nu$ *of FP, FLi1, FLi3 and FLi5 thin films 98*
Figure 4. 35. *I-V logarithmic plot of SP, SLi1, SLi3 and SLi5 in darkness..... 99*
Figure 4. 36. *I-V logarithmic plot of SP, SLi1, SLi3 and SLi5 solar cells under AM 1.5G. illumination..... 101*
Figure 4. 37. *Boxplot of SP, SLi1, SLi3 and SLi5 solar cells parameters 102*

LIST OF TABELS

Table 3. 1. *ns- Continuum-Surelite III (Nd:YAG) working parameters* *49*
Table 3. 2. *ns- Minilite II (Nd:YAG) working parameters* *49*

Table 4. 1. *The added MF quantities in mole and mg with extended chemical formula of* $M_{0.0x}Cu_2SnS_3$ .. *62*
Table 4. 2. *The atomic concentration of TP target* *65*
Table 4. 3*. List of CTS thin films with the different preparation parameters* *67*
Table 4. 4. *The atomic concentration of CTS thin film and with different sulfurization temperatures.* *68*
Table 4. 5. *The thickness and crystalline size of CTS thin film and with different deposition times* *76*
Table 4. 6. *The atomic concentration of CTS thin film and with different deposition times* *77*
Table 4. 7*. List of Na and Li doped CTS thin films with the preparation parameters* *79*
Table 4. 8. *List of the prepared CTS based solar with the corresponding abbreviations* *81*
Table 4.9. *The atomic concentration of Na doped CTS thin film and target* *83*
Table 4. 10. *The band gap energies, thicknesses and crystalline sizes FP, FNa1, FNa3 and FNa5 thin films* *88*
Table 4. 11. *Electric properties of SP, SNa1, SNa3 and SNa5 solar cells in darkness* *90*
Table 4. 12. *Optoelectric properties of SP, SNa1, SNa3 and SNa5 solar cells under illumination* *91*
Table 4. 13. *The thicknesses and crystalline sizes of FP, FLi1, FLi3 and FLi5 thin films* *95*
Table 4. 14. *The atomic concentration of Li doped CTS thin film* *96*
Table 4. 15. *The band gap energies, thicknesses and crystalline sizes FP, FLi1, FLi3 and FLi5 thin films* ... *98*
Table 4. 16. *Electric properties of SP, SLi1, SLi3 and SLi5 solar cells in darkness* *99*
Table 4. 17. *Optoelectric properties of SP, SLi1, SLi3 and SLi5 solar cells in illumination* *102*

1. INTRODUCTION

1.1. Overview of world energy production and consumption

Nowadays, the modern mankind has access to several energy sources on Earth. The so-called fossil fuel energy (coal, oil, and gas) are the most often utilized for their simple use and relatively affordable price. However, they are a non-renewable and unstable source of energy that result from long processes of transforming biological matter. For various reasons, it turns out that these energies can no longer be used. First of all, fossil energy reserves are starting to dwindle. Subsequently, due to the very strong demand from emerging countries such as China, Brazil and India, etc. The prices of these energies have increased over the last decade, making them unaffordable for some. On the other hand, the non-homogeneity dispersion of these source around the world makes them a very significant cause of conflict and war. Additionally, the climatic changes that have been accruing in the last half century is the most negative and worrying outcome of these energy sources.

While using fossil energies, they emit a large quantity of heat trapping gas CO_2 (carbon dioxide, in particular) or greenhouse gases which is contribute greatly to air pollution and global warming. Figure 1.1 displayed the recent atmospheric CO_2 levels observed at Hawaii's Mauna Loa Observatory after removing seasonal and natural variations (Shaftel, 2022).

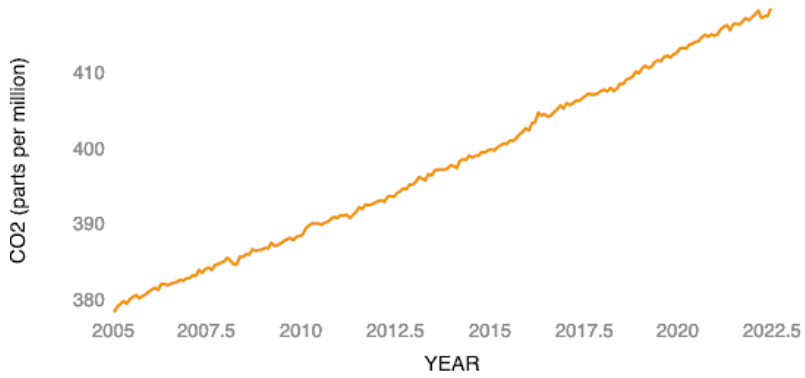

Figure 1. 1. Plot of the changing of carbon dioxide CO_2 concentration in the last two decades (Shaftel, 2022).

The atmospheric CO_2 have increased by rate of 50% since the start of the industrial era (18^{th} century), bringing it to 150% of its original value in 1750. This increase is impacting not only on the air pollution but also on the surface temperature of the earth as we can see in Figure 1.2.

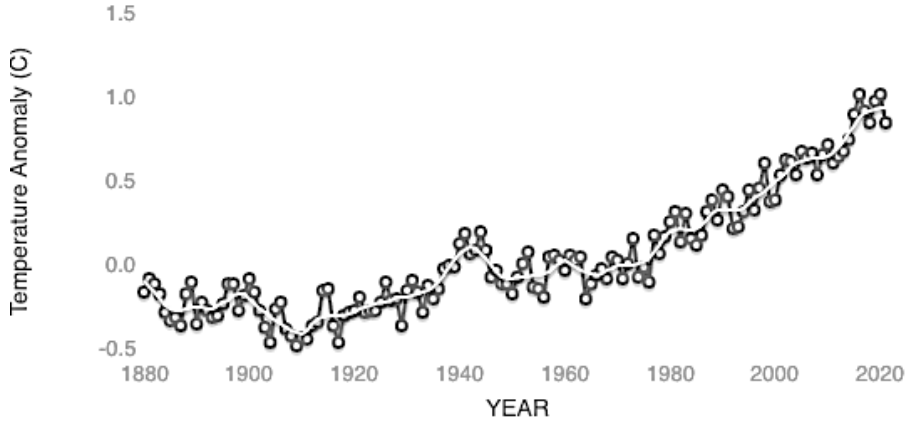

Figure 1. 2. plot of the changing of surface temperature between in the last century (Shaftel, 2022).

This graph displays the shift in the average worldwide surface temperature between 1880 and 2020. The hottest years since 1880 were the years 2016 and 2020.

Moreover, many abundant non-polluting renewable energies are found everywhere which could be exploited by mankind. We can distinct four types of renewable energies: the wind energy, nuclear energy, hydroelectric energy and solar energy. Due to its low energy output per unit of land, wind energy is not sufficiently affordable. Even though nuclear energy has a high yield, the waste it produces is very damaging and difficult to degrade. Moreover, it is frightening because of its previous serious accidents (Chernobyl disaster). Hydroelectric energy has a good yield, but its installation is not available everywhere, and most of the spaces that are favorable to it are already saturated with barrages. Solar energy, it is available everywhere on the surface of the globe, in equal quantity in the year, and has a performance that is improving thanks to the current technology of materials in thin layers (Masson-Delmotte ve ark., 2021). It is becoming easier and easier to exploit. It seems to be the most promising source for the world's energy future.

Huge interest is devoted to solar cell research and industry to cut the fossil fuel addiction and preserve the environment. Thus, in the last 5 centuries, we can say that the humanity managed to produce 3 generation of solar cells with different ups and down. The silicon based solar cells are still in the lead when it comes to the industry despite its rigid form and high cost. The second generation that is based on thin film layers with high-quality absorbance layers. These solar cells consume a very low amount of material which gives them the ability to be deposited at flexible substrates (Wang ve ark., 2014; Kato ve ark., 2019). Unfortunately, the existence of toxic and rare elements in the composition of these solar cells is the most drawback that face the industrialization of this technology. Due to that, numerous research groups are working to develop more earth friendly materials such

as Cu_2ZnSnS_4 and Cu_2SnS_3 and Cd free solar cells. On the other hand, the third-generation solar cells are the fastest developed one with a big research funding all around the world. However, it faces a major obstacle which is the short lifetime of solar cells due to the organic nature of some composing layers. In our present thesis, we are interested in developing a combination between 1st and 2nd generation solar cells with Si/Cu_2SnS_3 heterojunction based solar cells that might be a good based for future Tandem solar cells.

1.2. The Structure of The Thesis

This thesis is composed of five different chapters. The first one is dedicated to introducing our work and descriptive its importance and contribution to the scientific community. The structure of these with its SCOPS was also provided in details.

The second chapter illustrated in brief the most important information as a scientific background for the thesis. Literature review had six different section that were in order: physics of semiconductors, photovoltaic effect, different generations of solar cells, chalcogenides semiconductors, Cu_2SnS_3 (CTS) and Alkali atoms doping effect. In this chapter the required basics of solar cell physics were given along with the most used materials that are investigated such as $CuIn_xGa_{1-x}Se_2$ and Cu_2ZnSnS_4. Finally, we give a relatively profound analyze for CTS material (the used material in the thesis) and the importance of Alkali atoms doping on the solar cells performance since it is the core element of the novelty of our thesis.

3rd chapter was dedicated to the presentation of ball milling and **P**ulsed **L**aser **D**eposition (**PLD**) techniques. In this chapter, we give a brief history of these two techniques and explain the physics behind each one. Then, we present the systems which we used in our experiments with its different parts.

The 4th and the most important chapter provides the results and discussion of all the acquired experimental data. This chapter was sectioned into four parts. The first and second parts present the experimental parameters and the resulted analyses of CTS powders and targets. The 3rd part of this chapter, explains the CTS deposition parameters using PLD technique. On the other hand, the effect of deposition time and sulfurization temperature is given. The doping effect on CTS thin films different properties is sectioned according to the used dopant atom; Li and Na. The last section in this chapter explains the behavior of CTS based solar cells in darkness and under illumination with different dopant atoms and concentration.

The last chapter presents a general conclusion of this thesis.

1.3. Thesis SCOPS and Contributions

This PhD thesis study focuses on the production of CTS (Cu_2SnS_3) thin films for applications in solar cell technology. Our principal goal is to improve the conversion efficiency of CTS based solar cells using home-made targets with different alkali atoms doping concentrations. To achieve that, we need to assure the stoichiometric composition and good crystallinity of our thin films. In order to accomplish the objective of our PhD thesis some main aims must be fulfilled:

- The first objective of our thesis is to produce a dense and stoichiometric CTS target for PLD technique using ball milling system. To do so, we have optimized the production parameters of CTS powder and target.
  - ✓ We have produced CTS powder from elemental Cu (Copper), Sn (Tin) and S (Sulfur) powder using wet ball milling while focussing on the particle size reduction. Then, we have analysed the structural and composition properties of CTS powder.
  - ✓ The next aim is the uniaxial pressing of CTS powder. To do so, we have formed a green target then sintering this CTS target at different temperatures. After that, we have to study its structural and composition properties according to the used temperature.
  - ✓ After the production of a suitable and pure CTS target, the next aim is to introduce four different alkali atoms as dopants to the target with dissimilar concentrations.
- The second main aim in our work is to study the non-doped CTS thin film according to the PLD deposition time duration and sulfurization temperature by analysing its properties. CTS thin films with different four deposition duration and five sulfurization temperatures were produced, and all their structural, optical, morphological and compositional properties were provided and discussed.
- After a good analysis of temperature and deposition time effects on CTS thin films properties, the next step is to use the best CTS thin film parameters with 10 min deposition time and 500°C sulfurization temperature to produce alkali atoms doped CTS thin films with different doping concentrations. For each atom (Li, Na) the properties all thin films were analysed and discussed in details according to the doping concentrations.

- Our last objective in this thesis is to develop alkali doped and non-doped CTS thin films based solar cells using n-type Si wafer (Al/Si/CTS/Ag). The effect of introducing Na and Li atoms with various concentration into CTS based solar cells is investigated in details at darkness and under illumination.

The results of our thesis are expected to have a very important value in the academic research community by providing a very original data concerning the development of a CTS based heterojunction solar cells. The number of the researches concerning CTS material remains poor compare to CZTS even though it presents a very good theoretical optical conversion efficiency of 30% (Avellaneda ve ark., 2010). Our work definitely enriches and provide new aspects for this material. On the other hand, introducing the doping martials into the precursor is an untraditional way for doping with alkali atoms. As a consequence, new outcomes are expected in comparing to other traditional doping ways such as post-deposition treatments. Additionally, we can see the effect of the doping atoms and different concentrations on the performance of Al/Si/CTS:Na,Li/Ag solar cells. The properties of these diodes in darkness and under illumination are a good research material for future development of tandem solar cells. Furthermore, the structure of these solar cells can be considered as a combination between the 1^{st} and 2^{nd} generation solar cells.

2. LITERATURE REVIEW

In this chapter we have provided a state of art for this thesis, where the necessary information and background is given in simplified way.

2.1. Physics of Semiconductors

In order to understand the phenomena and physics behind the generation of electric power in solar cells devices we need to go back to the origins of semiconductors.

2.1.1. Formation of allowed and forbidden energy bands

The electrons in an isolated atom (the interatomic distance (d) between two neighbor atoms is wide) are bound to materials and they can only occupy some certain discrete energy states. The outer shell electrons are relatively weakly bound to nucleus and are called valence electrons. They come into participation in chemical reactions as well as in the electrical conduction of metallic and semi-conductor materials.

In solid materials, when the d is being small (a few Å), the atoms can no longer be considered as isolated. As a result, interactions of electrostatic nature between electronic orbitals occur and the crystal becomes an electronic system which must obey the Pauli exclusion principle. According to Pauli exclusion principle, it is impossible to find 2 electrons at the same quantum state of energy level. If we consider for example an atomic system with *N* atomic number, each level must split into *N* levels until the formation of continuous energy bands ($\Delta E \sim 10^{-23}$ eV) for *N* sufficiently large.

The interatomic distance (d) is an important factor that control the electronic structure of material. In case of silicone material, when d is large enough, the electronic structure remains the same as in an isolated atom (case I of Figure 2.1). However, if d becomes weak, we witness a splitting of energy levels until the formation of 3s 3p bands with 2*N* states and 6*N* states respectively as in case II of Figure 2.1. On the hand, if d becomes even lower, then the interactions will be stronger with overlapping and splitting of the bands into two of 4*N* states in each one. Additionally, we notice that the appearance of a band does not include any possible state which is band gap or the forbidden energy band (Nelson, 2003; Sze, 2008).

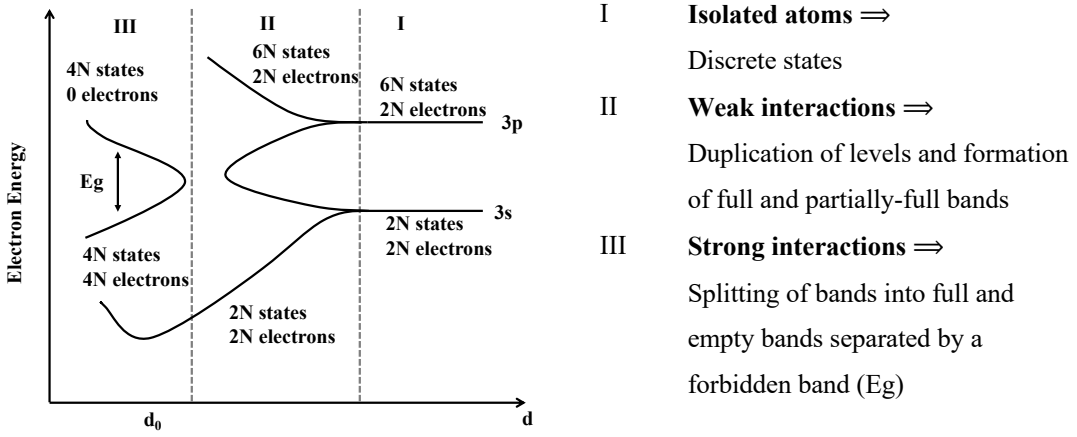

Figure 2. 1.A schematic explanation of the mechanize of bands formation in solid materials

2.1.2. Distinction between metal, semiconductor and insulator

According to the band diagram (Figure 2.2) of material and theirs overlapping we can distinguish the crystals into three different categories: metals, semiconductors and insulators. This is a result of the dissimilarity in their lattice parameter and inter-atomic distance. The band gap of semiconductors is the primary material feature which distinguishes semiconductors from other groups of materials. In semiconductors, the band gap lies in between metals and insulators.

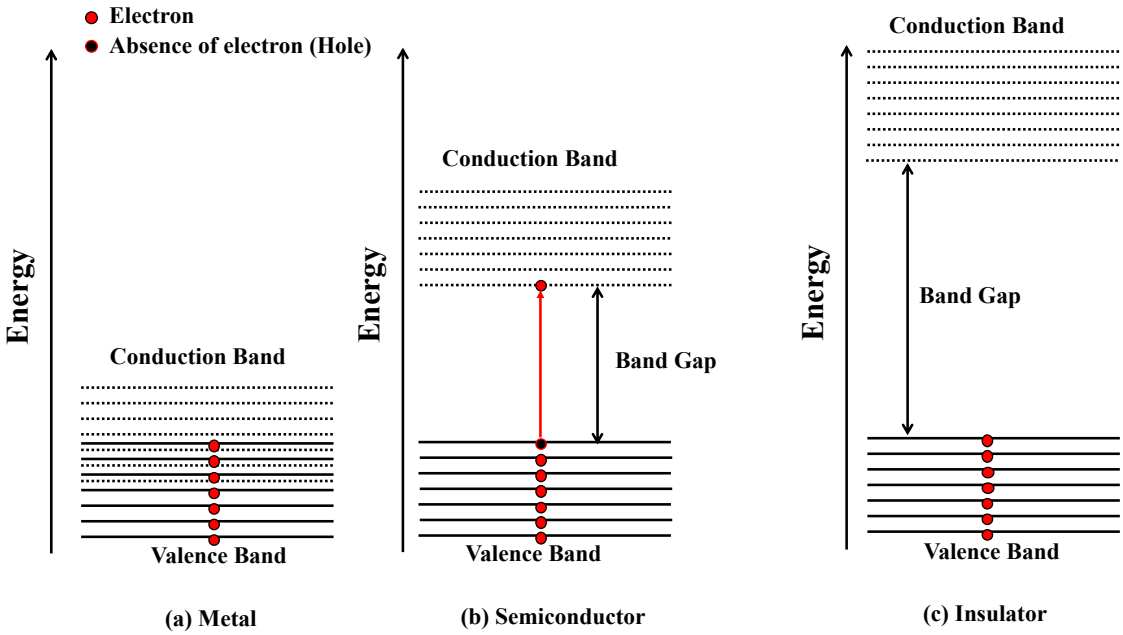

Figure 2. 2. Simplified band diagram of insulator, semiconductor and metal.

A metal (see Figure 2.2 a) is characterized by a partially filled band where electrons can easily move to higher energy levels and thus move around and conduct electricity. Metal is a conductor even at 0°K. However, a semiconductor (SC) (see Figure 2.2 b) is an insulator at 0°K, because its bands are either full or empty. Under normal temperature conditions (T = 300°K), the semiconductor of E_g (Band gap energy) less than 5.18 eV tends to have electric conductivity due to thermal emission that makes it possible to partially populate the upper band. For an insulator with E_g larger than 5.18 eV(see Figure 2.2 c), thermal emission is enabled to populate the empty higher energy band and therefore the energy bands remain empty or full (Nelson, 2003; Sze, 2008).

2.1.3. Distinction between metal, semiconductor and insulator

According to the band diagram (Figure 2.2) of material and theirs overlapping we can distinguish the crystals into three different categories: metals, semiconductors and insulators. This is a result of the dissimilarity in their lattice parameter and inter-atomic distance. The band gap of semiconductors is the primary material feature that distinguishes semiconductors from other groups of materials. In semiconductors, the band gap lies in between metals and insulators.

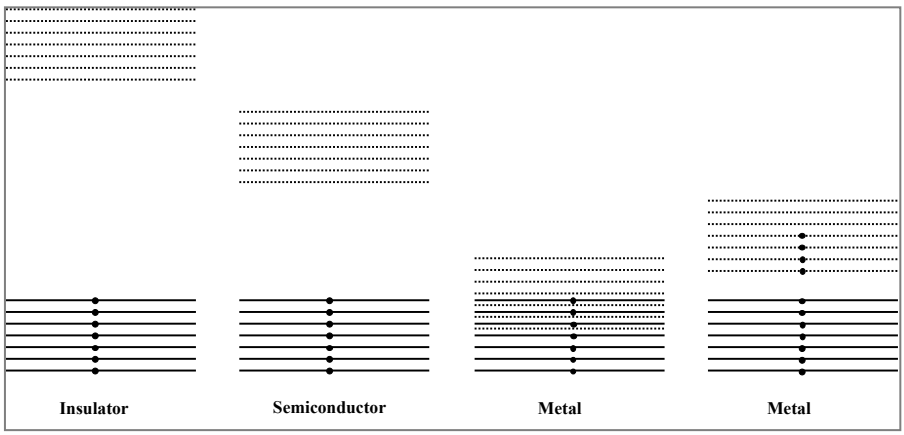

Figure 2. 3. Simplified band diagram of insulator, semiconductor and metal.

A metal is characterized by a partially filled band where electrons can easily move to higher energy levels and thus move around and conduct electricity. Metal is a conductor even at 0°K. However, a semiconductor (SC) is an insulator at 0°K, because its bands are either full or empty. Under normal temperature conditions (T = 300°K), the semiconductor of E_g (Band gap energy) less than 5.18 eV tend to have electric

conductivity due to thermal emission that makes it possible to partially populate the upper band. For an insulator with E_g larger than 5.18 eV, thermal emission is enabled to populate the empty higher energy band and therefore the energy bands remain empty or full(Nelson, 2003; Sze, 2008).

2.1.4. N and P type semiconductors

SCs can be divided into two categories intrinsic and extrinsic. A semiconductor is said to be intrinsic when it has no physical or chemical defects. Its structure has no vacancies, no dislocations, or any type of impurities in its lattice. Experimentally, there always be a certain number of defects or impurities in the material despite the synthesizing methods, and the intrinsic SC represents in fact an ideal borderline case. However, real undoped semiconductor crystals of good crystallographic quality can be considered as intrinsic semiconductor. The intrinsic SC have a small concentration of free charge carriers that results in low electric conduction (Nelson, 2003).

To enhance the electric conduction of SC, doping is very important approach that can introduce new energy levels to the band gap near the maximum of the valance band or near the minimum of the conduction band. These second category is called extrinsic semiconductors. At thermodynamic equilibrium, the concentration of electrons 'n' in the conduction band is different from the concentration of holes 'p' in the valance band in extrinsic SC. This difference is mostly obtained by intentionally introducing a low concentration of impurities with a controlled nature into the material. This addition is called doping. This feature has a considerable influence on the properties of semiconductors. For example, adding one atom of boron per 10^5 atoms of silicon increases the conductivity of silicon by a factor of 10^3 at room temperature (Würfel ve Würfel, 2016).

The electric conduction in semiconductors is due to two types of charge carriers, negative charger "electron" and positive charges "holes" that represent the absence of electron. In N-type SC the concentration of electrons is higher than the concentration of holes and the opposite is the case in P-type SCs where the concentration of holes is higher than the concentration of electrons (Sze, 2008).

2.2. Photovoltaic Effect

It is known that the function of solar cells is based on photovoltaic (PV) effect. Therefore, in this section we explain the basic structure of solar cells and the origin of PV effect.

2.2.1. PN junction

Bringing two semiconductors of different doping types (N and P) into contact leads to a so-called PN junction. This has the direct effect of moving charges from one side of the junction to the other side (Würfel ve Würfel, 2016).

In N-type SC the fermi level is close to the conduction band, while it is close to the valance band in P-type SC. When the two types of SC are rejoined together, the fermi levels will tend to align while conduction and valance bands will bend to reach equilibrium state. The bent of band region represents the depletion zone (W) (see Figure 2.3). The formation of W is rolled by two different phenomena; diffusing and drifting of charges (Belaqziz ve ark., 2018). The contact will allow the charges to diffuse from the regions of high concentration to the region of low concentration of free charges. The majority free electrons will diffuse from the N type to the P type SC.

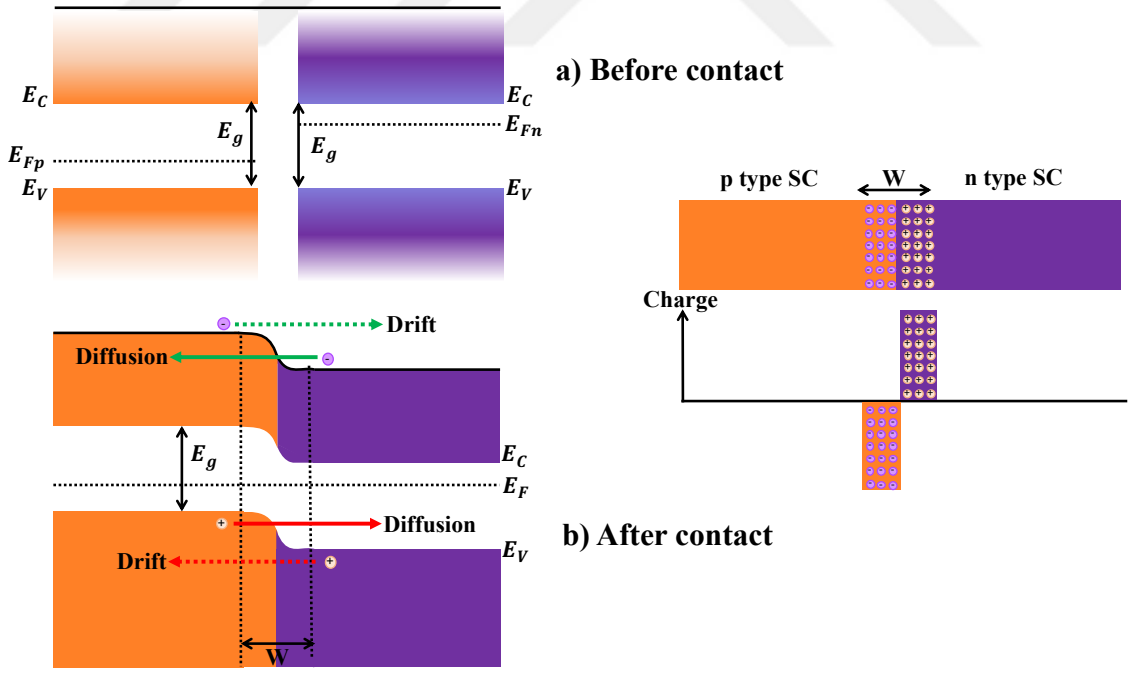

Figure 2. 4. Energy band diagram and charge distribution in PN junction before and after contact.

The free electron is then recombined with a hole on the P doped region, leaving behind a positively ionized donor atom on the N-doped region. On the other hand, a diffusion of

the majority free holes of P-type towards N-type SCs will happen. The hole tends to recombine with a free electron on the N-doped region, leaving behind a negative acceptor atom ionized on P-doped region (see Figure 2.3). These fixed ionized atoms generate an internal electric field that increases until it reaches a value which will stop the movement of charges due to an excessively high potential barrier. This electric field opposes the diffusion current by the generation of a drift current (Bisquert, 2017; Guitouni ve Attaf, 2017; Belaqziz ve ark., 2018).

In the depletion zone (W), atoms are ionized by the departure of the free charges. Its width depends on the concentration of the doping in SC and it decreases when the dopant concentration increases. The electric potential formed in the depletion zone is called the potential of the internal electric field or built-in potential (Guitouni ve Attaf, 2017).

In PN junction, two distinct cases of joining can exist. We call a homojunction when the N-type and P-type semiconductor materials are of the same nature. An example is the case of silicon-based PV solar cells. Otherwise, we speak of a heterojunction when associating two semiconductor materials of different nature (case of the majority of PV solar cells in thin layers) (Nelson, 2003; Belaqziz ve ark., 2018).

2.2.2. PV effect and solar cells

When a semiconductor is under illumination or a source of light, a very well-known phenomenon takes place that is called the PV effect. When a solar cell (PN junction) is illuminated, the emitted photons are absorbed by the semiconductor materials. When the energy of the photon is greater than the energy of the forbidden band of the semiconductor, an electron from valence band promotes up to conduction band leaving a positively charged absence of a particle (hole) behind, then an electron-hole pair (photocarriers, or charge carriers) is formed. The separation of an electron and a hole due to excitation energy is not infinite, and these charges can recombine. A Schematic graph of the formation of photocurrent in the basics of PV effect.

The free charge carriers are generated in the N and P zones and in the depletion zone. Depending on each zone, photo-carriers behave differently:

- In N or P zones, the photo-generated minority carriers are generated by incident photons ($h\nu_1$) and ($h\nu_3$) will arrive at the depletion region and they are propelled by electric field into P zone (in the case of holes) or into N zone (in the case of electrons) where they become majority carriers. In this case, we have a diffusion

photocurrent. In these zones, the recombination of electron and holes takes place far from the depletion region due to the existence of free charges.

- In the depletion region, electrons and holes generated by incident photons ($h\nu_2$) are separated by the internal electric field. In this zone, electrons and holes are accelerated towards N and P region, respectively. In this case, the generation photocurrent appeared.

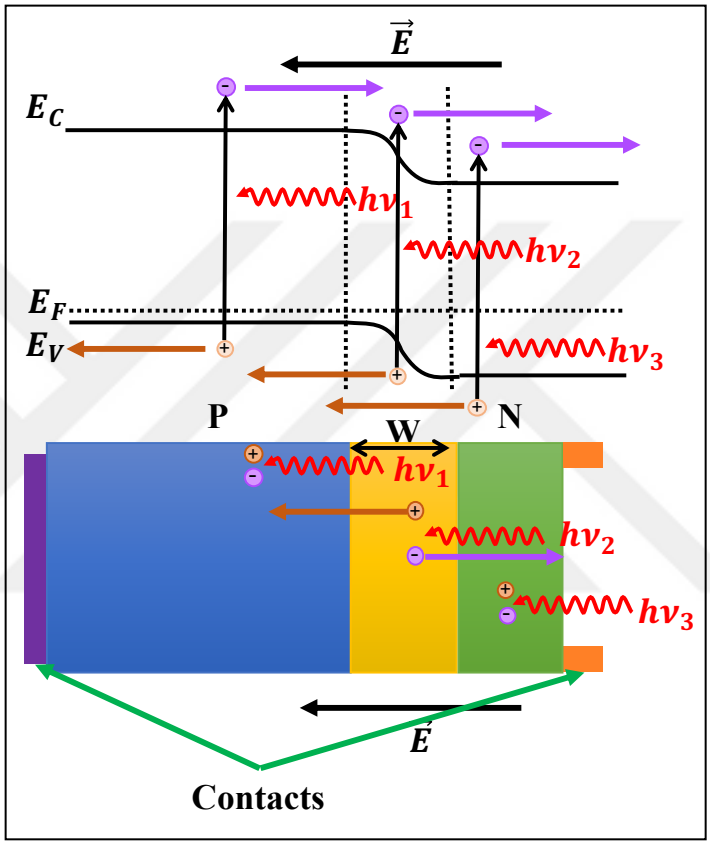

Figure 2. 5. Schematic graph of the formation of photocurrent in the basics of PV effect

These two contributions add up to create a resultant photocurrent I_{ph} which is a current proportional to the flux of the absorbed light (see Figure 2.4).

In summary, it should be noted that the conversion of solar radiation into electricity by a PV cell can only occur if and only if three physical phenomena have taken place:

i. Absorption of as many photons as possible.
ii. The transformation of the absorbed energy into free charge carriers.
iii. Collection of free charge carriers with the least loss to an external electrical circuit.

To extract PV parameters and characteristic of a solar cell; the latter is subjected to artificial solar illumination using a simulator. These measurements are generally carried out under an illumination corresponding to an Air Mass 1.5 (AM1.5) solar spectrum and an incident irradiation power of 100 mW/cm² at 25°C. The AM1.5 spectrum is defined as the solar spectrum received at the earth's surface at an incidence degree of 48.2° (Nelson, 2003; Bisquert, 2017; Belaqziz ve ark., 2018).

2.2.3. Solar cells parameters

A PV cell is characterized by a defined data from the observation of its I-V characteristics under illumination. From these characteristics, we can extract their energy conversion efficiency η, open circuit voltage V_{oc}, short circuit current I_{sc} and fill factor FF. We explained these terms in the following paragraphs.

2.2.3.1. Current/Voltage characteristic and equivalent diagram

Figures 2.5 represents the I-V characteristic of a PN junction based photovoltaic solar cell. As mentioned in previous paragraph, the photocurrent consists of a current of electrons collected by the cathode and a current of holes collected by the anode. In the case of an ideal solar cell, this photocurrent can be assimilated to an ideal source of current that is directed in the opposite direction of diode characteristic in the dark, as it is shown in the graph a, b and c of Figure 2.5.

For an ideal case, I-V curve obeys the following diode equation in the darkness:

$$I_{diode} = I_0\,[exp(eV/mkT) - 1] \qquad \textbf{Eq 2. 1}$$

where I_0 is the saturation current, q is the charge of the electron, K is Boltzmann constant, T is the temperature and m is the ideality factor of the diode. The latter takes recombinations into account. Under illumination, the generated photocurrent I_{ph} is added. We get the following equation:

$$I = I_{diode} - I_{ph} = I_0\left[exp\left(\frac{eV}{nkT}\right) - 1\right] - I_{ph} \qquad \textbf{Eq 2. 2}$$

In the case of a real PV cell, other parameters must be taken into account such as resistive effects, recombinations, leakage at the edges and contacts. The equivalent circuit is shown in d, e and f of Figure 2.5 by a current generator, a diode and two resistors R_s and R_{sh}. R_s is the series resistance that related to the volume resistivity.

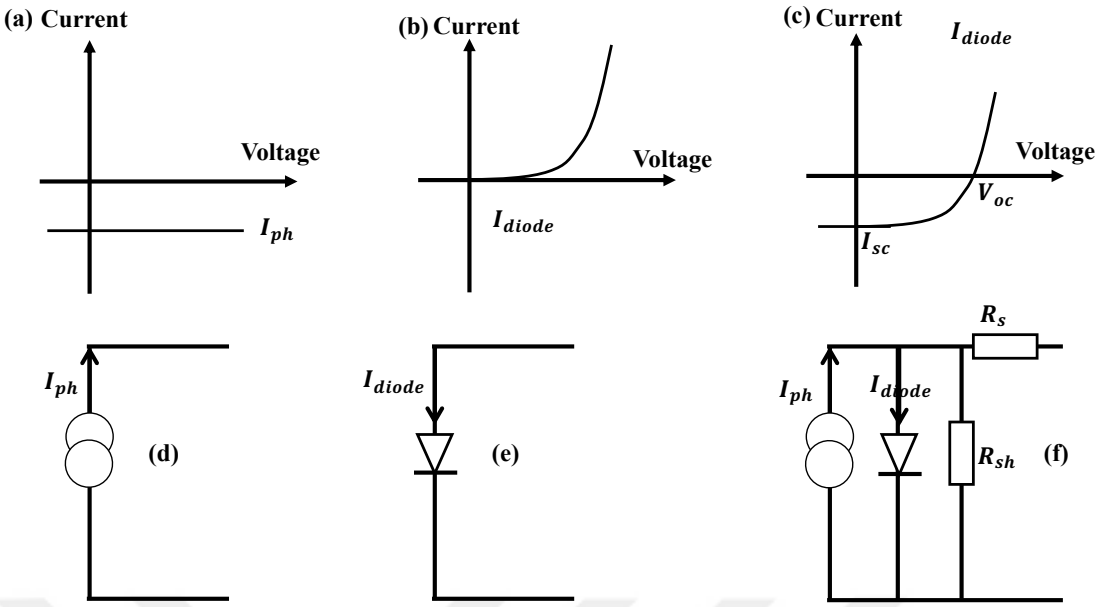

Figure 2. 6. Current-Voltage characteristic of a PN junction-based PV solar cell

2.2.3.2. Open circuit voltage (V_{oc})

The open circuit voltage is by definition: the voltage at the terminals of the photovoltaic cell under open circuit illumination. It essentially depends on the type of solar cell (PN junction, Schottky junction), the materials of the active layers and the nature of the active layer/electrode contacts. It also depends on the illumination of cell. From the expression of the total current of the solar cell under illumination, Equation 2.2 in the case of zero current, we obtain its expression:

$$V_{oc} = \frac{KT}{e} Log\left[\frac{I_{ph}}{I_0} + 1\right] \qquad \textbf{Eq 2. 3}$$

Depending on degree of illumination, two regimes can be observed (Figure 2.6).

- Regime of low luminous flux: in this case, $I_{ph} \ll I_0$, which allows us to write $Log\left[\frac{I_{ph}}{I_0} + 1\right] \simeq \frac{I_{ph}}{I_0}$, hence $V_{oc} = \frac{KT}{e}\frac{I_{ph}}{I_0}$. This is the linear behavior zone of solar cell.
- Regime of high luminous flux: the light fluxes are sufficiently intense for $I_{ph} \gg I_0$, i.e. $\frac{I_{ph}}{I_0} \gg 1$, hence: $V_{oc} = \frac{KT}{e} Log\left[\frac{I_{ph}}{I_0}\right]$. This is the domain of logarithmic behavior.

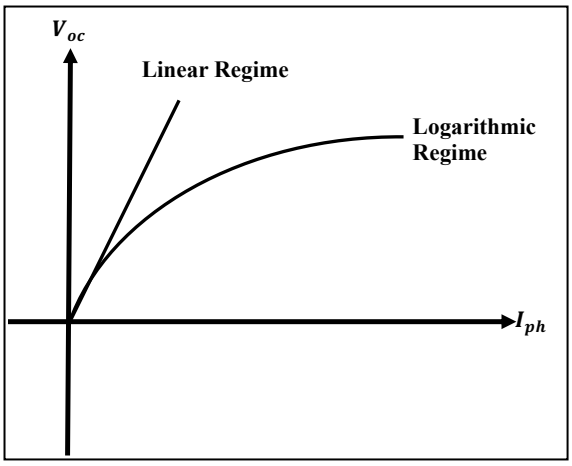

Figure 2. 7. The variation of V_{oc} according to I_{ph} under high and low luminous flux

2.2.3.3. The short circuit current (I_{sc})

The short circuit current I_{sc} is the current that flows through the junction under illumination with no applied voltage. Determination of the exact value of the current I_{sc} depends on the model chosen for solar cell. For an ideal cell, the short-circuit current is equal to the current I_{ph}. I_{sc} increases with the intensity of light illumination, the wavelength of the incident photons, the mobility of charge carriers and temperature.

2.2.3.4. Fill Factor (FF)

The maximum current and voltage supplied to the external circuit by a PV cell under illumination are the short-circuit current (I_{sc}) and open-circuit voltage (V_{oc}), respectively. Nevertheless, the power from solar cell is 0 at both of these operational points. This maximum power (denoted P_m) is determined from an operating point P_m (I_m, V_m) of the I-V curve (Figure 2.7).

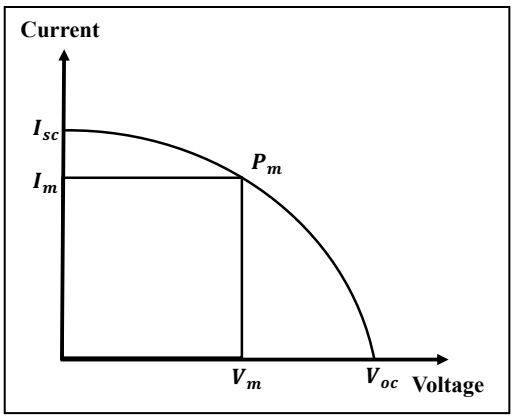

Figure 2. 8. I-V characteristics of solar cell and the position of V_m, I_m and P_M

This point P_M is obtained when the area of the rectangle ($I_m \times V_m$) defined by the axes I_m and V_m passes through a maximum. The "Fill Factor" (FF) is defined by the following relation:

$$FF = \frac{P_m}{I_{sc} \times V_{oc}} = \frac{I_m \times V_m}{I_{sc} \times V_{oc}} \quad \textbf{Eq 2. 4}$$

It represents the ratio of the area of the rectangle P_m defined in Figure 2.7, to that of the rectangle $I_{sc} \times V_{oc}$. The conversion will be more effective the higher FF is. When the surfaces of the two rectangles ($I_{sc} \times V_{oc}$ and $I_m \times V_m$) are closer together, the value of FF rises, and the solar cell exhibits perfect behavior. The deviation from the ideal case comes from the contact resistances, the low mobility of the charge carriers within the semiconductor, or even the leakage currents in the cell.

2.2.3.5. The conversion efficiency (η)

The efficiency η, of PV cells designates the power conversion efficiency. It is defined as the ratio of the maximum power delivered by the cell to the incident light power (P_{in}):

$$\eta = \frac{P_m}{P_{in}} = \frac{I_{sc} \times V_{oc} \times FF}{P_{in}} \quad \textbf{Eq 2. 5}$$

This efficiency can be improved by increasing the fill factor, the short-circuit current and the open-circuit voltage. The conversion efficiency is an essential parameter that makes it possible to evaluate the performances of the cell.

2.3. Different Generations of Solar Cells

2.3.1. 1st generation

1st generation PV cells consist of a single PN homojunction. The typically used semiconductor material is silicon in its monocrystalline form (composed of a single crystal) or polycrystalline (composed of several crystals, of different sizes and orientations). The solar cell is composed of thin wafers of silicon with a thickness ranging from 150 to 300 µm. Although the absorption coefficient of silicon (α) is lower than ~ 100 cm^{-1}, due to its indirect gap, the PV solar cells based on this material remain the most widely used until now. The interest of these cells is mainly linked to the availability of silicon and the maturity of this technology on one hand. On the other hand, their long-term stability, the high mobility of charge carriers and the strong spectral absorption guarantees the high performance and avowed reliability. Nevertheless, they have certain disadvantages such as their cost, their high weight and their rigid character.

Solar cells based on monocrystalline silicon have recorded efficiencies above 25%. Their efficiency is superior to PV cells at based on polycrystalline silicon which provide conversion efficiencies of the order of 22% (Green ve ark., 2021). However, the peak watt price of 1st generation PV solar cells still remains high. This sector requires very advanced and costly technologies with energy-intensive manufacture besides their high weight and their rigid character. Therefore, in order to lower the manufacturing cost, a second generation of PV solar cells have emerged.

2.3.2. 2nd generation

Thanks to the improvement of technologies associated with thin-film deposition (development of characterization techniques, mastery of high vacuum), thin-film based solar cells have been able to find their place in the industry. This generation of PV solar cells, also called second generation, derives its main advantages from its ability to consume less raw materials and its feasibility for large-area growth. Intended for low-cost development, this technology can be obtained by a multitude of growth techniques generally divided into three main classes: techniques requiring a high vacuum (molecular beam epitaxy, co-evaporation, etc.), techniques which require a lower vacuum and they can in some cases be assisted by plasma (Plasma Enhanced Chemical Vapor Deposition (PECVD)(Sharma ve ark., 2014), metal-organic chemical vapor deposition (MOCVD)(Fang ve ark., 2019), sputtering, etc.) and finally techniques that work under pressure and temperature conditions close to ambient (spin coating, spray pyrolysis, screen printing, etc.). The principle of thin-film PV conversion remains practically the same as that of a crystalline silicon cell, but with the general use of PN heterojunctions. For proper operation of thin-film PV cell, the absorber material must have a very high optical absorption coefficient in the visible region of spectrum. As a result, the use of direct gap materials is favored and makes it possible to achieve much thinner thicknesses of the order of 1 to 10 μm compared to crystalline silicon. For terrestrial applications, the most industrialized absorber materials for this generation are mainly amorphous silicon (a-Si) (He ve ark., 2022), cadmium telluride (CdTe) (Swartz ve ark., 2022) and $CuIn_xGa_{1-x}Se_2$ (CIGS) (Wang ve ark., 2022).

A thin film based solar cell consists of a stack of material films deposited on top of each other on a solid of flexible substrates. The nature of the material used for each layer as well as the existing interfaces between them have a direct impact on the overall behavior of the cell and therefore on its performance. Figure 2.8 presents a classic diagram of a

CIGS-based PV cell, illustrating superstrate configuration, generally used in the case of a 2nd generation cell.

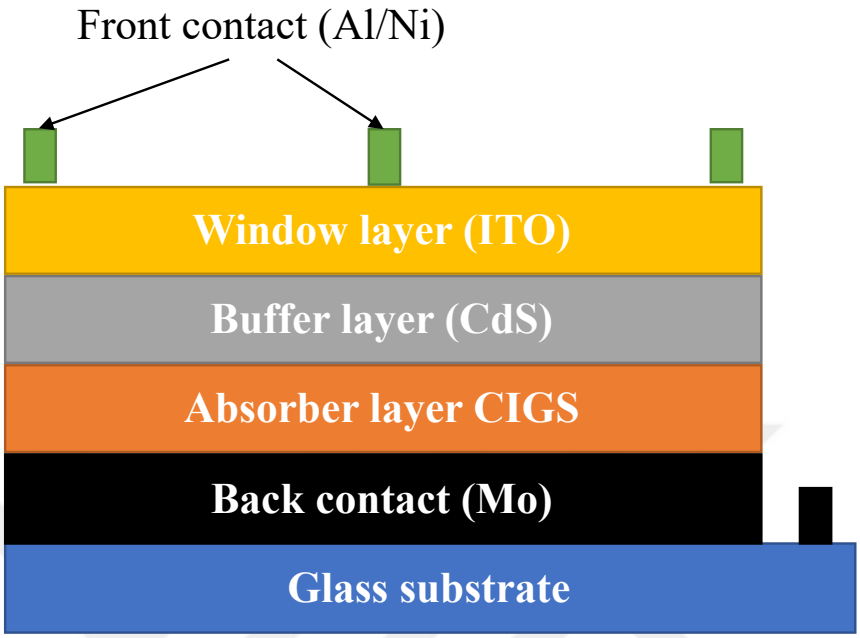

Figure 2. 9. Based configuration of CIGS solar cells

From this example of cell configuration, we can describe the main parts comprising the thin film technology:

- *The Substrate:* it is used to ensure the mechanical strength of PV cell in thin layers. The latter can be rigid such as glass or flexible in nature.
- *Front and rear face contacts:* These are metal contacts used to collect the photo-generated current. These contacts are expected to have an ohmic nature. The most used one in CIGS solar cells is molybdenum (Mo) as a back contact.
- *The absorbent layer:* it is made of a p-type semiconductor material with a high absorption coefficient and a direct band gap in the Vis range. A small thickness of this material is sufficient for the proper functioning of PV cell.
- *The buffer layer:* it is made of an N type SC material. This layer, associated with the absorbent layer, constitutes the active part of PV cell to form the PN junction. The buffer layer also improves the alignment of the band gaps between the absorbent layer and the optical window. Indeed, a good alignment makes it possible to limit the number of recombinations of charge carriers at the interface of the junction. Moreover, it is desirable for buffer layer to have an intermediate

optical gap between that of absorbing layer and that of window layer with a big transmittance property.

- *The window layer:* This layer is used to simultaneously ensure the passage of solar radiation as well as the conduction of charge carriers towards the external circuit of the cell. Indeed, over most of solar spectrum, its optical transmission is supposed to be greater than 80%, with a conductivity greater than 10^4 (Ω cm^{-1}). Such properties are obtained from transparent conductive oxides (TOC) such as SnO_2: F, In_2O_3: Sn, and ZnO: Al.

2.3.3. 3rd generation

The third generation brings together all the new approaches proposed and developed over the past few years. Its advantage lies mainly in its ability to produce devices on flexible substrates and in its ability to operate at low illuminations. This sector generally uses inexpensive materials based on non-toxic elements, as in the case of certain 2nd generation technologies.

- *Organic cells:* the emergence of this technology is associated with its discovery in the early 2000's of semiconducting properties of some polymers. In these solar cells, the active layer is made with a mixture of highly conjugated electron donor and acceptor organic molecules. Thus, by analogy to inorganic materials, the polymers used can be considered as semiconductors. Under the effect of energetically sufficient photon, an electron can acquire the ability to be transferred from VB to CB (Zheng ve ark., 2022).
- *Perovskite-based cells:* The interesting yields obtained by perovskites in recent years, in a record time interval, have made this technology one of the most attractive research trends in the field of PV conversion (Yang ve ark., 2022).
- *Dye solar cells:* dye solar cells and mixed bulk heterojunction/dye cell systems are based on a hole-carrying polymer used as an electron donor. It also seeks to overcome current efficiency limits by resorting to original concepts such as multijunction cells, intermediate gap cells or the use of hot carriers(Agrawal ve ark., 2022).

The majority of third-generation systems are currently under development and aim for more or less long-term industrial applications. Currently, the main driving force in solar

PV energy is silicon solar cell technology. On the other hand, thin film technology is gaining ground as it offers high efficiency and low-cost solar cells.

2.4. Chalcogenides Semiconductors

2.4.1. CIGS

$Cu_2(In_xGa_{x-1}Se_4$ is a semiconductor with a crystal structure of type chalcopyrite (Figure 2.9). Its tetragonal structure is composed of a stack of two zinc blende structures whose tetrahedral sites are occupied by selenium atoms (Xue ve ark., 2014).

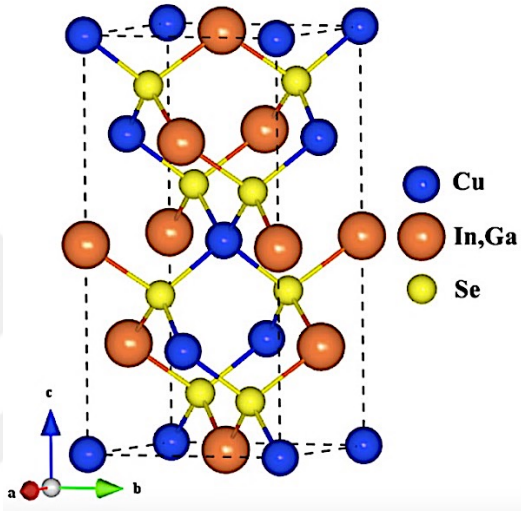

Figure 2. 10. CIGSe crystal lattice (Xue ve ark., 2014)

As shown in Figure 2.9, it is possible to substitute indium (In) atoms with atoms of the same valence structure such as gallium (Ga). It is also possible to carry out the isovalent substitution of selenium by sulfur. These substitutions makes it possible to vary the width of the band gap as well as the lattice parameters of CIGSe.

The preferred crystalline planes parallel to the surface for CIGSe material are generally (112) and (204/220) planes, and more rarely (116/312) (400/008), (332/316) and (424/228) planes (Lee ve ark., 2010). CIGSe deposited in thin layers is a polycrystalline material, so it has grain boundaries. At these interfaces, CIGSe exhibits structural defects, mainly selenium V_{Se}^{++} vacancies. These defects, also present in the volume where can become a source of charge recombination. Therefore, CIGSe deposition are made in an atmosphere saturated with selenium (Lany ve Zunger, 2005; Cho ve ark., 2013).

The substitution of In with Ga can varies the band gap energy and it can be written as (Alonso ve ark., 2002):

$$E_g CIGSe(x) = E_g CIS + 0.626x - bx(1-x) \quad \textbf{Eq 2. 6}$$

with b is an optical constant which varies between 0.11 and 0.26 and x is the amount of gallium substituted for indium in the structure:

$$x = \frac{[Ga]}{[Ga]+[In]} \quad \textbf{Eq 2. 7}$$

Since CIGSe has a direct gap and a high optical absorption coefficient (α >10^5 cm^{-1}), it is capable of absorbing a large part of solar spectrum over a thickness of a few micrometers (Khoshsirat ve ark., 2015).

2.4.2. CZTS

Cu_2ZnSnS_4 (CZTS) quaternary composites belongs to I_2-II-IV-VI_4 semiconductors. Experimentally, Cu_2ZnSnS_4 usually crystallizes in kesterite structure, or stannite structure (Vanalakar ve ark., 2015b) as shown in Figure 2.10. It is often represented as a structure deriving from the chalcopyrite structure in which In^{3+} ions have been replaced by Zn^{2+} and Sn^{4+} ions. Stannite structure differs from kesterite only by the arranging of Cu^{+} and Zn^{+2} (Regulacio ve ark., 2012).

More recently, an interested new phase for the development of solar cells has been highlighted: Wurtzite structure (Yang ve ark., 2014) crystallizes in a hexagonal lattice. A last possible crystalline structure is the cubic phase of Zinc-blende type. The Cu^{+}, Zn^{2+} and Sn^{4+} metal ions present in the Wurtzite and Zinc-blende phases are randomly positioned. Regarding the optical properties, Cu_2ZnSnS_4 in its kesterite phase has a gap of 1.5 eV and an absorption coefficient greater than 10^4 cm^{-1} (Khattak ve ark., 2018). This makes it a promising material for PV applications since zinc and tin are abundant and cheap elements compared to In and Ga.

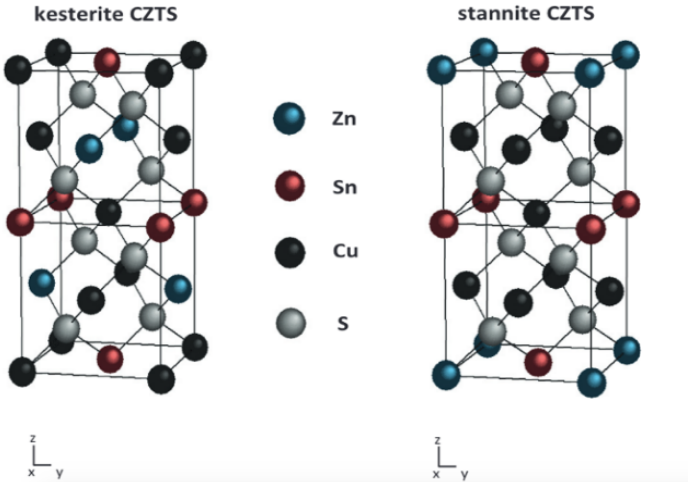

Figure 2. 11. Kesterite and stannite structure of CZTS (Vanalakar ve ark., 2015b)

The main electrical characteristics of semiconductor materials result from the displacements of charge carriers under the effect of an electric or magnetic field (electrical conductivity, Hall effect, photoconductivity, etc.). Nevertheless, these displacements are governed by the collisions of charge carriers with ions, impurities or defects of the crystal lattice. The mean free path, which characterizes the average distance traveled by an electron between two successive shocks, is an important parameter specific to the structural state of materials. In conventional PV materials, in particular silicon, the n and p doping of these semiconductors is often done voluntarily to form PN junction. On the other hand, CZTS semiconductor is naturally p-doped. Its residual doping is intrinsic and inherent due to the crystalline defects of the material. These defects are mostly cation substitutions where copper atoms take the place of zinc atoms (Cu_{Zn}) (Chen ve ark., 2010).

This material meets the same particularities as chalcopyrites, differences in composition lead to large variations in electrical properties. Unsuitable stoichiometries cause secondary phase segregations. More specifically, an excess of zinc and tin as well as a low copper content prove to be favorable for improving electrical performance (Kobayashi ve ark., 2005; Katagiri ve ark., 2008). On the contrary, a zinc poverty is favorable to a segregation of conductive phases such as Cu_xS (Suryawanshi ve ark., 2013). It is also possible to form insulating phases such as ZnS or SnS_2 from regions poor in copper and rich in zinc or tin. These phases are less detrimental to the proper functioning of the cell because they only reduce the active surface of the cell by isolating certain areas and therefore do not cause any short circuit (Schurr ve ark., 2009). A relatively low sulfur content in the thin film would result in better electrical performance (Kumar ve ark., 2015). However, sulfur mostly has a positive effect when used as a precursor (Suryawanshi ve ark., 2013).

Most reported resistivity values of CZTS thin films range from ~10^{-3} to 10^{1} cm.Ω but there are also resistivity values higher than 10^{4} cm.Ω have been reported as well. The concentration of charge carriers has been reported to vary between $10^{16}cm^{-3}$ to $10^{21}cm^{-3}$. Hall effect measurement results proved that the mobility in CZTS layers changed simply from 0.1 to 30 $cm^2.V^{-1}.s^{-1}$, while the most published values were in the range of 1 to 10 $cm^2.V^{-1}.s^{-1}$ (Zhang ve Shao, 2009; Su ve ark., 2012; Rajesh ve ark., 2013; Tang ve ark., 2013).

2.5. Cu_2SnS_3 (CTS)

2.5.1. Different properties

In Cu-Sn-S system, many ternary phases can be formed according to the oxidation state of copper atom; CTS has a Cu^{+1}. Fiecher *et al* ,(Fiechter ve ark., 2003) have cited 18 different phases of Cu-SnS alloys (see Figure 2.11). The major uses for compounds in the Cu-Sn-S system have been suggested as solar absorbers (Reddy ve ark., 2019) and thermoelectric (Sheng ve ark., 2021) materials. The majority of these ternary materials are likely to exhibit a p-type conductivity, an important minority carrier mobility and a band gap of about 1 eV. These features allow them to be considered as a suitable compounds for solar applications (Zawadzki ve ark., 2013).

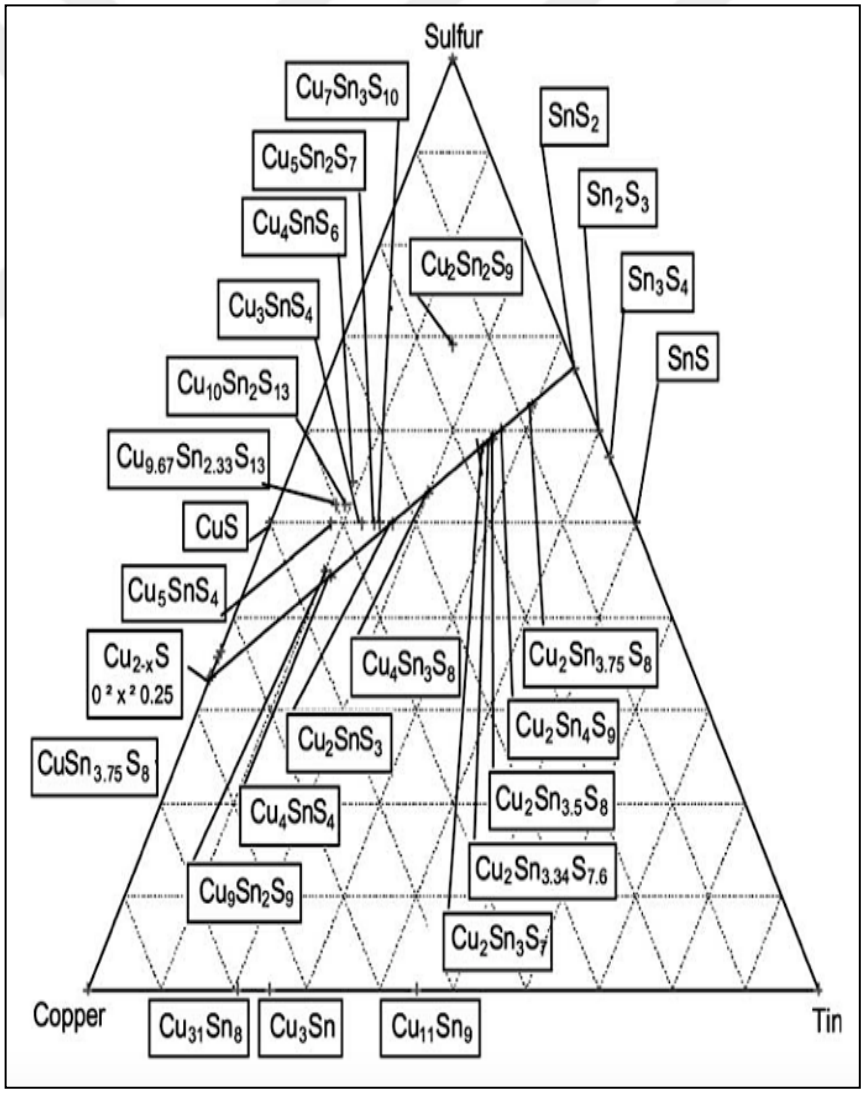

Figure 2. 12. Gibbs phase triangle for the system Cu –Sn –S (Fiechter ve ark., 2003)

As prospective solar absorbers, Cu_2SnS_3, Cu_3SnS_4, Cu_4SnS_4, and $Cu_2Sn_3S_7$ (Kuku ve Fakolujo, 1987; Avellaneda ve ark., 2010; Fernandes ve ark., 2010; Umehara ve ark., 2013; Zawadzki ve ark., 2013; Gezgin ve ark., 2022; Jo ve ark., 2022) have been examined. The majority of these materials were proven to exhibit direct band gaps ranging from 0.8 to 2 eV, as well as strong absorption coefficients ($>10^4$ cm^{-1}).

2.5.1.1. Structural properties

This ternary material (Cu_2SnS_3) can be found in many structures; monoclinic, cubic, tetragonal, hexagonal, and triclinic (Figure 2.12). The formation of these structures depends on cation's (Cu/Sn) disorder, post deposition and annealing temperature.

CTS material is a ternary semiconductor compound belonging to the group: I-IV-VI. It is a polycrystalline material that crystallizes in different systems, namely: monoclinic (Berg ve ark., 2012), triclinic (Han ve ark., 2014), cubic (Bouaziz ve ark., 2011), tetragonal (Fernandes ve ark., 2010) and hexagonal (Wu ve ark., 2007) . Experimentally, cubic, monoclinic and tetragonal structures are the most frequently observed on many works and essentially obtained from physical and chemical methods (Lokhande ve ark., 2016a; Lokhande ve ark., 2016b).

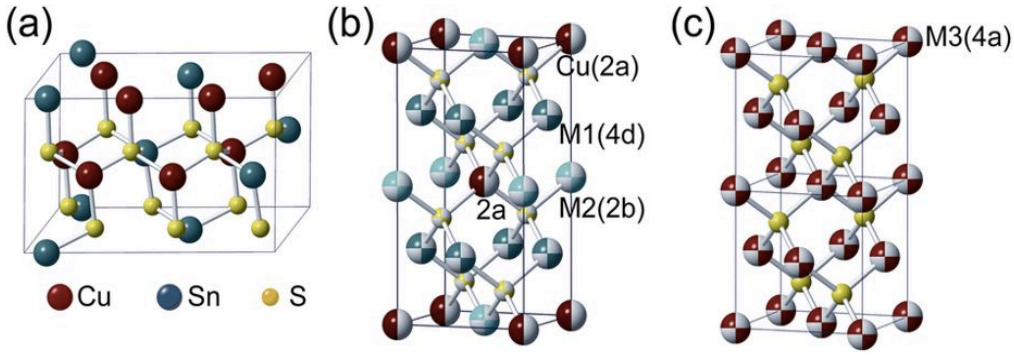

Figure 2. 13. Crystal Structures of CTS; a) Monoclinic b) Tetragonal c) Cubic. Atomic concentration: M1(Cu:56.4%/Sn: 43.6%), M2(Cu: 53.7%/Sn: 46.3%), M3(Cu: 66.7%/Sn: 33.3%) (Shen ve ark., 2016)

Usually, the structural characterization of a compound is carried out by X-Ray Diffraction (XRD). Nonetheless, the identification of this compound is difficult because of the close locations (2θ) of the diffraction peaks that characterises CTS different structures. The fact that Cu_3SnS_4 secondary phase has a cubic structure similar to that of Cu_2SnS_3, their lattice parameters are close enough and makes their detection by XRD very difficult

(Baranowski, 2015). For these reasons, most published studies combine XRD characterization results with Raman spectroscopic analysis (Lokhande ve ark., 2016a). The different crystal structures of CTS are much more apparent in Raman spectra, because the peaks do not overlap, as is the case with XRD.

2.5.1.2. Optical Properties

In this section, we present some of CTS optical features, which can have a big effect on the performance of CTS-based solar cells. Regarding CTS compound, all the theoretically calculated Density Of States (DOS) showed that the valance band maximum and the conduction band minimum are at the symmetry point Γ as shown in Figure 2.13 (Zhai ve ark., 2011). As a result, CTS has a direct optical gap whose theoretical values vary from 0.84 eV to 0.88 eV (Zhai ve ark., 2011), while experimentally the different optical gap values reported in the literature are much wider range, ranging from 0.83 to 1.77 eV (Avellaneda ve ark., 2010; Chen ve ark., 2012; Zhao ve Cheng, 2013; Reddy ve ark., 2015).

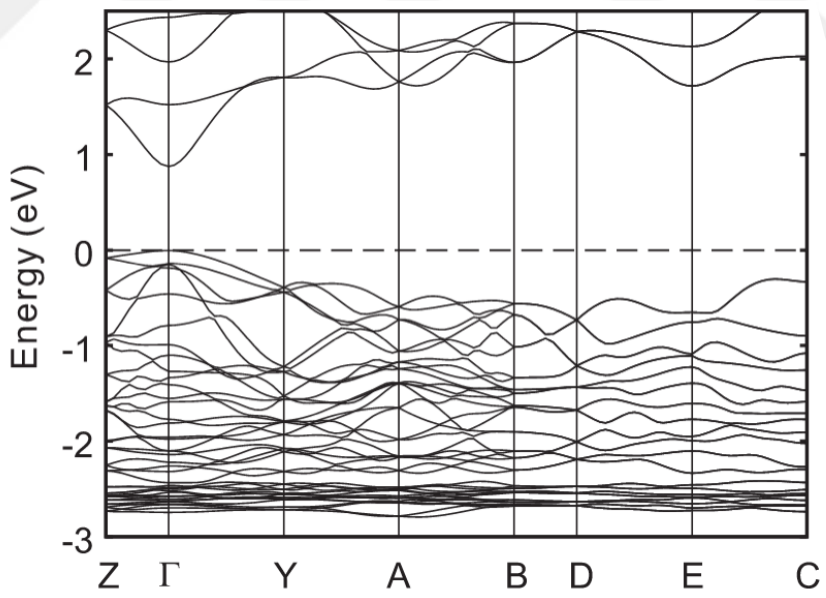

Figure 2. 14. Density of States of CTS material (Zhai ve ark., 2011)

This compound is also characterized by a high optical absorption coefficient which can reach a value of 10^5 cm^{-1} (Bouaziz ve ark., 2009; Reddy ve Reddy, 2017). Thus, a small thickness of CTS would be sufficient to absorb the maximum solar radiation in Vis range.

The presence of secondary phases such as Cu_xS and SnS significantly affect the optical properties of CTS compound. These phases appear as defects in the crystal structure and directly affect the optical properties of the material (Zhao ve Cheng, 2013; Dong ve ark., 2015; Miyata ve ark., 2015; Lokhande ve ark., 2016a).

2.5.1.3. Electric Properties

CTS material is often reported as p-type, with carrier concentrations ranging from 10^{14} cm^{-3} to 10^{22} cm^{-3} and a minimum resistivity of 10^{-4} (Ω·cm) (Pallavolu ve ark., 2018; Yang ve ark., 2020). Moreover, the electrical properties of CTS are also influenced by the formation of secondary phases. Indeed, the presence of copper-rich phases such as Cu_3SnS_4, Cu_4SnS_4 and Cu_xS implies an increase in the conductivity of CTS material. Robles et al. (Robles ve ark., 2015) reported an increase in the resistivity of CTS from 2.10^{-3} Ω.cm to 5.10^{-3} Ω.cm after chemical treatment with KCN which indicated the elimination of the conductive Cu_xS phase on the surface of a CTS thin film. Bodeux *et al.*(Bodeux ve ark., 2015) reported the effect of composition variation on the increase in CTS (Kim ve ark., 2018) conductivity. They observed an increase from 0.1 $S.cm^{-1}$ to 0.8 $S.cm^{-1}$ for a Cu/Sn ratio increasing from 1.9 to 2.2. Thus, it is clear that the presence of secondary phases modifies the optical and electrical properties of CTS compound and consequently affects the conversion efficiency of PV solar cells.

2.5.1.4. Structural Defects

Unlike intentionally doped silicon, CTS is a naturally p-type semiconductor. This type of conductivity is attributed to the presence of intrinsic defects in CTS compound. Using the first principal calculation, it was found by many groups that the dominated defect in CTS is the copper acceptor vacancy (V_{Cu}) with a formation energy of -0.66 eV. V_{Cu} is a shallow level situated just above the valance band maximum (0.04 eV). These defects are believed to be the main acceptor state of CTS, likely responsible for its p-type conductivity. As for the main donor defect, Sn on Cu antisites Sn_{Cu} with a transition level of 0.2 eV, it can serve as a recombination centre. The formation energy of S vacancy V_S is low, but it doesn't affect the carriers due to the absence of its transition level in the band gap (Baranowski ve ark., 2014; Baranowski ve ark., 2016; Nishihara ve ark., 2017). On the other hand, defects of V_{Sn} and Cu_{Sn} type seem thermodynamically unfavorable and have a low probability of presence (Baranowski, 2015; Tiwari ve ark., 2017).

2.5.2. CTS thin films preparation techniques

Multiple deposition techniques were used to synthesize CTS thin films. The physical deposition methods such as evaporation (Kanai ve ark., 2015; Nakashima ve ark., 2015a; Nakashima ve ark., 2015b; Sasagawa ve ark., 2018) or sputtering(Dong ve ark., 2016; Lee ve ark., 2017; Xu ve ark., 2018) are mainly based on a stuck metal deposition of Cu and Sn and then they require an additional sulfurization step. In other works, the used precursors were sulfides or oxides of Copper (Cu) and Tin (Sn) metals (CuS, SnS, Cu_2S and SnS_2) (Bodeux ve ark., 2015; Wang ve ark., 2017; Shin ve ark., 2020).

Sputtering, thermal evaporation and electron beam evaporation remain today the most efficient and widely used techniques for CTS thin film deposition (Umehara ve ark., 2013; Aihara ve ark., 2014; Lokhande ve ark., 2016a; Kanai ve Sugiyama, 2021). In this chapter, a general presentation on these three physical deposition techniques have been discussed. Since a common and universal method to produce thin layers does not exist, we must choose the one that is adapted to our expectations and our objectives. Due to that, we focused on the production of CTS based PV cells which requires a deposition method that is adaptive to our laboratory and adjust to the goals and objectives of our work. PLD technique is versatile and widely used technique that is recognized by producing good quality thin films with exact stochiometric transfer from the target to the deposited thin films. This technique is extremely beneficial since we deal with a very low concentration of doping in our work. This method is the subject of our study for the deposition of PV thin layers of CTS.

2.5.2.1. Sputtering

Cathodic sputtering is a physical deposition technique widely used by researchers and industrialists to deposit a multitude of materials in thin layers form with a good quality. This technique consists of bombarding a target (source material to be deposited) fixed in a cathode with accelerated ions coming from a plasma (generally ionized argon), with enough energy to tear off its atoms. The extracted atoms travel through the enclose chamber held under high vacuum. Afterwards, they condense on a preheated (if required) substrate fixed to an anode (usually) in front of the target. The cathode-anode assembly can be put either under an alternating voltage, which is called RF sputtering or a direct voltage, in this case it is called DC sputtering. The chosen type of the applied voltage is relative to the nature of the target material to be deposited (conductor, semi-conductor or

insulator). In the case where the target is composed of several sources of elements, it is called co-sputtering. The team of Kanai *et al.* (Kanai ve Sugiyama, 2021) was able to make a CTS-based PV cell by depositing the absorber material by RF sputtering. In this study, sulfurization process was carried out at an annealing temperature of 560°C. The PV cell fabricated under these conditions had a conversion efficiency of 5.2%.

2.5.2.2. Thermal evaporation

Thermal evaporation is the most often utilized thin layer deposition method as it is easy to apply. Its principle is based on the evaporation of a source material placed in a pot and evaporated at an appropriate temperature to subsequently condense on a substrate. The choice of temperature depends on the elements or the source components to be deposited. Generally, the substrate is fixed on a rotary system to ensure the homogeneity of deposition. Similar to the sputtering, the thin layers are produced under high vacuum conditions, using a single source or several sources (co-evaporation). In PV applications, because depositing compound materials (CTS, CZTS, CIGS...) with the same composition as the source is problematic, this technique is often supplemented with a sulfurization phase to increase the quality of the deposited thin films (Kanai ve ark., 2015; Nakashima ve ark., 2015a; Nakashima ve ark., 2015b; Sasagawa ve ark., 2018).

2.5.2.3. Pulsed laser deposition

In theory, the technique is fairly simple to put into practice. A high-energy laser is used to ablate the target material that is maintained in a vacuum or under partial pressure of a reactive or neutral gas. Throughout this irradiation, the mechanism of laser-matter interaction will induce atoms vaporization, which will be liberated from the target and ionized to create a plasma under the influence of the laser's energy. It is feasible to collect the species discharged by the target to form a thin layer thanks to the proper arrangement of the substrate.

Pulsed laser deposition (PLD) [74] is recognized as a highly strong technology for producing thin films of excellent quality employing various deposition parameters (such as; wavelength, energy per pulse, substrate-target distance, etc). In 2015, Ettlinger *et al.*(Ettlinger ve ark., 2015) used PLD technique to provide the first CTS thin films. After that at the same year, Vanalakar *et al.*(Vanalakar ve ark., 2015a) was able to reach a conversion efficiency of 0.82% using PLD to synthesize CTS thin films for the first time. Afterwards, a lot of research on the same trend have been published (Ettlinger ve ark.,

2016; Raadik ve ark., 2017; Wang ve ark., 2017; Schou ve ark., 2018; Thota ve ark., 2019). For most of PLD experiments, the deposition was held using one single target of C-Sn-S.

2.5.2.4. Ball milling

Processing materials is an everyday treatment to obtain the required microstructure and properties. This process is assured by entering the material into nonequilibrium/exited-state by energizing it with high-energy. Conventionally, researchers have used light, pressure, temperature, or electricity to excite the equilibrium material. However, using mechanical stress (brute force) to energize a material is a simple and unconventional way. Ball milling (BM) grinding technique is an alloying technique based on solid state reaction. The reactant powders in this method are cold welded, fractured and then rewelded due to the high energy released throughout the ball milling process (Suryanarayana, 2008). This technique appeared for the first time in 1966 by Benjamin *et al.* (Benjamin, 1970) for the production of superalloy based on nickel for application in the gas turbine. After that, the scientific community interested in this new solid-state reaction method specially since is raw products are commercially available (Suryanarayana, 2001; Kilmametov ve ark., 2019; Vaidya ve ark., 2019).

BM is an uncomplicated and a practical technique that is available in laboratory and on an industrial level with many advantages. One of the most important advantages of this technique is the production of new alloys that are very difficult to construct using other methods because of its immiscible nature. This is due to the fact that BM is a purely solid-state processing approach, hence phase diagram constraints do not apply (Suryanarayana ve ark., 2001).

The milling process in abridged, is filling a cylindric container with the milling medium and the required raw powder materials. This process is extended for a certain duration of time with a specific speed and at a controlled atmosphere to a sure the best milling results. The milling medium (balls) must be harder than the raw materials in order to prevent grinding the balls. There are many different factors that affect the BM process and have a very important effect on the final product. Namely, ball to powder ratio (BPR), milling time, starting (raw) materials and milling speed. Altering these parameters will grantee the production of different sizes and different alloys. The standard BM process is dry

milling but wet milling is also possible using different types of solution that are nonreactive with the raw materials during the BM process. The wet milling is often used to achieve small sized powders with less agglomerations (Okada ve ark., 1992).

(a) (b) (c)

Figure 2. 15. (a) Laboratory Vibratory/shaker mills, (b) Laboratory planetary ball mill and (c) Laboratory attritor mill

For the manufacturing of mechanically alloyed powders, many types of high-energy equipment are already in use, depending on their capacity, milling efficiency, and commercial reasons. Vibratory/shaker mills, planetary ball mills and attritor mills are the most important milling machines among them (see Figure 2.15).

CTS material was produces by ball milling for different application using different combination of raw materials, the most common is the use of elemental powders of copper, tin and sulfur with high purity (Chen ve ark., 2012; Vanalakar ve ark., 2015c; Basak ve ark., 2018; Nakata ve ark., 2019; Lohani ve ark., 2020b). The use of combined sulfides (example: CuS and SnS) is very limited in very few studies (Wubet ve Kuo, 2015; Hegedüs ve ark., 2018; Lohani ve ark., 2020a).

2.5.3. CTS solar cells history and achievements

Usage of CTS as an absorber layer was first reported in 1987 by Kuku *et al* (Kuku ve Fakolujo, 1987), where a Schottky type solar cell was produced with an efficiency reaching a 0.11%. After that, no other solar device was stated until 2012. Due the enormous interest gained by CIGS and then CZTS at the first decade of the 21 century, the attention was shifted to CTS as one of CZTS's stable phases. The second reported solar cell was produced in 2012 by Koike *et al*, with efficiency of 2.82% (Koike ve ark., 2012). Then, many groups focused on this material. In 2013, Umehara *et al*. were able to increase the conversion efficiency up to 6% by using the next ratios of elements Cu_2Sn_1.

$_XGe_XS_3$ with X=0.17 (Umehara ve ark., 2013). The conversion efficiency world record of CTS based solar cells have reached 5.2% using Na doped films (Kanai ve Sugiyama, 2021). The same group also used K atom as a dopant for CTS and improved the conversion efficiency of the solar cells (Nakashima ve ark., 2017). Other articles have also verified the positive effect of Na doped CTS material to enhance the PV properties (Nakashima ve ark., 2015a; Chantana ve ark., 2017a; Chantana ve ark., 2017b; Sasagawa ve ark., 2018). On the other hand many other dopant atoms (Sb (Magdy ve ark., 2021), Ag (Zhao ve ark., 2020), K (Nakashima ve ark., 2017)) were used to enhance the general properties of CTS and increase its efficiency.

2.6. Alkaline Atoms Doping Effects

The revolutionary thin films solar cells (CIGS, CZTS) with their complex structure and many defects have opened new windows to further enhance their efficiencies by optimising the deposition parameters or playing with the stoichiometry of different elements.

One of the most effective ways is by doping these quaternary materials with Alkali atoms (mostly Na & K). Impacts on different material are proven to be positive but it varies from one material to another due to different intrinsic properties of each one. Next, the effect of the Alkali atoms on the CIGS, CZTS/CZTSe, CIS will be explained.

2.6.1. CIGS

As a promising quaternary semiconductor CIGS has made a revolution in efficiently enhancement of the solar cells by reaching up to 22.9% (Kato ve ark., 2019), where the main factor was the use of alkali atoms for doping this material. Na was the most used atom for doping as its incorporation was proven to enhance the open circuit voltage V_{oc} by improving the P-type properties of CIGS by passivating the grain boundary defects and, in some cases, even increasing the grain size (Salomé ve ark., 2013; Salome ve ark., 2014; Rehan ve ark., 2018). Consequently, a better efficiency was found on these CIGS based solar cells.

The researches were kept on going by using potassium (K) atom instead of Na, due to its close atomic configuration, similar but not always better results were found. K doped CIGS has presented a better crystallography and in general an enhancement in carrier concentration along with V_{oc}, FF and the efficiency η (Jackson ve ark., 2014; Laemmle ve ark., 2015).

The p-type conductivity of CIGS is mostly due to the intrinsic donor defect V_{cu}^{-} (low formation energy 0.06eV) that adds a transition defect level of 0.03 eV above the valance Band (Zhang ve ark., 1998). Other donor defects also are present in CIGS, In_{Cu}^{++} and V_{Se}^{++} that reduces the carrier concentration and the performance of CIGS solar cells devices (Lany ve Zunger, 2005; Cho ve ark., 2013).

The increase in the carrier's concentration in CIGS due to the doping of Na and K atoms has not yet well understood. There are many theories trying to explain the obtained high effective acceptors concentration, and we can divide it into two categories: passivation of defects and position of Na atoms.

2.6.1.1. According to passivation of the defects

Na atoms enter into a chemical reaction with the intrinsic defect of CIGS:

- The V_{Se} found on the surface of CIGS's grains is passivated by the introduction of Na (Kronik ve ark., 1998; Wei ve ark., 1999).
- Eliminating the In_{Cu} antisite donor defects was set as the main reason for the increase in hole carrier's concentration(Wei ve ark., 1999).
- Na forms an antisite on V_{Cu} but it doesn't contribute to the electric conduction (Wei ve ark., 1999; Azulay ve ark., 2016).

2.6.1.2. According to the position and the segregation of Na atoms

- On the grain boundaries: this model states that Na (K) atoms are located on the grain boundaries of CIGS while they passivate the existing defects (Kronik ve ark., 1998; Niles ve ark., 1999; Azulay ve ark., 2016).
- On the bulk of the grains: this supposition is an assumption that Alkali atoms stay in the grain bulk generating a new acceptor's antisites Na_{In} and Na_{Ga} (Schroeder ve Rockett, 1997; Sun ve ark., 2009). Another supposition illustrate that the enhancement of the hole concentration due to alkali atoms doping by the catalytic role of Na atoms, that induces the formation of the acceptor defects V_{Cu} (Yuan ve ark., 2016).

The experiments didn't stop to the usage of Na and K but also other heavy alkali atoms such as Rb and Cs were used. In this context, researches are relatively new with lack of theoretical vision. However, obtained results are pleasant reaching the word record efficiency of 22.9% (Kato ve ark., 2019) using Cs as a dopant. KATO *et al* (Kato ve ark., 2019) have declined that the best improvement of the carrier's life time was obtained

by using Cs atom comparing to use the light alkali atom K. Consequently, V_{oc} and FF were enhanced. Supporting this papier, other publications also declare the positive effect of CIGS doped Cs solar cells (Jackson ve ark., 2016; Khatri ve ark., 2019). Before this champion cell, Rb doped CIGS based solar cell (Jackson ve ark., 2016) has given the best conversion efficiency of 22,6% for almost 3 years. A better diode quality, an enhancement in the carrier's life time and a decreasing of the recombination rate (passivation the grain boundaries) due to Rb doping were reported (Jackson ve ark., 2016; Kodalle ve ark., 2018; Feurer ve ark., 2019). Through the measurement of the concentration of alkali atom before and after Rb (Cs) treatment, a very interesting behaver was observed; they do attempts to segregate into the grain boundaries replacing the SLG defused lighter alkali atoms (Na & K) (Jackson ve ark., 2016; Kodalle ve ark., 2018; Feurer ve ark., 2019; Khatri ve ark., 2019).

2.6.2. CZTS

Similar to CIGS, as a quaternary semi-conductor CZTS (Cu_2ZnSnS_4) was considered as a very interesting semi-conductor. Because of its composition that only contains Earth-abundant and non-toxic elements, it was deemed as an ideal alternative to CIGS. The research on this p-type semi-conductor was wildly done over the last two decades where its conversion efficiency was increased from 0.66% (Katagiri ve ark., 1997) to the world record performed by IBM Group 12.6% (Wang ve ark., 2014). Almost all alkali atoms were used as dopants for CZTS; Li (Yang ve ark., 2016), Na (Prabhakar ve Jampana, 2011), K (Tong ve ark., 2014), Rb (Altamura ve ark., 2016) and Cs (Mule ve ark., 2017). The positive effect of alkaline atoms was clearly shown in many research by enhancing the solar cells based CZTS performance, by grain size augmentation and improving the crystallinity of the grown films, or by passivating the recombination centres on the interface with the buffer film layer, that effect directly on the CZTS based solar cells by increasing the efficiency and V_{oc} (Xin ve ark., 2015; Altamura ve ark., 2016; Mule ve ark., 2017).

The complex structure of CZTS made it a subject of many intrinsic defects that play a fundamental role in controlling its type; the dominated intrinsic defect is Cu_{Zn}^{-} antisite that have the lowest formation energy following that the V_{Cu}^{-} vacancy. These are the dominating acceptor defects in CZTS structure. Cu_{Zn}^{-} antisite & V_{Cu}^{-} vacancy introduce two shallow acceptor levels; 0.11eV and 10 meV, respectively. As for the donor defects,

their formation energy is relatively low; Zn_{cu}^{+} has the lowest energy sallow donor level (Chen ve ark., 2013).

Xin *et al* (Xin ve ark., 2015) has chosen to use Li as a doping agent to improve the performance of Li doped CZTS solar cells (V_{oc}, I_{sc}, FF, R_s, R_{sh}) and the diode quality factor. It reflects by passivating of the recombination centres along the junction and by increasing the carrier's diffusion length. To explain the effect of Li, some theories were given; (1) Li atoms occupied V_{Cu} reducing by that Zn_{Cu} antisite donor defects and Sn_{Cu} antisite deep acceptor defect increasing by that p-type carrier concentration, (2) Li atom might substitute on Zn site forming a shallow acceptor level Li_{Zn} that might be shallower than Cu_{Zn} antisite. Cabas *et al* (Cabas-Vidani ve ark., 2018) was able to reach a very high efficiency 11.6% competing with the value of champion solar cell which was 12.6% (Wang ve ark., 2014).

Xiao *et al* (Xiao ve ark., 2015) have performed a theoretical study on the intrinsic defects in CZTS along with the extrinsic defects due to Na dopant. The calculation revels extrinsic defects resulted from the introduction of Na:

- Na_{Cu} is an antisite with a very low formation energy. It is an isovalent doping (doesn't affect the conductivity of the crystal).
- Na_{Zn} also is an antisite with a low formation energy. However, it is different from Na_{Cu}. Na_{Zn} forms a shallow acceptor level contributing to the conductivity and enhancing the performance of the solar cells.

Not far from the theoretical work results, many researches were focused on the effect of Na doping on the CZTS based solar cells. Tejas *et al* (Prabhakar ve Jampana, 2011) have found that Na doping enhances the film growth (grain size) and the (112) texture of CZTS thin films . Similar results were found by Wen *et al* (Wen ve ark., 2015) where Na incorporation affects the grain size and the film electric conductivity. A compact structure, which is free of pinholes, was obtained in Na doped CZTS films grown by Singh *et al* (Singh ve ark., 2016). Therefore, Na doped CZTS solar cells explored a better efficiency. Similar results also were reported by Werner *et al* (Werner ve ark., 2015).

K was also used as a dopant in CZTS. Using first principle calculation has proved that K atoms might reduce the formation of harmful Zn_{Cu} antisite and Zn-rich secondary phases (Zhang ve ark., 2017). It was also verified that K atoms can improve the energy conversion efficiency of CZTS thin films (Tong ve ark., 2014; Li ve ark., 2017).

The works based on Rb and Cs are still considered to be new, hence some very interesting results were found. The expected positive effect of these atoms was not always present

in CZTS material, however some articles stated that the use of these two atoms along with Na might enhance the PV properties of these thin film together with the solar cells devices (Altamura ve ark., 2016; Hsieh ve ark., 2016; Mule ve ark., 2017).

2.7. Pulsed laser deposition technique

2.7.1. History of PLD

In 1960's, many advances in the study of laser-matter interaction were made immediately after the invention of laser. It was notably in 1962 that F. Breech and L. Cross studied the phenomena of vaporization and excitation of atoms on a solid surface irradiated by a laser (Breeh ve Cross, 1962). This understanding of the phenomena involved enabled H. M. Smith and A. F. Turner to carry out the first experiments in pulsed laser ablation (Smith ve Turner, 1965) and to establish the bases of this original technique for depositing thin films in early 1965.

At this time, the success of this technique was described as "non-predictive" by these inventors due to the many unknown phenomena linked to the formed plasma by lasers. It was only after 20 years later, following the progress in laser technologies and in vacuum technology, that laser ablation experienced its first real boom. Thus, in 1987, D. Dijkkamp *et al.* work make this technique famous thanks to the synthesis of superconducting oxide thin films with very high quality (Y-Ba-Cu-O) (Dijkkamp ve ark., 1987).

This success allows the pulsed laser ablation technique to become more widespread in laboratories. Nowadays, this deposition technique is very widely used in the scientific world and also in industry because it allows the production of a very wide range of compounds such as oxides, metallic, semi-conductor films and ceramic layers, etc. The nature of the films obtained can be amorphous, crystalline or nanostructured. Add to this wide range of materials and the wide range of experimental conditions, the constant progress of laser technologies and vacuum chambers combined with the moderate cost of this technique compared to more complex growth processes. These are all points that make laser ablation a constantly evolving technology.

In theory, PLD technique is fairly simple to put into practice. A high-energy laser is used to ablate the target material that is maintained in a vacuum or under partial pressure of a reactive or neutral gas. Throughout this irradiation, the mechanism of laser-matter interaction will induce atoms vaporization, which will be liberated from the target and ionized to create a plasma under the influence of the laser's energy. It is feasible to collect

the species discharged by the target to form a thin layer thanks to the proper arrangement of the substrate.

2.7.2. Introduction to laser ablation technique

PLD is a well-established technique in the world for research and industrial applications. Today, PLD is used in many fields of study because it offers many advantages compared to other deposition techniques.

In principle, the technique is very simple to design, produce and run. A high-energy laser irradiates a target material placed under vacuum or under partial pressure of reactive or neutral gas. During this irradiation, the laser-matter interaction mechanisms cause the vaporization of atoms which is released from the surface of target and then ionized to form a plasma. All these processes are taken place within a laser pulse volume at the focal point. Thanks to the appropriate positioning of the substrate, it is possible to collect the species released from the target to form a thin layer.

The principal facilities required for PLD are these following elements:

- A high-power pulsed laser.
- An optical device for transferring and focusing the laser beam on the target.
- A substrate placed in front of the irradiated target.
- A vacuum chamber in which a target (material source) and substrate are placed.
- A pumping unit allowing the chamber to be placed under a high vacuum.

2.7.3. Laser-target interaction during laser ablation

A laser (**L**ight **A**mplification by **S**timulated **E**mission of **R**adiation) beam is a polarized, coherent and generally monochromatic (the most nearly monochromatic obtained up to date). The energy E_{Laser} (in eV) of the photons is defined by the Planck-Einstein relation as a function of the electromagnetic wave frequency ν (in Hz) and the Planck constant h (6.63×10^{-34} J.s) according to the following formula:

$$h\nu = E_{Laser} \qquad \textbf{Eq 2. 8}$$

The wavelength λ_{Laser} (in nm) associated with this laser beam is directly linked to the frequency of the wave and to the celerity of light in vacuum c (3×10^{8} m.s^{-1}) by the following relationship:

$$\nu = \frac{c}{\lambda_{Laser}} \quad \Leftrightarrow \quad \lambda_{Laser} = \frac{1240}{E_{Laser}} \qquad \textbf{Eq 2. 9}$$

The interaction of such a very high energy beam with a solid material will generate a succession of phenomena which will lead to an ablation of the material in a form of a plasma if the energy is high enough. This plasma is mainly made up of atoms or molecules (excited or not) existent in the ablated material. In a second period, the material plasma begins an adiabatic expansion in vacuum. Finally, a last step leads to the deposition on a substrate of the species contained in the plasma. The repetition (number) of laser pulses that allow the ablation, deposition and finally growth of layers of controlled thickness. The steps leading to plasma formation and expansion are depicted in Figure 2.14:

a. First of all, the laser beam is focused on the target materials where a mechanism of absorption occurred. Upon impact, photon energy is converted into thermal energy through the free carriers (electrons) present in the target (conductors or semiconductors). This first step is extremely fast (of the order of a few hundred of ps) compared to the duration of the laser pulse.
b. The increase in the local temperature at the surface of the material is therefore very large and rapid. Extension by thermal conduction is very limited in depth and speed given the speed of the phenomenon in comparison with thermal propagation.

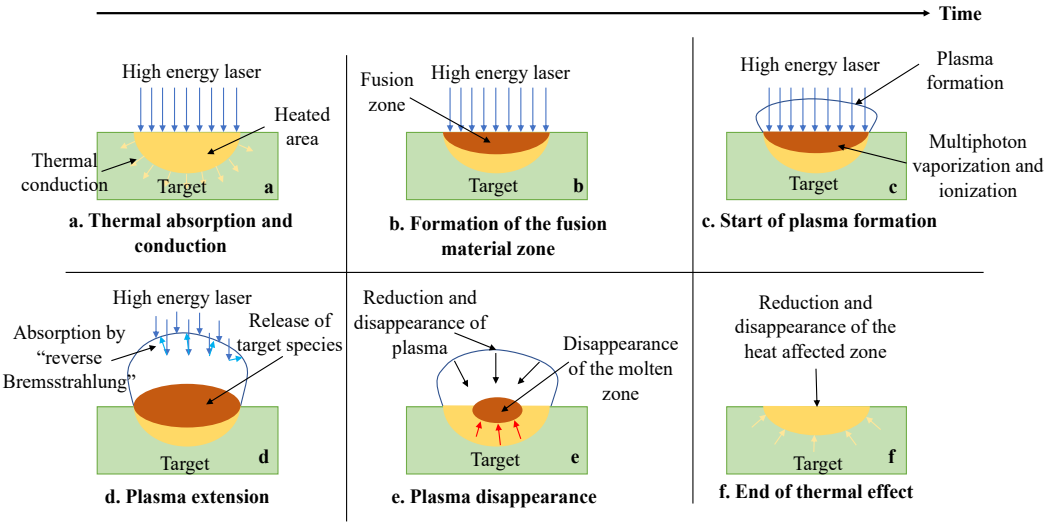

Figure 2. 16. Mechanism of laser matter interaction during laser ablation

c. Under the effect of temperature increase, the species present on the surface of the zone affected by the laser will reach the vaporization threshold and form a dense

layer of excited particles called Knudsen layer. This is the start of plasma formation. Once the beginning of the plasma formed, the latter will gradually extend in a direction perpendicular to the surface of the irradiated target.

d. The photons continuing to irradiate the target will be absorbed in the very dense plasma by the "inverse Bremstrahlung" phenomenon, thus limiting the interaction with the target and accelerating the expansion of the plasma. Therefore, the energy of these photons will be transmitted to the charged particles of the plasma. The phenomenon continues until the plasma becomes totally impermeable to incident photons due to its ionic nature, giving it optical indices n and k) close to 1 and 0, respectively (n tending towards 1 meaning total reflectivity and k tending towards 1 meaning here a total permittivity). Once this threshold is reached, the laser no longer irradiates the plasma or the surface of the material. As long as the laser beam is present, Knudsen layer retains its density but tends to expand. As a result, it slightly loses its density, which makes it more absorbent, thus allowing more laser photons to interact with the surface of the material, leading to a greater release of particles, thus referring to a further increase in the density of the plasma. The phenomenon is therefore maintained, self-regulated and stable as long as the laser irradiates the surface. The duration of plasma generation is therefore almost equivalent to the duration of the laser pulse (Voevodin ve Donley, 1996; Tan ve ark., 2007; Fujioka, 2015).

e. Once the laser pulse has ended, the density of the layer is no longer maintained and a reduction of Knudsen layer and of the plasma is observed. It is following this step that almost all of the ejected species contained in the plasma join the substrate to form the thin layer.

f. After that, the total disappearance of the plasma and of the zone in fusion after is observed.

2.7.4. Non-thermal phenomena in the interaction laser beam -material

Additional processes of the photochemical type can occur during the ablation of semiconductors or insulators. In this case, the absorption of a photon shifts the material from a bonding orbital to an anti-bonding orbital, thereby breaking chemical bonds in the material. This implies that the photons have an energy greater than the binding energy in the solid. Note that at high power densities, such phenomena can result from multiphoton absorptions. When the proportion of broken bonds is sufficient, part of the material is

ejected, without there being any significant heating of the target. The best-known example is the ablation of polymers where laser radiation (UV wavelength) breaks the bonds between the monomers, leading to a non-thermal etching of the material. In the general case of semiconductors or insulators, this phenomenon is often associated with a thermal component

2.7.5. Ejection of condensed particles

During the synthesis of thin films by PLD, the deposition of "particles" of micrometric size (harmful effect) on the substrate is frequently observed. We generally seek to avoid this type of pollution that damages the thin films surface but their origins can be various. Detailed studies of the problem have been carried out previously (Angleraud ve ark., 1999; Orlianges, 2003; Orlianges ve ark., 2004) which highlight two major contributions, the surface state of the target during the interaction and the phase explosion. Both reasons lead to the explosion of matter in the form of condensed particles. If it is easy to understand the role of the surface condition of the target and to remedy it, this is not the case for the phase explosion. Indeed, just after the end of the laser pulse (15 ns), the vaporized material located just above the surface of the target and which has not yet had time to undergo a significant expansion, is at an extremely high pressure (close to the pressure of the solid). This can bring the "liquid" target surface to a temperature close to the critical thermodynamic temperature. When the ejected material begins to expand, the vapor pressure above this surface drops sharply and the liquid phase will suddenly boil explosively, ejecting droplets likely to settle on the substrate. The appearance of this phenomenon depends on the particular thermal characteristics of the target material and is inevitable beyond a certain fluence.

2.7.6. Advantages and disadvantages of PLD

PLD is a technique with many advantages over other processes for growing materials in thin layer or nanostructure forms. Indeed, the method is simple in its implementation but offers many possibilities as to the parameters allowing the control of deposited layers properties. This technology is therefore relatively flexible and less expensive than most other thin layer deposition techniques since the laser system is outside the deposition chamber. It requires little heavy equipment (with the exception of the laser) and makes it possible to work easily in small-sized chambers, thus it guarante high-quality deposition because they are little contaminated by residual impurities. PLD offers a very wide range

of material deposition due to flexibility in power and wavelength of the laser beam. It has been demonstrated that PLD allows control of the stoichiometry of the deposited layer depending on the composition of the target and any reactive gas (Dijkkamp ve ark., 1987). In addition, the high deposition rate of this technique allows us to produce high quality thin films or nanoparticles in short time range. At room temperature, by adjusting the deposition parameters we can synthesize crystallized thin films using this method.

Thus, PLD is a technique which serves as a relatively economical process compared to other competing thin film deposition techniques. Although it also has a certain number of limitations inherent to the process (deposition on small surfaces, inhomogeneity of the layers, emission of undesirable macroparticles in certain cases, etc.), it remains a technique that is widely studied in many laboratories.

In 2015, Ettlinger *et al.* (Ettlinger ve ark., 2015) used PLD technique to provide the first CTS thin films. After that at the same year, Vanalakar *et al.* (Vanalakar ve ark., 2015a) was able to reach a conversion efficiency of 0.82% using PLD to synthesize CTS thin films for the first time. Afterwards, a lot of research on the same trend have been published (Ettlinger ve ark., 2016; Raadik ve ark., 2017; Wang ve ark., 2017; Schou ve ark., 2018; Thota ve ark., 2019). For most of PLD experiments, the deposition was held using one single target of Cu-Sn-S.

3. MATERIALS AND METHOD

In this chapter we are presenting and explaining the preparation technique used in our theses to produce CTS based solar cells.

3.1. Ball Milling

For CTS powder we used the famous preparation method called Ball milling:

3.1.1. Mechanize of BM

Initially, when the grinding ball strike the metal powder it will cause a deformation resulting in flattening and hardening metal powder. The strong plastic deformation enhances the ratio surface/volume of particles following that a sizing down and shattering of these brittle powder takes place.

The commonly acknowledge explanation of alloying is the formation of intimate mix of constituent elements in different phases after milling the elemental powders. The formation of alloys is manifested by introducing multiple crystalline defects (dislocations, grain boundaries, vacancies, stacking faults, etc.…) into the material by the cold impact that causes also an instant elevation of temperature. Due to that, these defects along with rising the temperature form new phases from the raw elemental powders (seen Figure 3.1). In some cases, the formation of the required phase is not achieved, therefore a brief annealing treatment is required for the formation of the alloys (Suryanarayana, 2001; Suryanarayana ve ark., 2001; Suryanarayana, 2008; Suryanarayana, 2019).

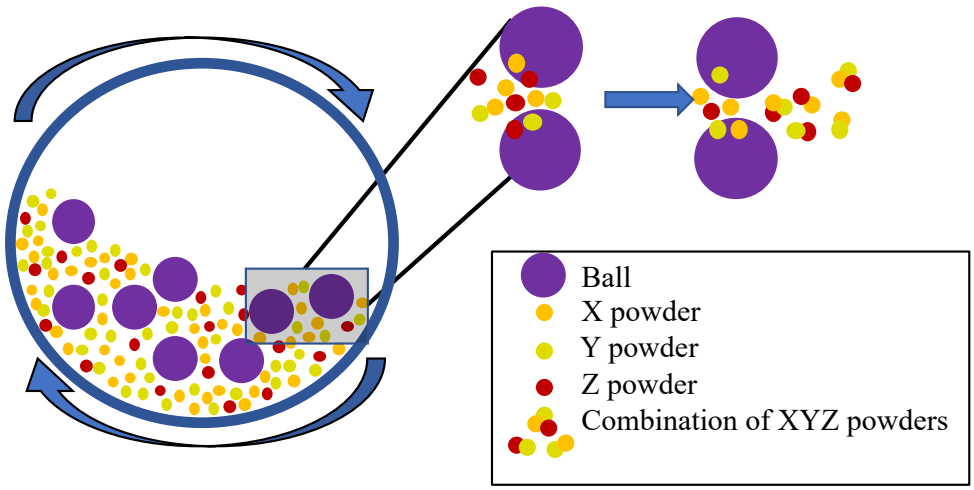

Figure 3. 1. Schematic image of the mechanical alloying of powders

As we previously mentioned, two types of grinding are used; dry and wet. In the wet mechanical alloying a certain quantity of surfactant is mixed with the powders and balls in the milling containers. The surfactants (PCAs: process control agents) can be organic or inorganic and mostly likely in liquid state. These substances cover the surface of the grinded particle. During the BM, fragmentation processes will form new surfaces that are also shield by PCA to prevent the cold weld and agglomeration. Due to that, the resulted powder particles are more refined with a usually amorphous structure (Nouri ve Wen, 2014; Neamţu ve ark., 2016).

3.1.2. Parameters of BM

Many different parameters can affect the BM process in positive or negative way according to the desirable final product. In the next statement, the effect of the most essential BM parameters is discussed:

3.1.2.1. Ball-to-Powder ratio

Ball-to-powder ratio (BPR) is one of the most important parameters in the milling process. At a low BPR the collision frequency decreases and this will decrease the energy introduced into the milled powder. On the other side, at high BPR, the mean free path of the ball's motion reduces while the energy consumption increases. However, the high BPR increases the iron contamination from the milling balls. Due to that, optimized BPR is required. The average BPR values are from 5:1 to 30:1.

In order to choose the suitable BPR we can rely on the following rules:

- The volume of grinding media (balls) = 50% of the vial's volume.
- The material charge occupies almost 25% of the vial's volume for best results.

Depending on these rules we can actually deduce the ball to powder ratio used in our case. It is very important to constantly check our milling medium because the volume of most the materials reduced when the size of the particles reduces (Gers, 2009).

3.1.2.2. Speed

RPM (rotation-per-minute) is usually the unite used to express the grinding action inside a mill or in other expression the mill shell's rotation speed. When the speed is very far from its optimum value it effects negatively on the resulted product. For instance, a low speed will extend the time of grinding to >100h at the same time a large inhomogeneity is observed. On the other hand, at a high rotation speeds the balls are stuck to the inner walls

of the vial where they can't fall down to produce any kind of impact force. Also, the high RPM leads to a temperature augmentation of the medium and also a high probability of contamination.

The recommended speed (V_R) depends on grinding condition like the ball diameter & the mill shell size:

$$V_R = 2/3V_C \quad \textbf{Eq 3. 1}$$

V_C is the critical speed calculated by:

$$V_C = \frac{42.3}{D-d} \quad \textbf{Eq 3. 2}$$

D: Diameter of the mill shell.

d: Diameter of the balls.

3.1.2.3. Grinding time

The time of milling or grinding is the most important parameter in the BM process. However, this parameter is related directly to the type of milling, speed (rpm), BPR and most importantly to the desired final powder phases. Therefore, identifying the parameter must be depended on the combination of the other parameters. Very long milling times are not favorable due to the possibility of contamination. Therefore, it is preferable to adjust the milling time just to reach the desirable powder phase and not any longer.

3.1.2.4. Atmosphere

Along the size reducing process the possibility of a chemical reaction with the O_2 or H_2O particle that exist in the air is very probable. So, in order to protect our raw material, it is preferable to use an inert atmosphere like N_2 or Ar or use the wet milling.

3.1.3. The used Ball milling equipment

For powder mechanical alloying, the used ball milling system is the Desk-top high-speed vibrating ball mill (see Figure 3.2). This system is a vibratory ball milling type where the vial rotates at a 45° angle of the rotation axe. Thus, this 3-dimensional movement assure a rotation, oscillation and vibration of the powders for better results in short time range. The device principally composes of two parts rotation motor and a vial holder.

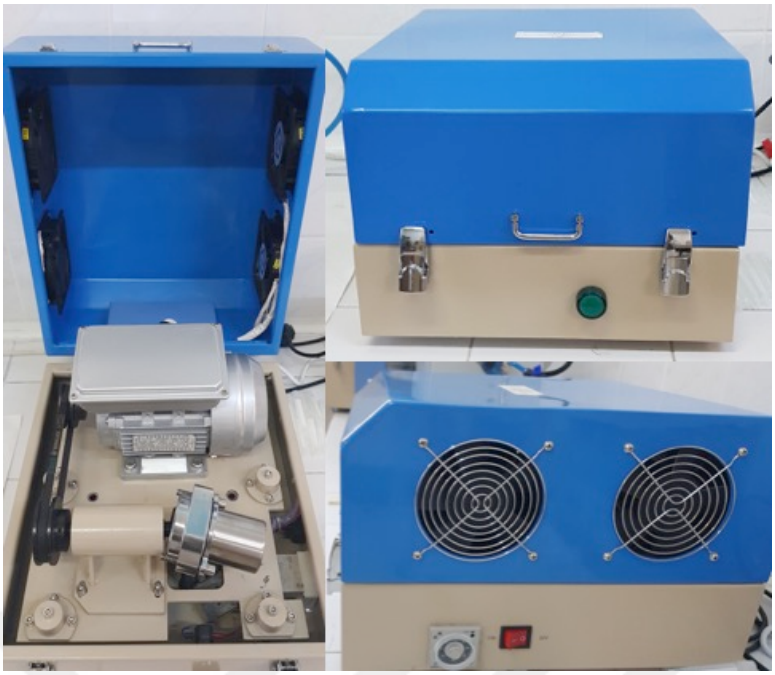

Figure 3. 2. Desk-top high speed vibrating ball mill

Between the two part a ribbon is installed to grantee the rotation of the vial. The system is enclosed in a box that contains 4 fans for cooling the motor and the vial due to elevation of the temperature during the grinding process. The rotation speed of our system is fixed at 1400 RPM and the timer is fixed to 30 min of milling.

Figure 3. 3. Image of the BM Vial (container) and grinding balls

The vial of our system is made of stainless steel, and it has a cylindrical shape with a cone at one end. The vial can contain up to 100 ml volume. The balls of the grinding are also made of stainless steel, and they all have the same diameter of 3mm (see. Figure 3.3). The vial is well closed where dry and wet grinding is available.

3.2. Target Production

In PLD system, the density and form of the target is very important as it effects the quality of the deposited thin films. If a porous target is expose to the laser beam, large atomic clusters will be easily ablated from the target and deposited on the substrate. Consequently, the deposited films will have a bad quality with no epitaxial growth. Therefore, a well condensed, homogenous and compact target is required for the PLD system (Zhou ve ark., 2010; Moholkar ve ark., 2011; Chen ve ark., 2012; Ullah ve ark., 2014; Ettlinger ve ark., 2015; Dong ve ark., 2016; Ettlinger ve ark., 2016; Raadik ve ark., 2017; Yadav, 2018). In this process, the elaboration is divided into three main steps:

3.2.1. Calcination

It is a thermal treatment that can have a very important contribution to the phase transition process and the removal of the volatile atoms. Calcination is done at high temperature to allow inter-diffusion of the ions existing in the raw materials by solid state reaction (Wang ve ark., 2011).

3.2.2. Uniaxial pressing

For PLD target production we need to compact the powder in a cylindrical disc using uniaxial pressing. The uniaxial pressing process starts by the filling step. In this step, the powder is poured into a shaping die containing a lower punch (Figure 3.4). An operation of vibration of the die allows a better packing of the powder. After that, the upper punch is places genteelly on the powder. The matrix is placed then inside the pressing machine. The second step is the compression. The pressure is applied to the upper punch that slides in the die to densify the powder (Figure 3.4). During the compression, the granules move by sliding or rotating to form a denser packing by elimination of the porosity between them. In this stage, the spherical granules will rearrange and deform to remove of the intergranular porosity in the granules. At the end of pressing, the particles can no longer slide past one another until reaching a critical minimum size (Reed, 1995; Boch, 2001). The pressing should be applied genteelly and removed genteelly. At the end of this process, the resulted product is called green pastille (target) and it often needs a heat treatment to densify.

Figure 3. 4. The target shaping system (die and punch)

3.2.3. Sintering

The sintering is a thermal treatment where our green pastilles are placed in a controlled atmosphere under high temperature. The annealing process will help the atoms to rearrange and densify for more rigid target. If the sintering process is done at very high temperature and for a long-time duration, solid state reaction will mostly take place to produce new phases of the treated powders.

Figure 3. 5. Hydraulic Pressing machine

All the pallet targets were pressed in a home-made mould (die) produced in KONYA SANAYi (Konya industrial zone) presented in Figure 3.4. And we used a hydraulic pressing machine in Figure 3.5 to apply a controlled pressing force.

3.3. Pulsed Laser Deposition technique

The deposition of the CTS thin films was all done using the PLD technique. In this section, we give a brief explanation of PLD technique and introduce the system exist in our laboratory.

3.3.1. The PLD system for CTS thin films deposition

The general structure of PLD system that has been designed and built in our laboratory is demonstrated in Figure 3.6. This system is currently active and in well-conditioned for the deposition of thin films, nano-materials and plasmonic nano-particles. This system was completely constructed in local industrial facilities in KONYA (see Figure 3.7). Our group hold the required mechanical and electrical technical knowledge that ensures us a complete control of the system in case of any unexpected damage.

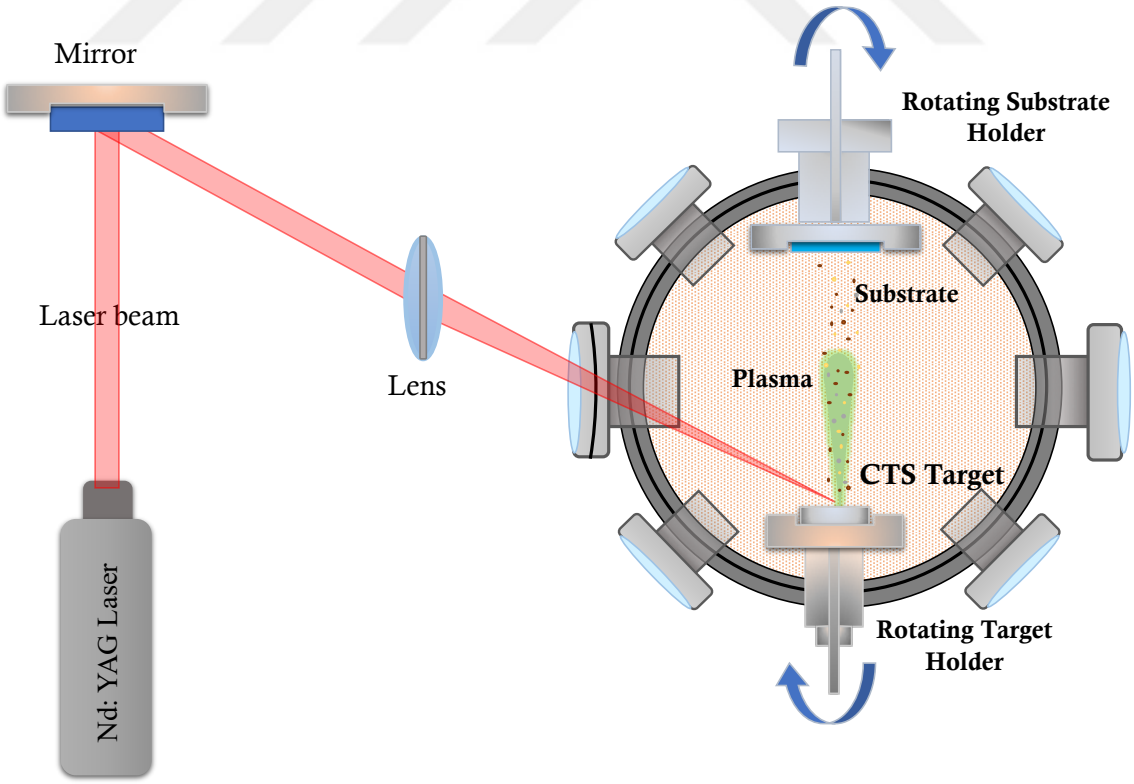

Figure 3. 6. Schematic image of PLD system

This thin film growth technique uses a pulsed photonic or laser as an energy source. In a low-pressure environment and by the help of focusing lenses and mirror, the intense nanosecond Nd:YAG laser beam is directed towards a solid target material (metal, alloy, ceramic, organic…). The target material the interaction between laser beam and the target material will produce a very energetic plume that contains energetic particles that will recondensed in the opposite side on the substrate surface.

The target and the substrate holders are in a constant circular movement with the help of two step motors placed facing each other. The deposition of the thin films in this system will assure a longer life for the target, production of a homogenous ablated plume as well as a homogenous deposition of thin films and a uniformed thickness. These two motors turn in different constant speeds (1-100 rot/min) thus, the laser beam is not always focused on the same spot and the damage of target is minimized (Willmott ve Huber, 2000; Ashfold ve ark., 2004; Gezgin ve ark., 2018; Houimi ve ark., 2021).

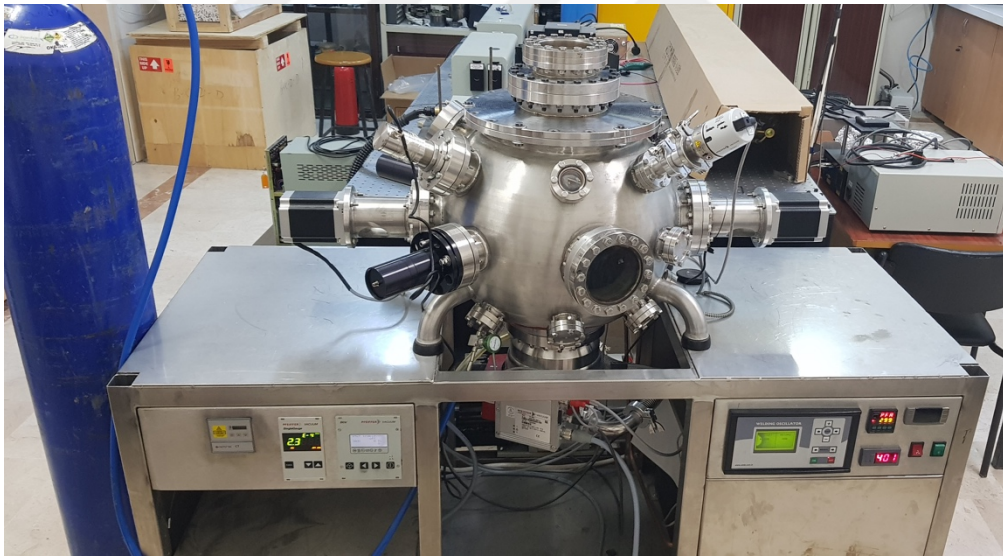

Figure 3. 7. The PLD system front view and general design.

The target-substrate distance is flexible and can be varied from 2.5 cm to 10 cm according to the plasma volume and deposited materials.

The deposition chamber along with the vacuum system, vacuum pumps, the essential power sources and all the control units are well positioned on a wheeled table that can be carried and moved from one to our other laboratory where our Femtosecond Laser system is located. With this facility, we are able to use both nanosecond (ns) (Figure 3.8) and femtosecond (fs) (Figure 3.9) laser pulses as sources for the ablation process.

Figure 3. 8. ns- Minilite II (Nd:YAG) laser systems

In our laboratory, we are currently using two nanosecond lasers: Continuum-Surelite III and Minilite II (Nd:YAG). According to the experiment's requirements, we can alter the wavelength and the power of these lasers as desirable. Also, during the experiments, if any unfortunate circumstances occur to one laser system the other system can operate immediately as an alternative. The working parameters of the two lasers are presented in the following Tables 3.1 and 3.2:

Table 3. 1. ns- Continuum-Surelite III (Nd:YAG) working parameters

Wavelength	Frequencies abilities	Pulse-width	Power (Max.)
1064 nm (1. Harmonic)	10 Hz	5 ns	850 mJ
532 nm (2. Harmonic)	10 Hz	5 ns	425 mJ
355 nm (3. Harmonic)	10 Hz	5 ns	225 mJ

Table 3. 2. ns- Minilite II (Nd:YAG) working parameters

Wavelength	Frequencies abilities	Pulse-width	Power (Max.)
1064 nm (1. Harmonic)	1-15 Hz	5 ns	42 mJ
532 nm (2. Harmonic)	1-15 Hz	5 ns	20 mJ
355 nm (3. Harmonic)	1-15 Hz	5 ns	10 mJ
266 nm	1-15 Hz	5 ns	4 mJ

Due to the moving deposition chamber, we can also use fs laser system located (see Figure 3.9) in our other laboratory.

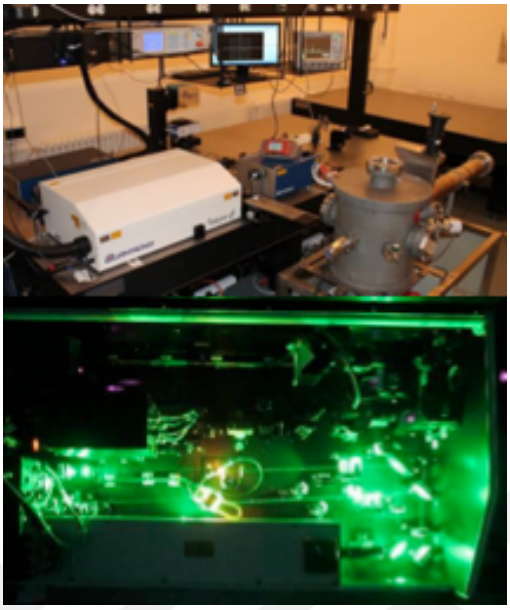

Figure 3. 9. Femtosecond laser system

The pressure in vacuum chamber, target-substrate distance, laser energy, etc. are always a subject to change in order to find the proper deposition parameters. In our previous works, our PLD system was able to conduct great results in the deposition of ZnO, CZTS, and CdS thin film successfully. These thin films were used in solar cell & diode devices. We can also use it to produce plasmonic nanoparticles to get plasmonic effect on the absorber thin films as we have observed and published before (Houimi ve ark.; Gezgin ve ark., 2016; Gezgin ve ark., 2018; Gezgin ve Kılıç, 2019; Houimi ve ark., 2021).

3.4. Annealing and preserving Processes

The wet milling powders, the pressed target (green pastilles) and the thin films synthesized by PLD require temperature treatment in controlled vacuum or gas atmosphere. In our laboratory, we provide a quartz oven for various annealing usages as present in Figure 3.10. The oven is constructed of cylindrical quarts glass tube with two enclosed endings. The first edge is for the entrance of gases and it is connected to the gas sources (Argon (Ar), Oxygen (O_2), Azote (N_2) …). As for the second one, it is linked with the vacuum pomp for the gas evacuation. The heating system is a resistance that surround all the quartz tube with a thermocouple to control the temperature. The temperature regular allow us to regulator the temperature elevation speed and uphold

duration for as many stages as we want. The temperature maximum increasing speed is 10 K°/min and the oven maximum temperature is 1100°C.

Figure 3. 10. Quartz vacuum oven

The thin films and silicon wafers are very delicate and sensitive to many factors such as time and atmospheric precipitations and gases. Therefore, to preserve the thin films from any oxidation harm or damage from the surrounding atmosphere, we saved them in enclose vacuum chamber present in Figure 3.11.

Figure 3. 11. Vacuum chamber

3.5. Physical Vapor Deposition (PVD) Technique

For the front and back contacts thin films of our CTS based solar cells, we have used the PVD technique. This technique involves the evaporating by bringing it to high temperature and then depositing it on a substrate. The component to be deposited is

known as the source. This source is heated to a high temperature until it reached the liquefaction. As soon as the liquefaction temperature is exceeded, it turns out that the pressure of the material is significantly higher than the residual pressure in the enclosure (vacuum chamber). Under these conditions, atoms of the material migrate and propagate until they encounter an obstacle. This meeting can be the result of a solid surface (substrate, wall of the enclosure) or an atom or molecule moving in space (reactive gases such as O_2). In the case of the encounter with a surface, the atom stays on the surface where energy exchange takes place. If the surface is noticeably colder than the incident atom, there is definitive condensation and growth of a thin films.

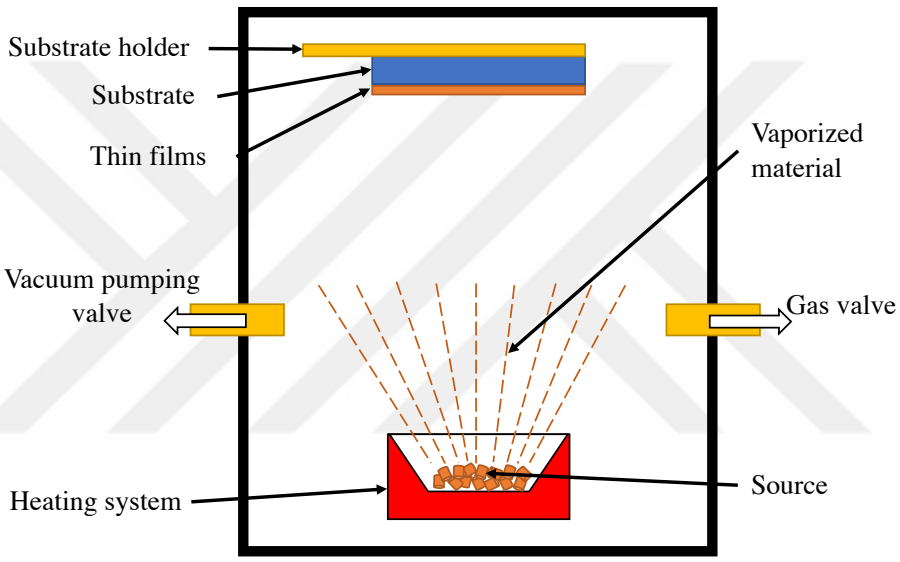

Figure 3. 12. Schematic image of PV system

The procedure for heating the material to be evaporated can be carried out in several ways, which will be chosen in accordance with the nature of the material to be deposited and the desired quality criteria. The most common method is the use of a pot heated by the Joule effect, however this process is limited to materials evaporating at relatively low temperatures (below the melting temperature of the crucible) to avoid any contamination from the container. A second technique consists in using an electron gun with electromagnetic deflection (Electron Beam PVD, EB-PVD) allowing in theory the evaporation of any material without risk of pollution by the support. In general, evaporation techniques make it possible to produce homogeneous films (without contamination), with a thickness of a few nanometers up to a micrometer on large substrates (10 to 18 cm in diameter). However, the layers produced are generally more

porous compared to other deposition techniques such as pulsed laser ablation, which can be a drawback for certain applications. Nevertheless, heating the substrate during the production of the films and/or performing post-deposition annealing can reduce the porosity of these materials. Also rotating the substrate are commonly used to enhance the homogeneity of the thin films.

The principle of evaporation technique and the image of the used deposition chamber are illustrated in Figure 3.12 and Figure 3.13, respectively. The system is thus composed of the following elements:

- *A deposition chamber:* made from glass or stainless-steel enclosure with a sealed seal, capable of withstanding large pressure differences and thermal variations.
- *A pumping system:* the high vacuum is obtained in two successive stages, primary and secondary pumping which makes it possible to obtain very low pressures in the containment (10^{-5} up to 10^{-10} Pa).
- *A heating system:* which consists of a heating source and a pot which contains the material to be deposited.

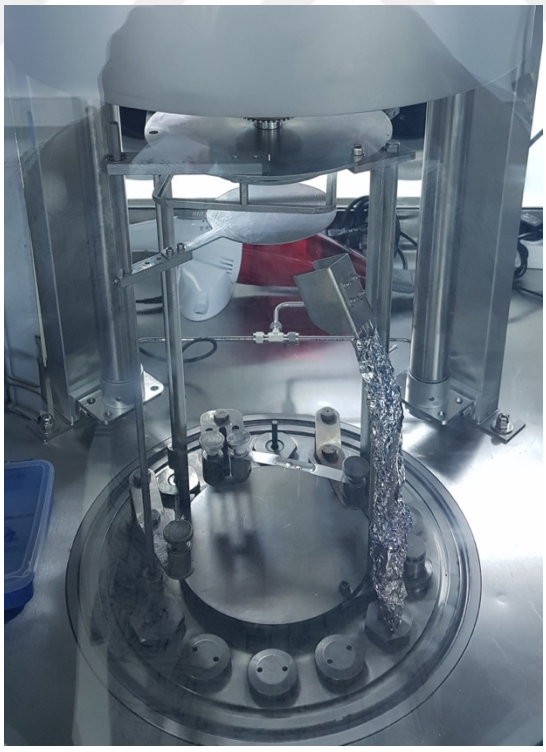

Figure 3. 13. Image of PVD system.

3.6. Characterization of thin films

The analyze of the different properties of powders targets, thin films and solar cells required a group of analyze devices that are cited in this section.

3.6.1. X-ray diffraction (XRD)

The X-ray diffraction analysis technique is based on the elastic interaction of a monochromatic beam of X-ray photons with the crystal lattice of a material. For an electromagnetic wave to be diffracted by the crystal, the wavelength of the incident photons must be of the same order of magnitude as the distance between the atomic layers (inter-plane) of the material. The resulting diffraction diffractogram allows us to have different information about the crystal structure of the material. According to the intensities and the angels of the XRD pattern we can investigate the crystal structure of a material, the inter-distance space between layers, lattice parameters, size, shape and internal stress in the crystal. Bragg's law defines the relationship between the wavelength of the incident beam (λ), the lattice parameter identified by the Miller indices (*hkl*) and the diffraction angle (θ), the natural integer n representing the diffraction order.

Figure 3. 14. Image of XRD analyses system.

The used apparatus is a BRUKER D8 ADVANCE X- Ray diffractometer (Figure 3.14). It is coupled to a computer performing the automation of angular scans and recordings. The X-ray source uses a wavelength of λ= 1.5428Å. D (crystalline size), ε (micro-strain) and δ (dislocation density) of the produced powders targets and thin films are calculated using the following equations (Prabhu ve ark., 2015; Reddy ve KUMAR, 2019):

$$D = 0.94\lambda/\beta cos\theta \qquad \textbf{Eq 3. 3}$$

D is the main size of crystalline composing the thin films, θ is the diffraction angle and β is the full-width at half-maximum of diffraction main peak

$$\delta = \frac{1}{D^2} \qquad \textbf{Eq 3. 4}$$

$$\varepsilon = \frac{\beta cos\theta}{4} \qquad \textbf{Eq 3. 5}$$

3.6.2. Scanning Electron Microscopy (SEM)

The principle of an SEM is to subject the surface of the sample to be analyzed to an electron beam (whose energy can vary from 1 keV to 40 keV). At each point, the interaction between the electron beam and the sample generates secondary and/or backscattered electrons which escape from the sample. They are then collected towards different types of detectors for secondary electrons and for backscattered electrons which amplifies the sensed signal.

Figure 3. 15. Image of SEM analyze device.

The only electrons that can be collected by the detectors are often emitted at a depth of less than 10 nm (electrons from deep layers cannot escape). Depending on the electrons collected, we have access to different information (morphology, thickness, etc.).
SEM analysis is a non-destructive method but requires metallization in the case of dielectric samples. SEM is therefore very useful for the morphological analysis of many films. In our study we used a "ZEISS EVO LS10" SEM microscope model present in Figure 3.15.

3.6.3. Energy Dispersive X-ray Spectroscopy (EDX)

Energy dispersive X-ray spectroscopy (EDX) is an analytical technique used to characterize material's chemical composition. In most cases, this tool is linked to an electron microscopy device, generally scanning electron microscopy (SEM). The working principle of, EDX device is based on detecting the emitted X-rays from the investigated simple after focusing on it a beam of high-energy charged particles (electrons or protons). The elemental composition of the analyzed sample is associated with the peaks in the EDX spectrum. This characterization approach may also be used to produce a sample's elemental mapping.

3.6.4. Raman spectroscopy

Raman scattering spectrometry is a technique for observing the vibrational states of a molecule based on the phenomenon of Rayleigh scattering. When the incidence monochromatic beam of visible, near-infrared, or near-ultraviolet light is focused on the material, it mainly diffused in an elastic way, this is called the "Rayleigh scattering". However, a tiny part of the radiation is scattered inelastically, either with higher energy in the case of Raman anti-Stokes scattering, or with lower energy in the case of Raman Stokes scattering. The vibrational energy levels of the examined molecules are represented by the difference in the energy between the incident photons and those released inelastically by the sample. These vibrational energy levels presented as peaks in the detected spectrum of Raman analysis where the energies are expressed here in wave number. If we analyze the modification in spectral lines caused by the Raman effect, we can reveal details about the sample's chemical makeup and the crystalline structure. Raman spectroscopy is widely used as a complement to XRD to characterize the compounds of a materials. This technique allows in particular the search for impurities, including in small quantities. The Raman device model used in this experiment is

RENISHAW Raman Microscope with 532 nm excitation wavelength and a laser power of 1.5 mW.

3.6.5. UV-Visible-NIR spectrophotometry

UV-Visible-NIR spectrophotometry is based on the effects of matter-electromagnetic radiation interaction in the operating range extending from near UV to very near IR.

The absorbance of materials in the near UV and the visible which is due to the passage of electrons from an electronic level to another level of higher energy, makes it possible to provide information on the optical properties of these materials such as: index of refraction, absorption coefficient (α), optical bad gap (E_g) and the layer thickness (W). The photometric coefficient that we have measured is the absorbance A.

To extract the absorption coefficient (α)from the absorbance we use the following relation (Mustafa, 2013; Antar, 2014):

$$\alpha = 2.303(A/T) \qquad \textbf{Eq 3. 6}$$

The band gap energy of a direct gap semiconductor E_g is calculated from the following relationship:

$$(\alpha h\upsilon)^2 = A(h\upsilon - E_g) \qquad \textbf{Eq 3. 7}$$

Measurements of absorption was carried out using the CRTSE using a “Cary500” Spectrometer.

3.6.6. Profilometer

Thickness of the deposited thin films is very important data giving us lots of info about the properties of our films and its behaviour in the solar cell devices. Profilometer is a displacement sensor device. It provides us information about the thickness and the roughness of the analysed thin films. The working mechanism of profilometer is based on removing the sample from the substrate using the probe tip. The stylus will scan the surface of the sample with a predefined speed and area. Along the scanning process the stylus will move in a vertical direction up and down according to the surface roughness sending by that an electric signal that will be converted to surface properties. Measurements of thickness was carried out using the CRTSE using a “Cary500” Spectrometer.

3.6.7. Characterization of solar cells (Current Density-Voltage (I-V) Measurement)

The I-V measurements allow the determination of the conversion yields η and the electronic properties of the PV cells. I-V measurements under illumination consist in measuring the current of a cell as a function of the voltage applied to its contacts (back and front). The measurements were carried out in a enclose glove box using source meter (Keithley 2400 Model) and a solar light spectrum simulator (80 mW/cm2 light intensity and AM 1.5 terrestrial solar spectrum) presented in Figure 3.16. I(V) measurements in darkness consist of carrying out the same means as that described under illumination but when the device is in complete darkness.

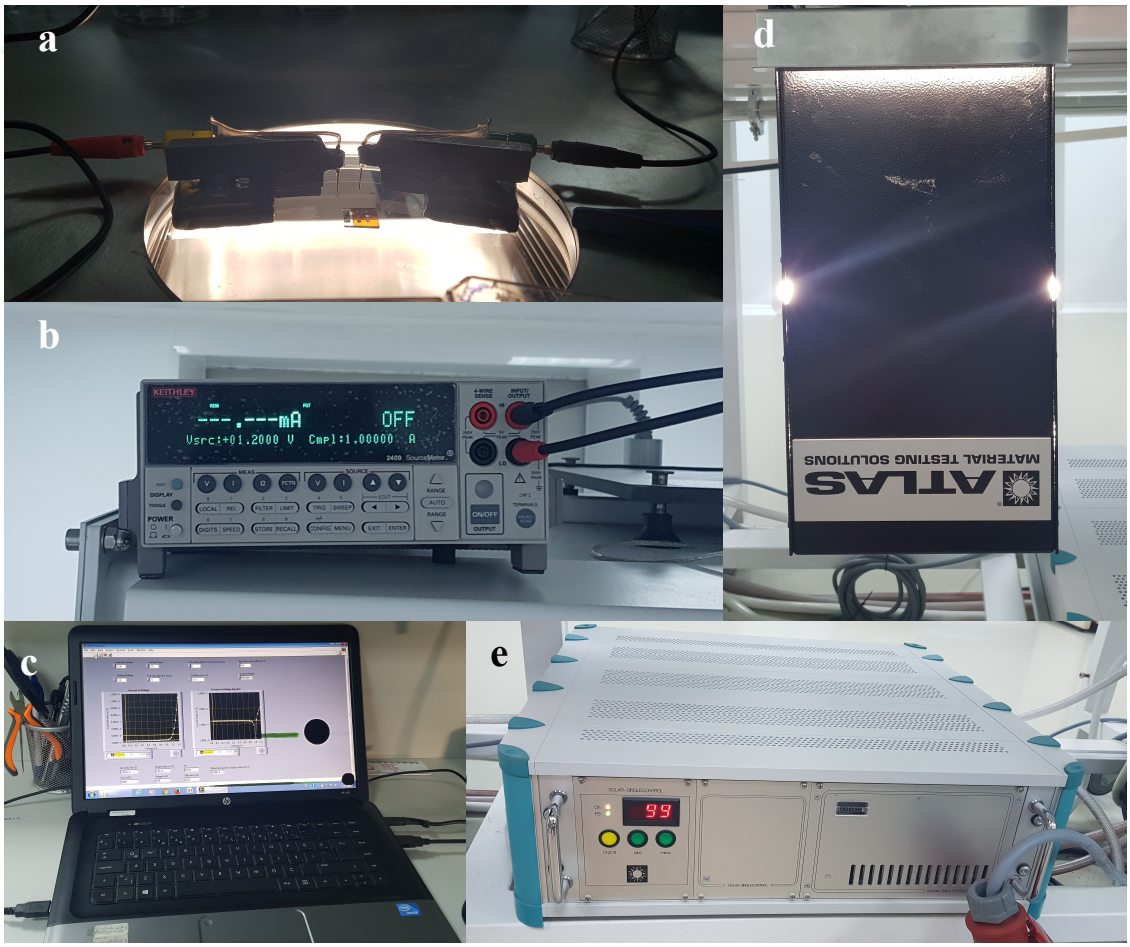

Figure 3. 16. Images of the different parts of I-V measurement system a) Anode and cathode for data collection, b) Keithley source meter, c) Data accusation interface, d) Solar simulator and e) Light source powering system.

4. Research Results and Discussion

In chapter 02, the required theoretical background of semiconductor materials has been provided and more specifically the big focus was on CTS materials. While in chapter 03, we explained and displayed the used methods and techniques to synthesize CTS material. Finally, we present in this chapter the deposition and fabrication details as well as the acquired analyses and measurements results of CTS powder, targets, thin films, and solar cells. At first, we will start by presenting CTS powder:

4.1. CTS Powder

In this part the preparation and properties of CTS powder were presented.

4.1.1. Experimental Process

CTS powder was made by BM (ball milling) method using elemental raw pure materials in powder form. Copper (Cu) and Tin (Sn) powder were purchased from Alfa Aesar with a purity of 99.9%. As for the Sulfur (S) powder we purchased it from TEKKİM KIMYA SANAYI, with a purity of 99%. To prepare the powder we weighted a 10 g of CTS powder with the following elemental ratios: Cu:Sn:S=2:1:3. The CTS powder was placed in the vial with 100 g of grinding balls of 3 mm. With these proportions, the BPR (ball to powder ratio) is 1:10. The ball milling was not dry as known in most of the CTS work. In our case, we used wet milling by pouring 10 ml of ethanol into the container before the beginning of the process. In the experiments, the ethanol covered all the grinding medium with the raw powders (see. Figure 4.1.a).

The BM was set for 6h separated into 30 min time interval. After 30 min of milling, we waited until the vial cooled down to prevent any temperature elevation that can cause contamination of the powder from the grinding balls or the vial. The milling speed is fixed at 1400 RPM (round per min). After 6 h of milling, the mixture was obviously wet and in need of drying process. We placed the CTS mixture inside the quartz oven of 80°C fixed temperature and under Argon gas atmospheric pressure for 24 h. To ensure the fast drying of our powders, we circle the Ar gas (see. Figure 4.1.b) into the oven. The resulted powder was analyzed using XRD to understand the effect of the BM process.

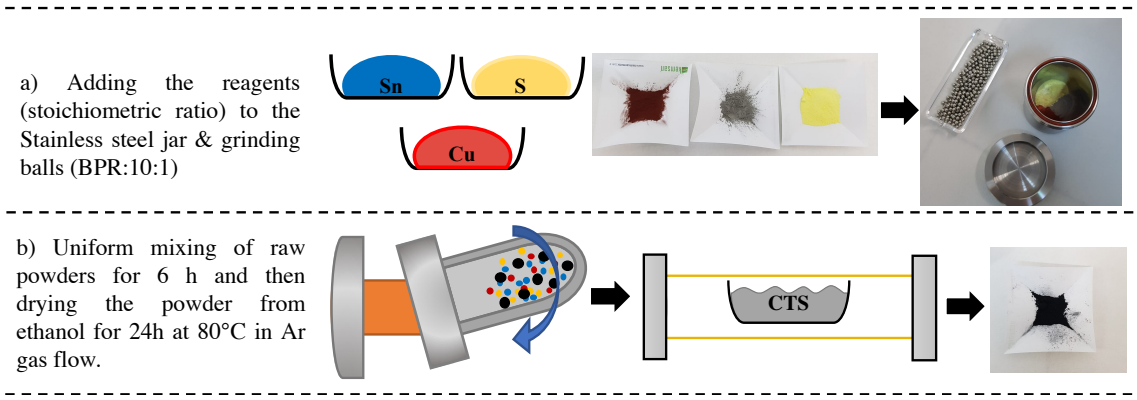

Figure 4. 1. Schematic image of CTS powder Ball milling process

In our work, we choose wet milling for two reasons basically. The first one is due to the small size of the resulting particle powders after wet milling compared to dry milling. The small particle size is an important quality for compact and PLD targets. The second reason is due to the high speed of our BM device that can't be modified in our case. Due to centrifugal force, at high-speed of 1400 RPM the milling will be immovable at the inner walls of the vial where they can't fall down to cause any kind of impact or grinding to the powder. Therefore, we added Ethanol to enhance the milling process.

4.1.2. XRD:

We investigated the crystallinity of CTS powders before any annealing treatments and the XRD pattern is present in Figure 4.2. Two different crystalline phases appeared in this pattern. The first one is CuS hexagonal phase (Reference data: ICDD 00-006-046) and Sn hexagonal phase (Reference data: ICDD 00-001-0926).

This signifies the direct reaction between Cu and S since no peaks corresponding to Cu precursor were detected. This mechanochemical reaction is expected due to fast reactivity between Cu and S (Baláž ve ark., 2016). As for the Tin (Sn) precursor, we suppose that it didn't react with S nor with Cu atoms and consequently we detected it in the XRD diagram. The development of this reaction was suggested previously by Baláž *et al.*(Baláž ve ark., 2018) in Equation 4.1:

$$2Cu + Sn + 3S \rightarrow 2CuS + Sn + S \qquad \textbf{Eq 4. 1}$$

However, the expected Cu_2SnS_3 phase didn't appeared after the 6 h of ball milling process. In many previous works, it has been stated that ball milling process can be insufficient to achieve a complete mechanochemical reaction to reach the required CTS phase (Cu_2SnS_3) (Nomura ve ark., 2013; Hegedüs ve ark., 2018). The most probable

explanation for that in our case is the use of wet milling. A surfactant (ethanol) will reduce the contacts probability between the different reactants (Cu, Sn and S) during BM process. This will decrease the reaction rate and slow down the formation of CTS material (Kozawa ve ark., 2021). Therefore, the annealing process is required to achieve the wanted CTS phase.

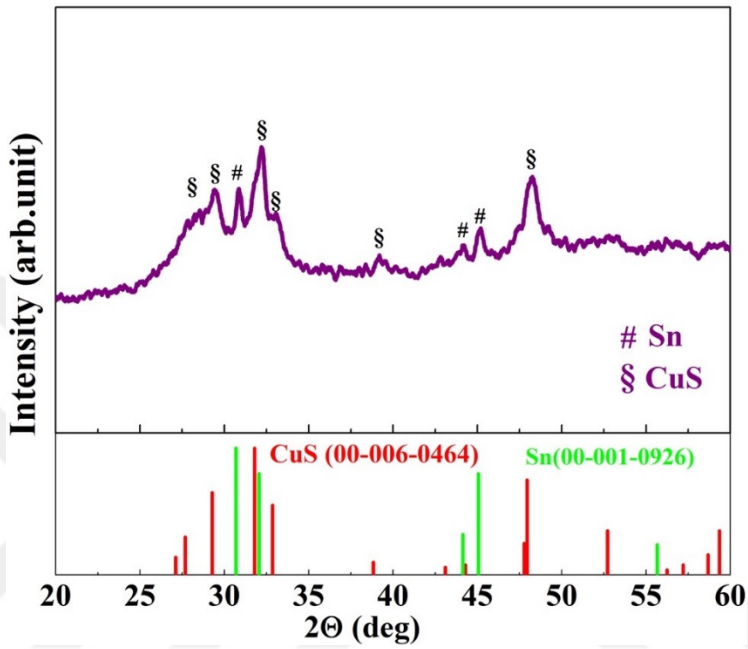

Figure 4. 2. X-Ray diffraction pattern of CTS powder after ball milling process

4.2. CTS Targets

The CTS powder resulted from the ball milling and then dried for 24h at 80°C is going to be formed into a target pallet shape specifically for the PLD system to synthesis CTS thin films.

4.2.1. Experimental process

In order to prevent the waist and the excessive consumption of matter, we chosen to use low diameter targets (12 mm) with small thickness. We only utilized 700 mg of CTS powder for each target. The powder was first weighted with a microbalance and then we poured it into a small agate. The powder is genteelly grounded to remove any agglomerations that were formed during the drying process (see. Figure 4.3.a). The 0.7 g of powder was then poured into the mold and then shaken a little bit to uniform the powder inside it. Afterwards, the mold was placed under high pressure of 19 MPa for 5min and later the pressure was removed gently. The resulting green pallet is immediately placed

with 100 mg of S powder in the quartz oven of atmospheric Ar gas pressure for the sintering process. The annealing treatment was set for 2h for 600°C for all the targets (see. Figure 4.3.b).

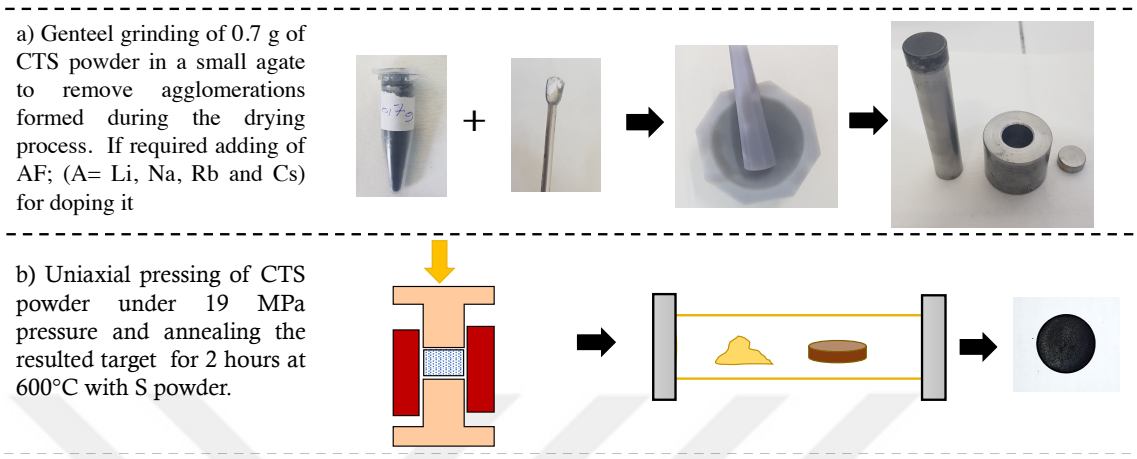

Figure 4. 3. Schematic image of CTS targets doping and pressing processes

For the doped CTS targets, the doping stage was held after the BM and before the pressing stages. The doping elements for CTS materials were alkali atoms; Li, Na, Rb and Cs. These atoms were introduced into CTS material in form of Alkali Metal Fluorides in form of AF; A= Li and Na. After the sintering, the F atom will evaporate in form of F_2 gas and only the alkali atom will remain in the CTS material lattice. The MF added quantities will define the concentration of the alkali atoms in CTS material. The added quantities in mole with extended chemical formula are present in Table.4.1.

Table 4. 1. The added MF quantities in mole and mg with extended chemical formula of $M_{0.0x}Cu_2SnS_3$

Added atom (M)	Chemical formula	Abbreviation	Added quantity in 1 mole of CTS (mole)	Added quantity in mg for 0.7 g of CTS (mg)
pure	Cu_2SnS_3	**TP**	0	0
Li	$Li_{0.01}Cu_2SnS_3$	**TLi1**	0.01	0.52
	$Li_{0.03}Cu_2SnS_3$	**TLi3**	0.03	1.56
	$Li_{0.05}Cu_2SnS_3$	**TLi5**	0.05	2.59
Na	$Na_{0.01}Cu_2SnS_3$	**TNa1**	0.01	0.84
	$Na_{0.03}Cu_2SnS_3$	**TNa3**	0.03	2.52
	$Na_{0.05}Cu_2SnS_3$	**TNa5**	0.05	4.2

4.2.2. XRD analyze

The XRD structural study focuses on the annealing temperature and how it can affect the formation of different phases of Cu-Sn-S alloys from CTS ball milled powder.

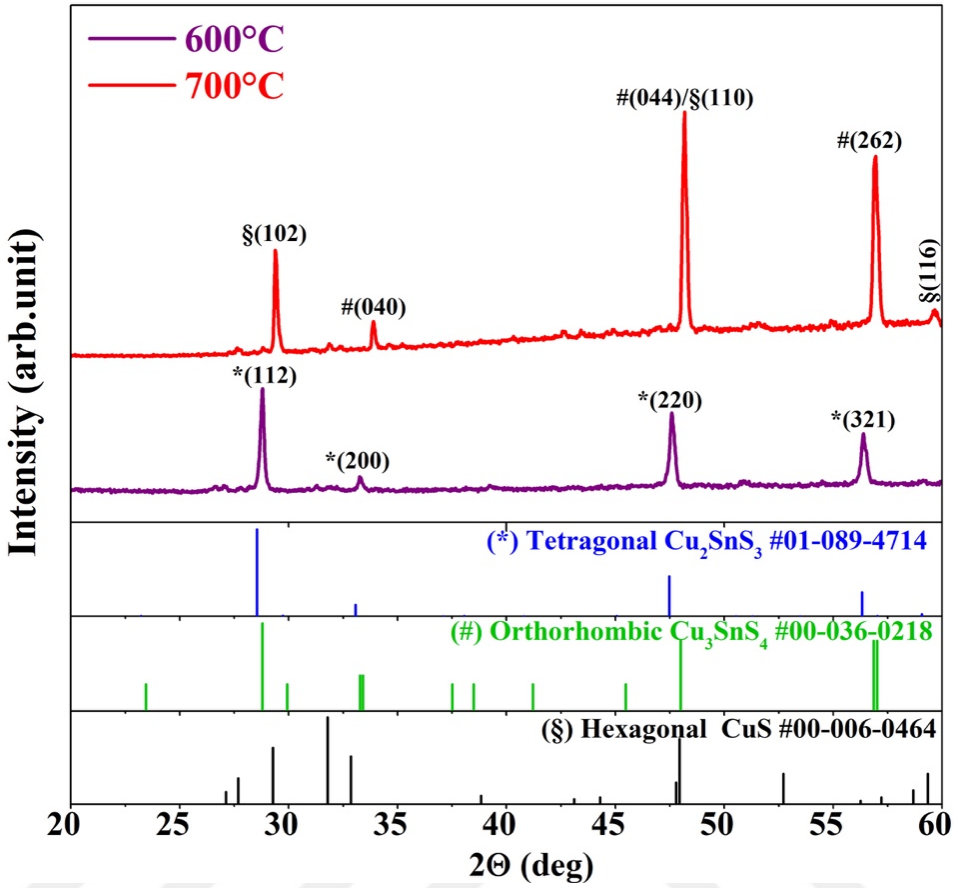

Figure 4. 4. X-Ray diffraction pattern of CTS targets after annealing at 600°C and 700°C.

Figure 4.4. presents the X-Ray diffractogram of CTS non-doped target TP after sintering treatment for two hours at different temperatures 600°C and 700°C. At 600°C, the XRD pattern presents one single crystal phase of tetragonal Cu_2SnS_3 (Reference data: ICDD 01-089-4714). The peaks are found at 2θ= 33.2°, 47.6° and 56.4° corresponding to (200), (220) and (312) planes respectively. The main peak is located at 2θ= 28.8° that signifies (112) plane. No sign of CuS or Sn phases indicate the total transformation of the powder precursors into CTS phase according to Eq 4.2:

$$2Cu + Sn + 3S \rightarrow 2CuS + Sn + S \rightarrow Cu_2SnS_3 \qquad \textbf{Eq 4. 2}$$

Rising the temperature to 700°C forms new phases in TP target that are signified by showing additional XRD peaks. According to the diffractogram of TP at 700°C, we observed the disappearance of CTS phase and the formation of copper rich phases; CuS and Cu_3SnS_4. The peaks of these two phases are situated at 2θ= 29.4° and 59.6°, that refer to (102) and (116) planes of CuS hexagonal phase (Reference data: ICDD 00-036-0218), respectively. Furthermore, Cu_3SnS_4 orthorhombic phase (Reference data: ICDD 00-036-

0218) appeared with two additional peaks at 2θ= 33.9° and 57° labelled as (040) and (262), respectively. As for the peak at 2θ= 48.2°, it might refer to the Cu_3SnS_4 (044), or CuS (110) planes. The formation of copper rich phases is due to the fast evaporation of SnS and Sn materials at high temperatures that leads to the deficiency of Sn in the target (Ettlinger ve ark., 2016). In the work of Namora *et al.*(Nomura ve ark., 2013), it was implied that if the annealing temperature of Cu_2SnS_3 excess 650°C, the material will decompose and copper rich ternary phases of Cu-Sn-S alloys will form such as Cu_3SnS_4 and Cu_4SnS_4.

As a conclusion, we propose 600°C annealing temperature as the most suitable for all CTS targets.

4.2.3. SEM-EDX analyze

To control the deposition quality of CTS thin films and their atomic composition, we conducted a pre-study of TP target. The results of its morphology and compositional analyses are given in this section. Figure 4.5. presents SEM images of two different sides of TP. Figure 4.5a that is a view from the front of a well-polished target surface (the front surface is the place where the laser beam hits the target). No visible cracks or grains do exist and the surface is well smoothed.

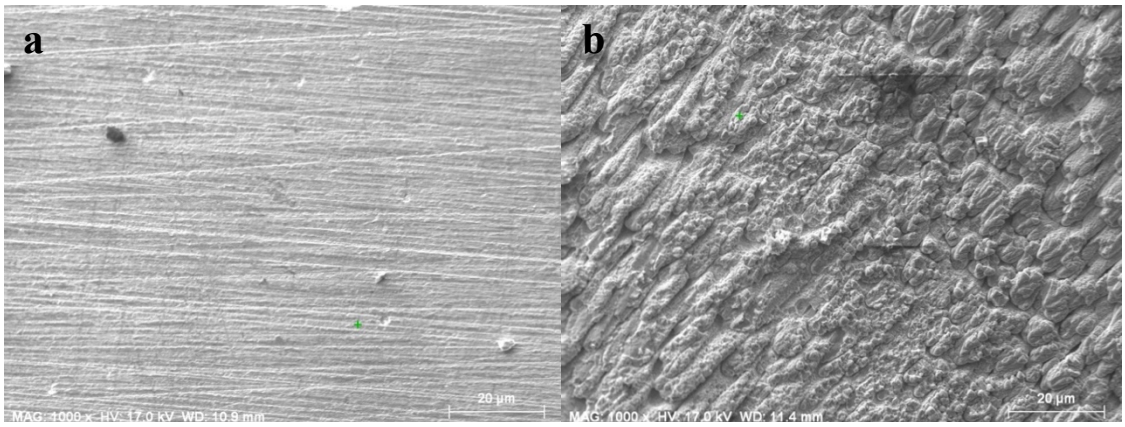

Figure 4. 5. SEM image of a) the fracture side and b) surface side of same CTS target (TP).

In Figure 4.5.b, the inside of the fracture target is presented. In the cracked side of the target, we do not distinguish any agglomerations or grains. These features can assure us well PLD target. For a PLD, the porous target damaged very fast and its laser ablation might result in some clusters of material that browns the thin films. Consequently, a well condensed target is required.

Table 4. 2. The atomic concentration of TP target

Samples	Cu (%)	Sn (%)	S (%)	Cu/Sn	S/Metal
TP	34.08	17.70	48.22	1.93	0.93

In Table 4.2, we have presented the atomic ratios in TP. TP contains the expected atoms that was added: Cu (Copper), Sn (Tin) and S (sulfur). In TP target the proportions of the atoms are nearly stochiometric. The ratio of S/Metals is 0.93, which is slightly less compare to the right stochiometric rate. The volatile nature of S atoms that dissipated during the 2h annealing procedure at 600°C is mostly the cause for the drop in S content in TP (Schou ve ark., 2018).

Given that the anticipated phenomenon was the evaporation of Sn atoms in form of SnS and copper rich targets, the targets excessive Sn content was surprising (Cu/Sn < 2). Similar outcomes were revealed for CTS targets and nanoparticles prepared using ball milling (Vanalakar ve ark., 2015c; Neves ve ark., 2016; Baláž ve ark., 2018). According to the work done by Hegedüs *et.al* (Hegedüs ve ark., 2018), it was highlighted that copper-poor CTS TP include a trace amount of CuS particle sample that EDX analysis is unable to resolve it. Thus; the EDX analyses of TP will reveal a copper-poor and tin-rich results. Despite this, we are unable to offer convincing proof that the Cu/Sn ratio becomes less than 2, due to changes in particle reactivity.

4.3. Undoped CTS Thin Films (Production and Analyze)

In order to perform a good CTS thin films, many different deposition parameters were investigated. The deposition parameters and the results of their different properties are given in this section.

4.3.1. Experimental process of undoped CTS thin films

The deposition of CTS thin films was done inside the vacuum chamber of PLD system. We used SLG (Silica Lime Glass) as a substrate for all the thin film. Before the deposition process the SLG and the CTS targets were carefully prepared for the deposition.

4.3.1.1. Preparation of SLG and CTS targets

The SLG was cut into equal samples of 2 cm long and 1cm width parts, using a roller. Then, the SLGs were cleaned with detergent and rinsed with distilled water. Subsequently

the slides were immersed vertically in acetone and isopropyl alcohol and cleaned for 15 min in ultrasonic bath, respectively. Prior to each experiment, SLG substrates were dried using N_2 gas flow.

Each experiment requires the preparation of the CTS homemade targets. The extra CTS powder is removed from the target's surface by first using sandpaper to smooth it out and then wipe it with acetone. This is done to ensure that the targets will have the same initial state throughout all experiments.

4.3.1.2. Deposition parameters of undoped CTS thin films

CTS thin films were deposited using PLD deposition system. In all our experiments, the utilized laser beam (Nd:YAG laser) parameters are the same. The wavelength of the laser beam is 1064 nm, the repetition-rate is 10 Hz and the pulse width is 5 ns. The laser beam was focused using a confocal less with a focal distance of 50 cm. The beam was then directed to a rotating CTS target to adjust the spot position. SLG were fixed on the substrate holder that faced the target with a parting distance of 40 mm. Afterwards the vacuum chamber was closed and evacuated up to a base pressure of 1×10^{-6} mbar.

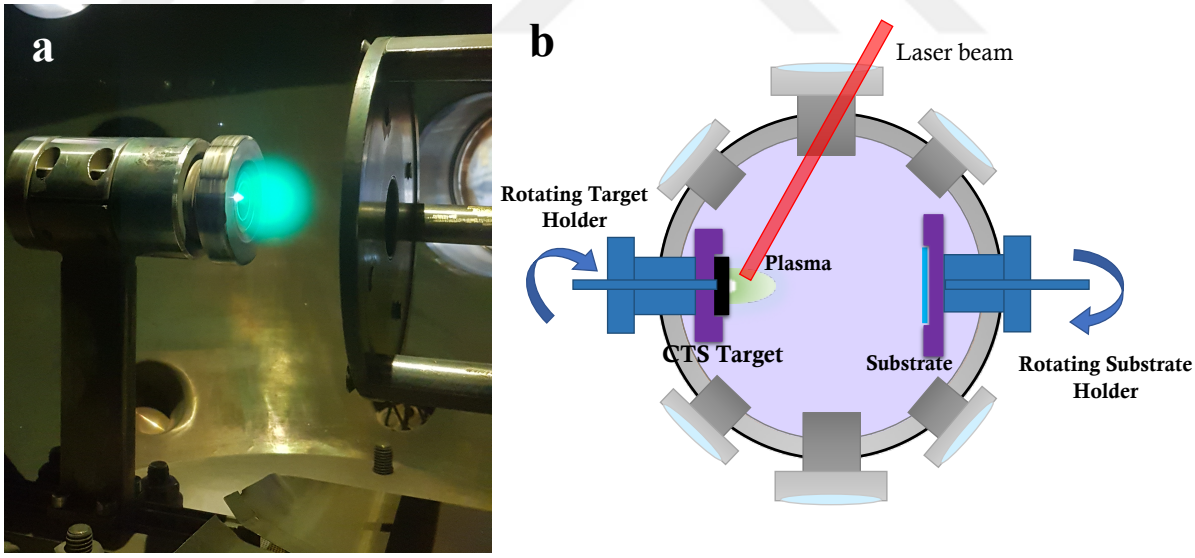

Figure 4. 6. A) Images of real CTS target plasma during the deposition and b) schematic plot of PLD system.

During the deposition process both target and substrate holders are rotating in a steady speed of 970 rpm and 960 rpm, respectively. This arrangement is important to preserve the targets from too much damaging and assure long experiences with homogenous deposition. The deposition time ranged from 2.5 min to 15 min. Figure 4.6.a, presents an

image of the CTS plasma plum during the deposition and in Figure 4.6.b we present a schematic graph of the PLD deposition chamber.

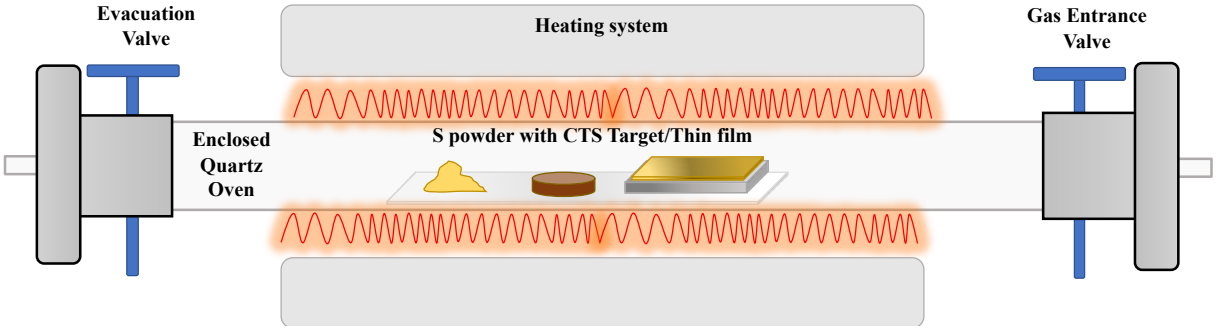

Figure 4. 7. Schematic image of quartz vacuum oven

The deposition process was all heled at room temperature. Therefore, to enhance the films crystallinity they must go through annealing process (sulfurization) at high temperature (from 400°C to 600°C) in vacuum quarts oven with the presence 50 mg of S powder next to the CTS thin films. In Figure 4.7, a schematic image of the quartz oven used for the annealing of the targets and thin films. The presence of S powder in all the annealing treatment is to compensate the lost in S element that happen at high temperatures due to the volatile nature of S atoms. The deposition parameters of all the CTS thin films are cited in Table 4.3:

Table 4. 3. List of CTS thin films with the different preparation parameters

Used target	Deposition time	Annealing temperature	Abbreviation
TP	2.5 min	500°C	F2.5
	5 min	500°C	F5
	10 min	500°C	**F10/F500/FP**
	15 min	500°C	F15
	10 min	0°C	F0
	10 min	400°C	F400
	10 min	450°C	F450
	10 min	550°C	F550
	10 min	600°C	F600

4.3.2. Effect of annealing temperature on different properties of CTS thin films

A crucial factor in forming CTS thin film is the sulfurization temperature, which influences its compositional, structural, morphological and optical characteristics. As a

result, the current study focuses on the effects of sulfurization temperature on the growth of CTS thin films.

4.3.2.1. Compositional properties (EDX) of undoped CTS thin films according to the annealing temperature

In Table 4.4, we present the elemental composition of CTS thin films with different annealing temperatures. At room temperature, F0 thin films have a high concentration of copper atoms and low ratio of S atoms (S/(Cu+Sn)=0,63). The evaporation of this atom may be the cause of S loss during the deposition of Cu_2SnS_3 thin films using PLD technique (He ve ark., 2017). This resulted from this material's high evaporation pressure (Ettlinger ve ark., 2016; Schou ve ark., 2018)..

Table 4. 4. The atomic concentration of CTS thin film and with different sulfurization temperatures.

Samples	Cu (%)	Sn (%)	S (%)	Cu/Sn	S/(Cu+Sn)
F0	43.16	18.07	38.77	2,39	0,63
F450	41,36	18,13	40,51	2,28	0,68
F550	39,85	17,40	42,75	2,29	0,75
F600	42,89	16,62	40,48	2,58	0,68

At 450°C, F450 thin film presents a higher S percentage of 40.51%. The ratio of S/(Cu+Sn) rises from 0.63 to 0.68 when S vapor was incorporated into F450 thin film during the sulfurization process (Guddeti ve ark., 2018). Further increase of S concentration was observed at 550°C at F550 thin film with increase of S/(Cu+Sn) ratio to 0.75. This is closer value to the stochiometric ratio of Cu_2SnS_3 material. Elevating the temperature much higher to 600°C had the opposite effect of the sulfurization by the sublimation of S and Sn atoms inform of Sn-S vapour. As a result, we notice a decrease in the of S/(Cu+Sn) and an increase in Cu/Sn ratios to 0.68 and 2.58, respectively (Pallavolu ve ark., 2018; Avellaneda ve ark., 2022).

4.3.2.2. Structural properties (XRD) of undoped CTS thin films according to the annealing temperature

X-ray diffraction of CTS thin films with different annealing temperatures is present in Figure 4.8. The as deposited F0 thin films that was deposited at room temperature (RT) has completely amorphous structure with no visible XRD peaks at all (Vanalakar ve ark., 2015a). When the thin films were sulfurized at 400°C, crystal peak appeared in the XRD pattern confirming its polycrystalline structure.

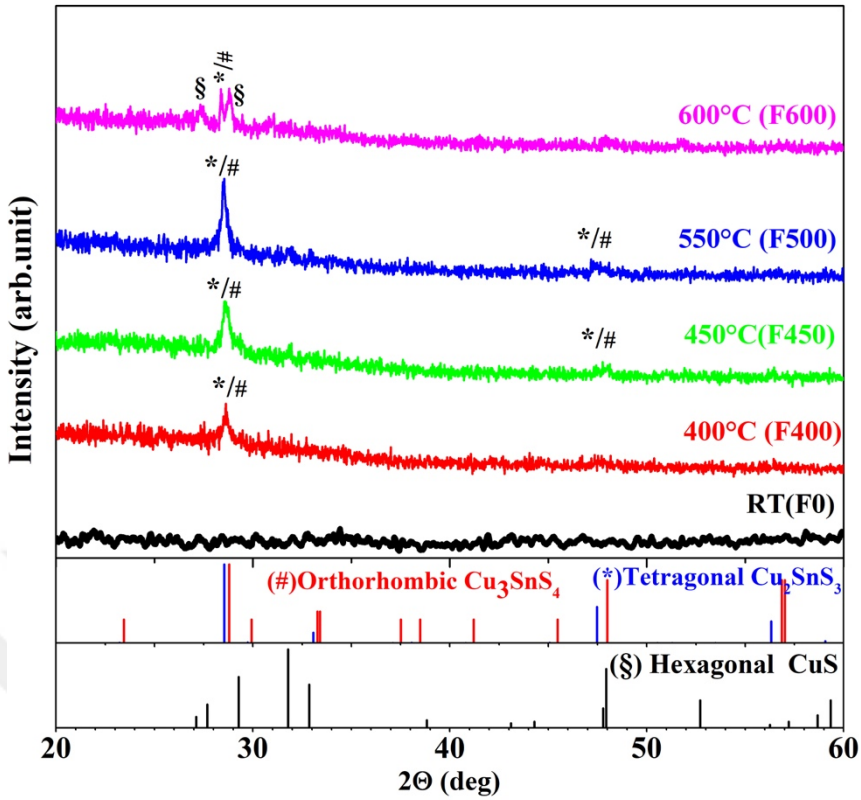

Figure 4. 8.X-ray diffraction of CTS thin films with different annealing temperatures.

In this structure, the small peak distinguish was referred to the tetragonal phase of Cu_2SnS_3 (Reference data: ICDD 01-089-4714) or the orthorhombic phase of Cu_3SnS_4 (Reference data: ICDD 00-036-0218) at 2θ= 29.4° (112)/(222). Elevating the temperature to 450°C did increase the crystallinity of the thin films from 6.9 nm to 11.2 nm. At the same time, we observed a second peak that was referred to the planes (220)/(044) of Cu_2SnS_3 tetragonal phase or Cu_3SnS_4 orthorhombic phase at 2θ= 48.2°, respectively. Further increase of the sulfurization temperature to 550°C did increased the main peak intensity causing an enhancement in the crystalline sizes from 11.2 nm to 14.75 nm. At this range of temperature, the effect of sulfurization temperature was positive and it increased the crystalline size and improved the crystallinity of CTS the thin films (Guddeti ve ark., 2018; Patel ve ark., 2018). At 600°C, new peaks were formed in XRD pattern indicating the existing of secondary phases. We observed the suppression of (220)/(044) peak and at the same time two peaks at 2θ= 27.36° and 29.8° appeared. These new peaks indicate the formation of CuS hexagonal phase (Reference data: ICDD 00-006-0464) (Pallavolu ve ark., 2018). The formation of CuS secondary phase is due to the high sulfurization temperature that triggers the evaporation of SnS (Fernandes ve ark.,

2010; Zhang ve ark., 2018). This caused a major decline in Sn and S concentration that decreased Cu/Sn and S/metal ratios to 0.68 and 2.58, respectively as presented in EDX analyse (Jiang ve ark., 2011; Guan ve ark., 2013). Due to that, the effective formation of the CuS phase in the Cu-rich F600 thin film with two peaks is a natural outcome (Ozsoy ve ark., 2021).

4.3.2.3. Morphologic properties of undoped CTS thin films according to the annealing temperature

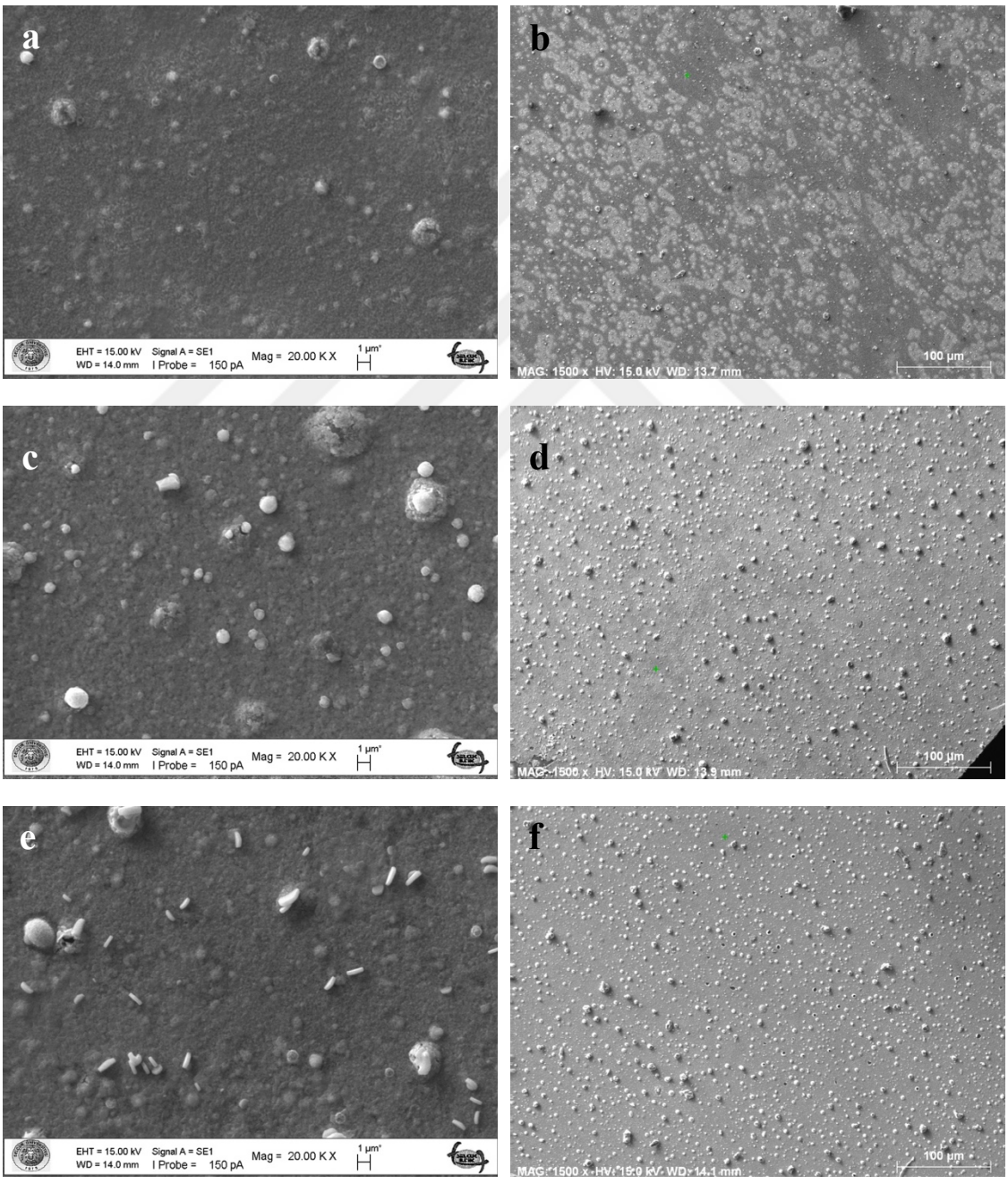

Figure 4. 9. SEM images of a1&2) F450, b1&2) F550 and c1&2)F600 CTS thin films..

It is widely known that annealing temperatures have a significant impact on the morphologies of thin films. As a result, the microstructure of CTS thin films surface was studies using SEM analyze. According to the top-view SEM images of the CTS films shown in Figure.4.9, compact and dense films have been produced at all temperatures using PLD technique with home-made CTS target. The grains are not very well distinguish in the thin films. However, we can directly notice that the grain sizes augments with temperature increasing, specifically in F550 and F600 (Figure.4.9.c & e). This might be explained by the high temperature's thermal energy that will encourage the development of the grained structure. At the same time, the crystalline size *D* (Figure.4.10) calculated from the XRD results showed a development as the sulfurization temperature augmented. On the other hand, the thickness (Figure.4.10) of the thin films increased to 529 nm in F600 thin film as the temperature rises due to the development of the amalgamation and coalescence processes (Chino ve ark., 2012; Patel ve ark., 2018; Shelke ve ark., 2020).

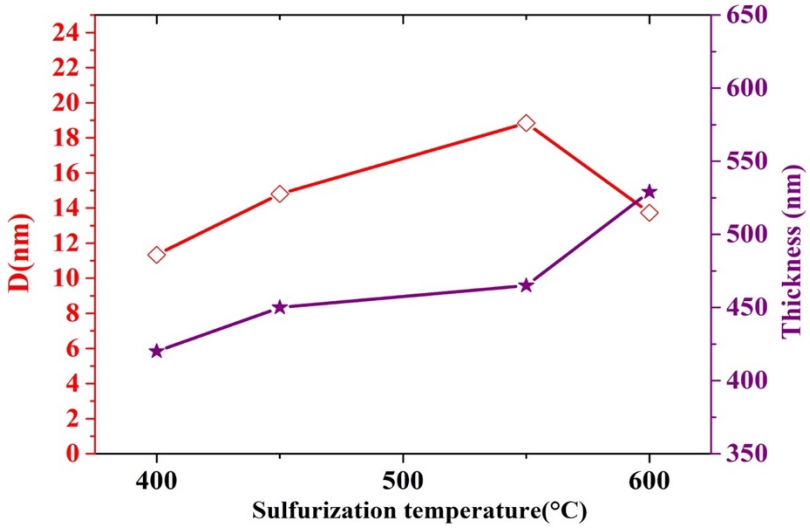

Figure 4. 10. Crystal size and thickness of CTS thin films with different annealing temperatures

It should be remarked that the surface of sample F450 in Figure.4.9.a & b has a few bright, petite clusters that are distinct from the film's general structure. The elemental composition of these particles is shown in later analyze using EDX mapping. The atomic composition of these cluster is reveled to be copper and sulfur rich which can be attributed to the formation of Cu_xS_y secondary phases (Patel ve ark., 2018). As the sulfurization temperature elevates the sizes of these particles increase and their shape change to bar-like form. Both EDX and XRD results supports these findings since we observed the CuS

peaks in the XRD pattern of F600 and the diminution of Sn concentration as the sulfurization temperature increased.

4.3.2.4. Optical properties of undoped CTS thin films according to the annealing temperature

The optical properties of thin films are very important factors that control its performance in optoelectric applications. In general, the impurities and defects as well as dopants have a significant impact on the optical characteristics. The sulfurization temperature has an important effect on the atom arrangement in thin films and the different existing defects and secondary phases. Hence, it is essential to investigate its influence on the optical properties of thin films.

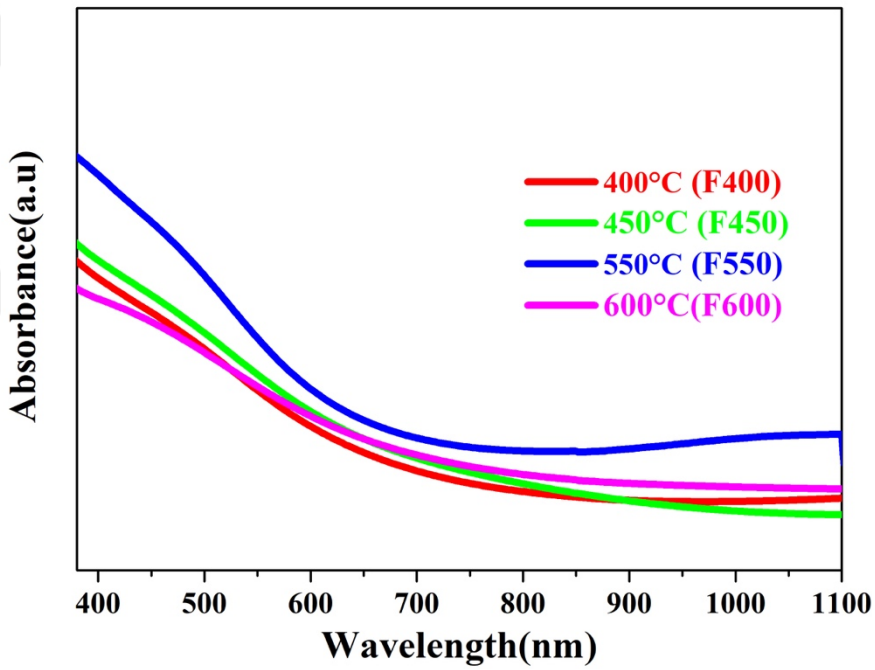

Figure 4. 11. Absorbance spectra of CTS thin films with different annealing temperatures

In Figure 4.11, we provide the absorption spectra of F400, F450, F550 and F600 thin films according to the sulfurization temperatures of 400°C, 450°C, 550°C and 600°C, respectively. We observed that the absorbance as well as the absorption coefficients (see Figure 4.12) of the thin films increased according to the sulfurization temperature with a good absorption coefficient of $\alpha > 10^4 cm^{-1}$. This increase is attributed to the enhancement of the structure of the thin films and augmentation of the grain sizes with the increase of the sulfurization temperature (Patel ve ark., 2018). When the temperature reaches 600°C, new phases are existing in the structure of the F600 which poorer the

crystallinity and decrease the absorption spectra of the thin film (Abdel-Latif ve ark., 2020).

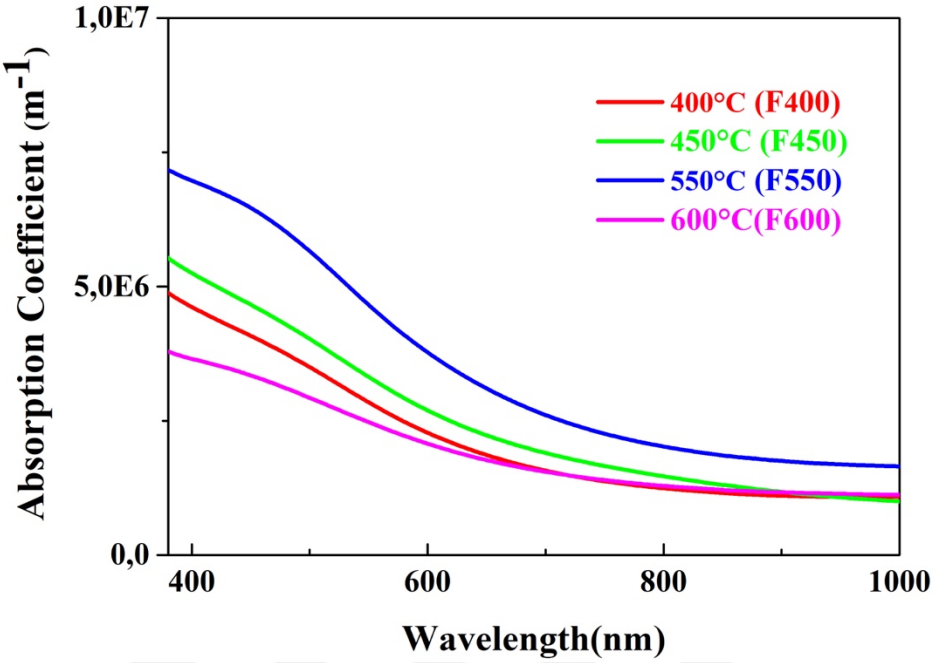

Figure 4. 12. Absorption coefficient of CTS thin films with different annealing temperatures

The band gap was determined using the $(\alpha h\upsilon)^2$ vs. hυ plot presented in Figure 4.13. The values of the band gap are ranging from 1.25 eV to 1.7 eV, which is close to previous finding of CTS band gap changing according to the sulfurization temperature (Dahman ve El Mir, 2015; Reddy ve ark., 2015). The band gap decreased from 1.64 eV to 1.25 eV when the sulfurization temperature changed from 400°C to 550°C and then it increased to 1.70 eV for F600 thin films. It was reported that the existing of CuS or Cu_xS_y secondary phases have a major effect on widening the optical band gap of Cu-Sn-S ternary thin films which is also related to the copper concentration in thin films. Thin films with low sulfurization temperature are copper rich which indicate the possible formation of CuS or Cu_xS_y secondary phases even if it was not indicated in the XRD pattern due to the low crystallinity. As the temperature increases to 550°C, the Cu concentration decreases and the incorporation of S rises. This will allow CTS material to form with a lower band gap of 1.25 eV. When the temperature of sulfurization reaches 600°C, SnS evaporation phenomena increases the Cu concentration. This will support the formation of CuS secondary phase that gives rises the band gap again to reach 1.70 eV (Guan ve ark., 2013; Ozsoy ve ark., 2021).

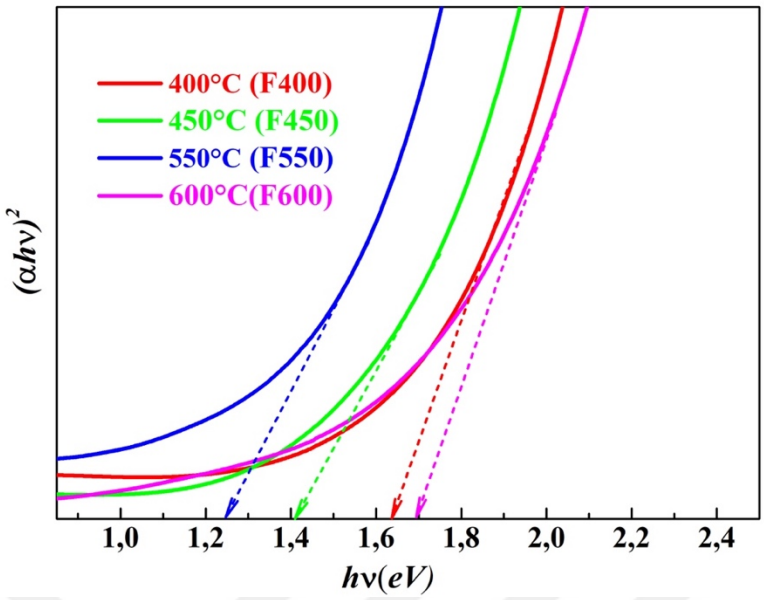

Figure 4. 13. Plot of $(\alpha h\nu)^2$ versus $h\nu$ of CTS thin films with different annealing temperatures

4.3.3. Effect of deposition time on different properties of CTS thin films

Crystallinity, surface morphology, atomic composition, and optic absorbance are dependent on the film thickness which determine possible uses of thin films. The ideal film thickness is crucial for a maximum device performance in optoelectronic device applications. Therefore, it is important to investigate how changes in film thickness affect the characteristics of CTS thin films. Additionally, controlling size and structure is a useful method for adjusting the physical and chemical properties of CTS thin films as well as their catalytic activity.

4.3.3.1. Structural properties (XRD) of undoped CTS thin films according to the deposition time

In Figure.4.14, we presented the thickness of the thin films with the crystalline size (D) calculated from the main peak of XRD pattern of F2.5, F5 and F15 thin films given in Figure.4.15. As the deposition time increases, it is very obvious that the thickness of CTS thin films rises with it. The thickness of the thin films increases from 138 nm to 623 nm as the deposition time by PLD method rises from 2.5 min to 15 min. The nucleation process intensifies and more layers of the CTS film material are deposited as the laser ablation times go on, increasing by that the film's total thickness (Suryawanshi ve ark., 2021). The fact that the rate of film thickness is nonlinear suggests that the nucleation and coalescence processes are the cause of the growth (Shelke ve ark., 2017).

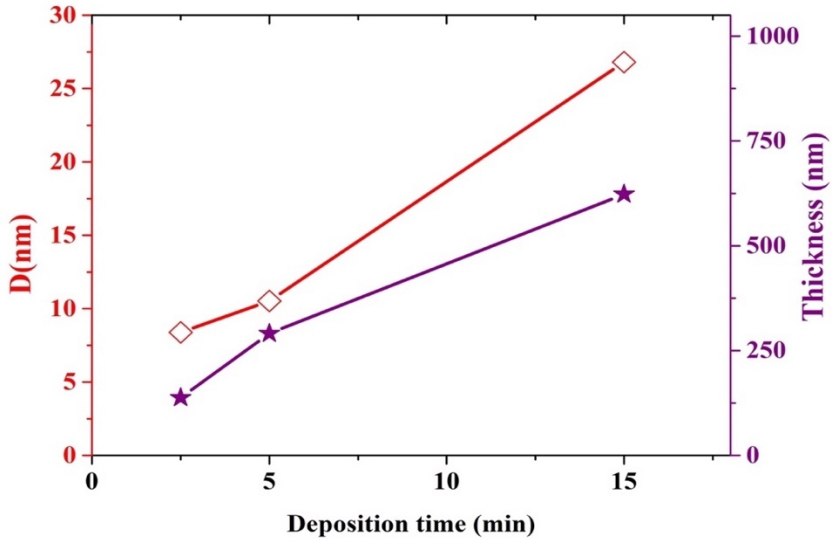

Figure 4. 14. Crystalline size and deposition rate of CTS thin films with deposition rate

XRD analyze was conducted on three thin films with different deposition times and the results are present in Figure.4.15. The thin films present relatively low crystallinity at short deposition time (F2.5) and the crystallinity enhanced when the deposition time increases (F15).

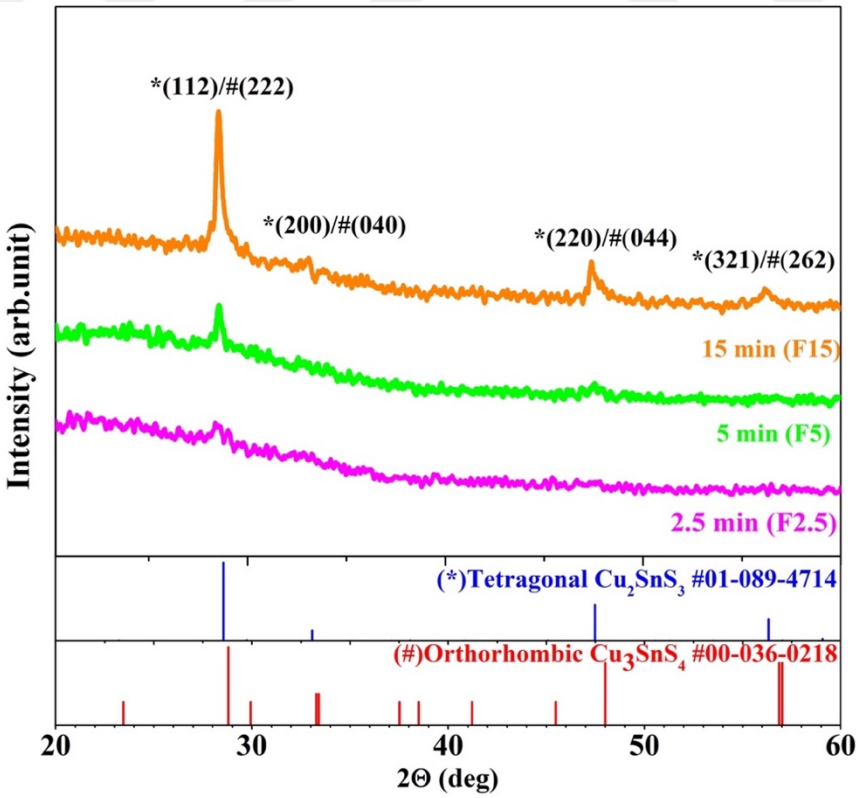

Figure 4. 15. X-ray diffraction of CTS thin films with different deposition times

The formed peaks are referred to the tetragonal Cu_2SnS_3 or orthorhombic Cu_3SnS_4 ternary structure phases as explained previously. There are no peaks that might correspond to binary secondary phase such as Cu_xS_y or SnS.

We notice the low crystallinity with minor peak in F2.5 thin films due to the small thickness of the thin film (see Table.4.5). Rising the deposition time to 5 min augments the thickness of the thin films (291 nm) and improve its crystallinity where new peak indicating (220)/(004) diffraction plane was formed. When the deposition time reached 15 min, the thickness of the thin film increased to 623 nm and two more XRD peaks appeared with augmentation of the peaks' intensity (Joshi ve Bhosale, 2019). The crystalline size also improved with the deposition time where they increased from 8.40 nm to 26.81nm (Patil ve ark., 2020).

Table 4. 5. The thickness and crystalline size of CTS thin film and with different deposition times

Abbreviation	Thickness nm	Particle size nm	Band gap eV
F2.5	138	8.40	1.44
F5	291	10.53	1.35
F15	623	26.81	1.05

4.3.3.2. Morphologic and Compositional properties of undoped CTS thin films according to the deposition time

The surface images obtained from the scanning electron microscopy (SEM) of CTS thin films obtained after sulfurization at 500°C with different thicknesses are present in Figure 4.16. Also, the EDX analyses of CTS thin film with different deposition times is present in Table.4.6. Both thin films present compact structure with no voids or pinholes despite the low thickness of F5 thin film. The increase of deposition time had a significant effect on the surface morphology of CTS thin films. As the thickness of the CTS thin film increased, more textured and larger grains are observed on the surface of F15 thin film (Jo ve ark., 2022). XRD results confirmed an crystallinity enhancement and augmentation of particle size in thick CTS thin films (Shelke ve ark., 2017), which are in accordance with the observed morphology in SEM images.

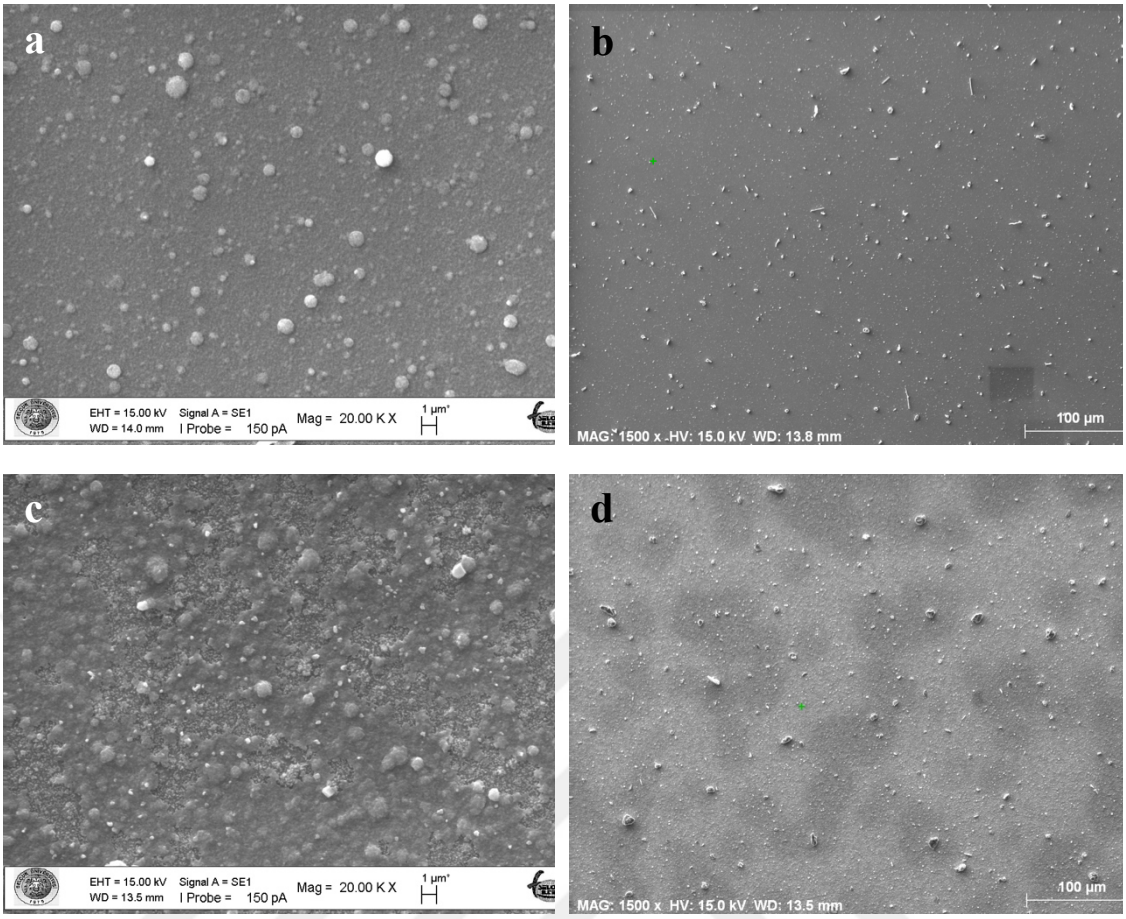

Figure 4. 16. SEM images of a & b) F5, c & d) F15 CTS thin films

F15 thin films has a cluster like surface with more roughness and bright particles (Figure 4.16. c & d), which are believed to be Cu_xS_y secondary phases (Patel ve ark., 2018).

The Cu/Sn ratio increases according to the thickness of the thin films which indicates copper rich films This explains the formation of Cu_xS_y secondary phases on the surface of F15. The S/(Cu+Sn) ratio increased in the CTS thin films as the thickness rises , which improved the incorporation of sulfur into CTS thin films (Shelke ve ark., 2017; Suryawanshi ve ark., 2021).

Table 4. 6. The atomic concentration of CTS thin film and with different deposition times

Samples	Cu (%)	Sn (%)	S (%)	Cu/Sn	S/(Cu+Sn)
F5	39,98	18,39	41,64	2,17	0,71
F15	38,21	15,14	46,66	2,52	0,87

4.3.3.3. Optical properties of undoped CTS thin films according to the deposition time

The optical absorbance of CTS thin films according to the deposition time is present in Figure.4.17. We can directly notice the effect of rising the deposition time is the increase of the absorbance due to the augmentation of the thin film's thickness (Mohamed ve ark., 2020). Thicker thin films have larger clustered grains that have more photon absorbance (Joshi ve Bhosale, 2019; Patil ve ark., 2020). F2.5 presents the lowest absorbance spectra with 138 nm thickness while F15 have the highest absorbance spectra with 623 nm thickness.

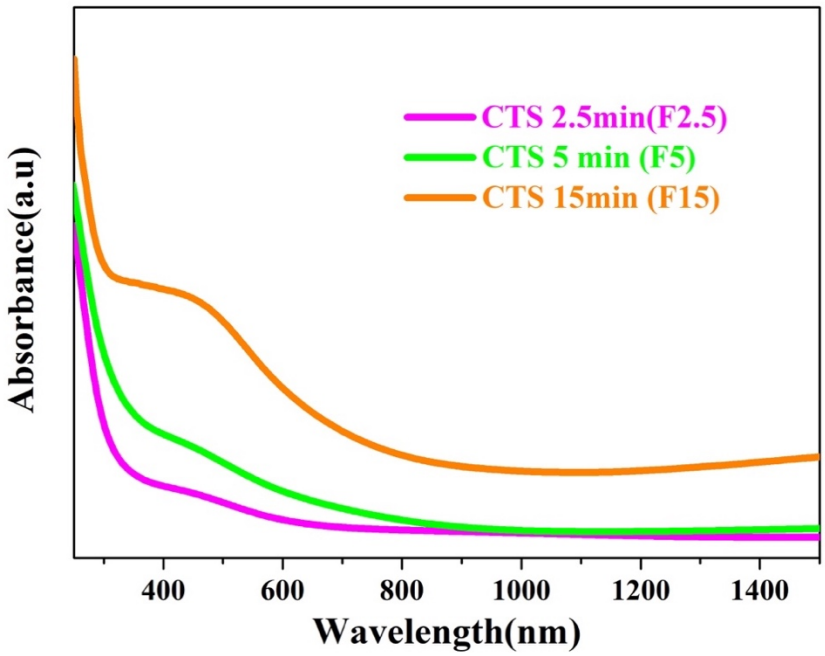

Figure 4. 17. Absorbance spectra of CTS thin films with different deposition times

The graph of $(\alpha hv)^2$ versus hv of of CTS thin films with different deposition times is present in Figure 4.18. It was found that as deposition time was increased, the energy band gap of CTS films diclined due to a rise in absorbance according to the growth in film thickness. The fact that the band gap varied from 1.44 eV to 1.05 eV in response to the change in deposition time. It was suggested that altering the ablation duration in PLD technique can change the material's optical band gap (Joshi ve Bhosale, 2019; 2021).

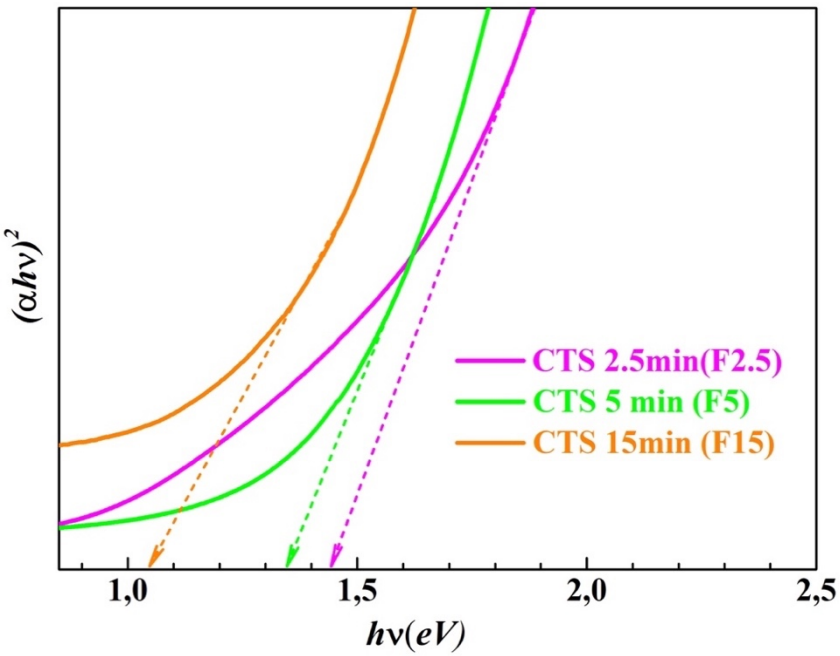

Figure 4. 18. Plot of $(\alpha h\nu)^2$ versus $h\nu$ of F2.5, F5 and F15 CTS thin films

4.4. Na and Li Doped CTS Thin Films and Solar Cells Properties

In order to achieve our goal and investigate the effect of alkali atoms doping on CTS solar cells we will present in this section the results in I-V characteristics of two solar cells sets. The first set of solar cells is made by CTS thin films with different doping concentrations of Li atoms while the second one is made using Na as a dopant atom with the same concentrations. We will first explain the steps followed in order to construct these solar cells and then present the I-V results under darkness and illumination conditions.

4.4.1. Experimental Process of Na and Li doped CTS thin films and solar cells

4.4.1.1. Preparation of Na and Li doped thin films

The growth process of Na and Li doped CTS thin films is the same as we illustrate in section 4.3.1. However, annealing temperature and deposition time are fixed at 500°C and 10 min as presented in Table 4.7

Table 4. 7. List of Na and Li doped CTS thin films with the preparation parameters

Used target	Deposition time	Annealing temperature	Abbreviation
TLi1	10 min	500°C	FLi1
TLi3	10 min	500°C	FLi3
TLi5	10 min	500°C	FLi5
TNa1	10 min	500°C	FNa1
TNa3	10 min	500°C	FNa3
TNa5	10 min	500°C	FNa5

4.4.1.2. Preparation of Al/n-Si/CTS/Ag structure solar cells

The Si wafers are a very important element in the PV industry due to its incredible properties. To assure the best effectiveness from these wafers we have to delicacy clean them and preserve them in vacuum atmosphere to prevent any kind of contamination or oxidation. The wafers in our work were first cut using fs laser to make uniform slices of 1 cm^2 surface for each. Afterwards, the wafers were washed with detergent and then rinsed with distillated water. The next step is to remove the naturally formed oxide layer (SiO_2); the slices of Si wafers were all immersed in dilated hydro-fluoride (HF) solution (1:24) for 2 min. The wafers were then again with distillated water and dried out using N_2 gas flow.

The Si used in our experiment are of 500 µm thickness and 10 Ω.cm resistance n type and one polished surface of (100) orientation.

The Al back contact was deposited on the non-polished face of the clean and dry n-Si slides using evaporation technique (PVD). The Ag or Al flacks were placed on a pot in an evacuated chamber of a pressure of 10^{-6} mbar. The deposition rate was changing from 1 to 5 Å/s. The final thickness of the contact is about 100 nm.

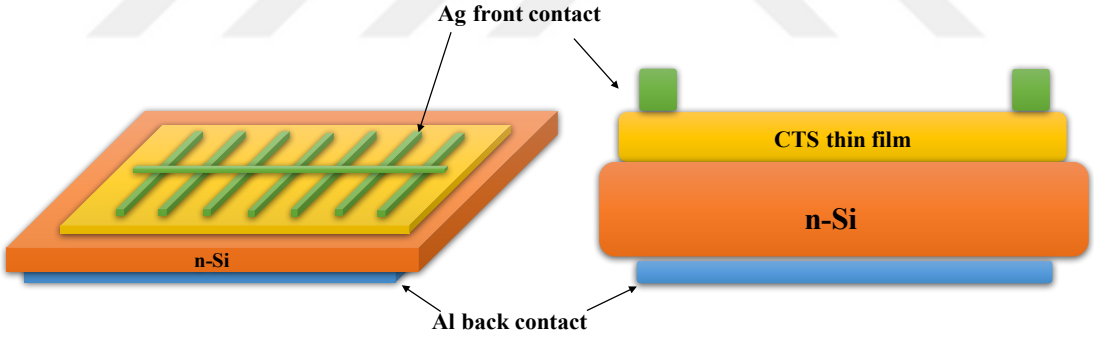

Figure 4. 19. Structure of CTS solar cells

After the back Al contacts were set, we deposited CTS different films with PLD technique followed by annealing process (see section 4.3.1). The Ag front contacts were also made using PVD with the same deposition technique. Before the deposition of the front contact, grid mask was paced on CTS thin films with a 0.2 cm^2 spacing (active surface). A schematic image presenting the structure of our solar cells is present in Figure 4.19. The used abbreviation in this section is present in Table 4.8.

Table 4. 8. List of the prepared CTS based solar with the corresponding abbreviations

Solar cells/diode structure	Abbreviation
Al/n-Si/FP/Ag	SP
Al/n-Si/FNa1/Ag	SLi1
Al/n-Si/FNa3/Ag	SLi3
Al/n-Si/FNa5/Ag	SLi5
Al/n-Si/FLi1/Ag	SNa1
Al/n-Si/FLi3/Ag	SNa3
Al/n-Si/FLi5/Ag	SNa5

4.4.2. Na Doping effect on CTS thin films

Doping the CTS material with different atoms such as Ge, Ag and Sb (Umehara ve ark., 2013; Zhao ve ark., 2020; Magdy ve ark., 2021) has proven to change and enhance the properties of this material. As for the solar cells efficiency improvement, Na atom is the most investigated one for Chalcogenide materials such as CIGS, CZTS and CTS (Nakashima ve ark., 2015a; Chantana ve ark., 2017a; Chantana ve ark., 2017b; Sasagawa ve ark., 2018). In this section we will present the effect of Na doping on the properties of CTS thin films.

4.4.2.1. Na doped CTS Thin films structural properties (XRD)

We present in Figure 4.20 XRD pattern of Na doped CTS thin films with different concentrations of Na atom. All Na doped CTS thin films displayed well defined XRD peaks with the same preferred orientation at $2\theta = 28.9°$. Despite the doping concentration of Na atoms, the structure of these thin films is considered to be polycrystalline mix phases of tetragonal and orthorhombic of Cu_2SnS_3 and Cu_3SnS_4 ternary materials, respectively.

Additionally, no secondary phases or impurities with Na atoms have been detected. As a result, it is assumed that the secondary phases of $Na_xCu_2SnS_3$ have unimportant amount or low crystallinity to be identified by XRD. The influence of Na doping is primarily seen once Na concentration exceed 1% (FNa1). This doping range it causes the main peak's intensity to progressively decline as Na concentration rises to 5% (FNa5).

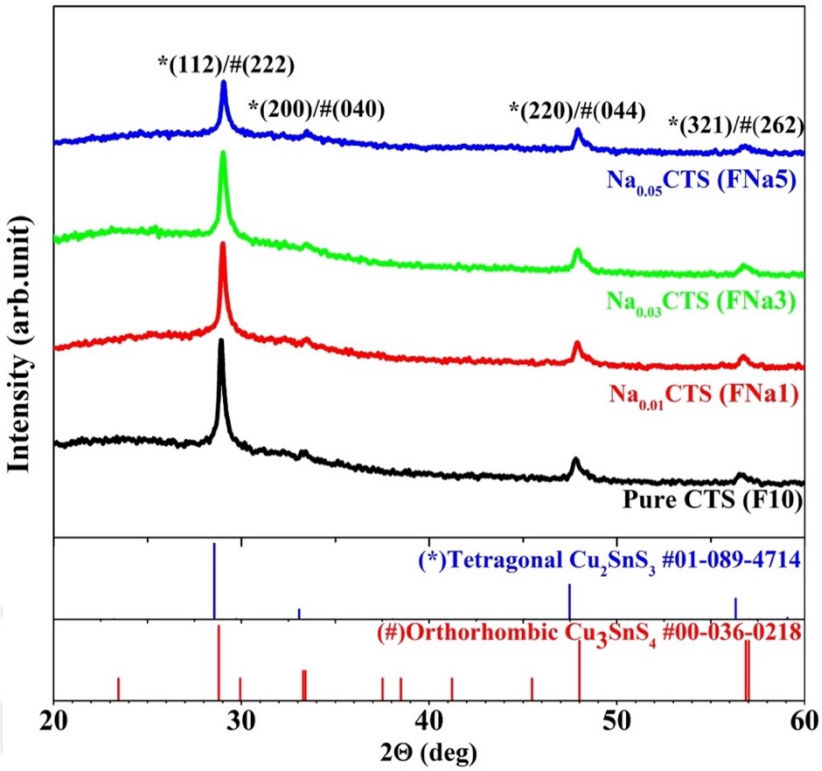

Figure 4. 20. X-ray diffraction of CTS thin films with different Na doping concentrations

From Figure 4.21.a, it is very obvious that the crystalline size D rises from 25.3 nm for FP to 28.9 nm for FNa1. The deposition rate didn't change much with Na doping and the thickness of the thin films witnessed a small increasing. In FNa1 thin films, the increase in crystalline size at this value of doping might be caused by the advantageous effects of adding Na atoms to the CTS structure, as mentioned in prior publications (Abdel-Latif ve ark., 2021). With additional Na atom incorporation, the peak intensities have been reduced as well as the crystal sizes of FNa3 and FNa5 to 22.4 nm and 21.4 nm, respectively. The disorder in CTSN3 and CTSN5 caused by the elevated Na content is most likely the main reason for the film's decreased crystalline quality (Wen ve ark., 2015; Wubet ve Kuo, 2015; Marzougi ve ark., 2019).

In Figure 4.21.b, we provided the dislocation density and strain of FP, FNa1, FNa3 and FNa5 thin films. It can see that the both plots demonstrate the same outlook. The lowest values of δ and ε was found at in FNa1. As a result, FNa1 demonstrate the best crystallinity. In FNa1 thin films, dislocation density and strain are at their lowest levels. As a result, among all thin films, CTSN1 has the best crystallinity.

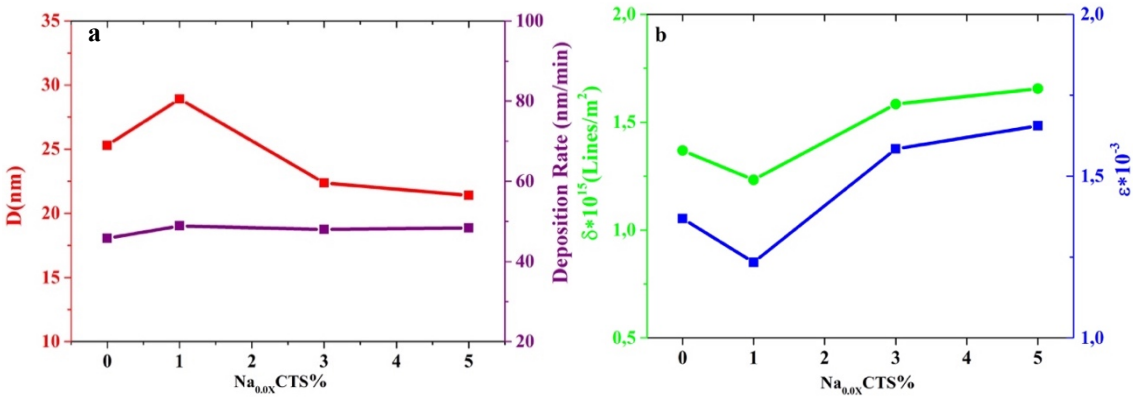

Figure 4. 21. a) Crystal size and deposition rate and b) density of dislocations and microstrain of CTS thin films with different Na doping concentrations

Since XRD analysis is not enough to discriminate the existing phases in CTS thin films due to the similar lattice parameters, further investigation of the thin films structure is done using Raman spectroscopy.

4.4.2.2. Na doped CTS Thin films compositional properties

The predicted atoms (Cu, Sn, S and Na) are present in almost stoichiometric quantities in both targets, TP and TNa1. The ratio of sulfur to metal in the FP thin film has increased from 0.63 to 0.8 during the sulfurization process at 500°C (see Table 4.4 and Table 4.9) signifying a successful sulfurization procedure. Therefore, we believe that we were able to partially offset the loss of S that occurred during the PLD technique's deposition.

Table 4.9. The atomic concentration of Na doped CTS thin film and target

Samples	Cu (%)	Sn (%)	S (%)	Na (%)	Cu/Sn	S/Metal
TP	34.08	17.70	48.22	0	1.93	0.93
FP	38.95	16.52	44.52	0	2.36	0.80
TNa1	33.3	18	47.85	0.85	1.85	0.93
FNa1	35.61	16.36	47.29	0.74	2.18	0.91

When compared to FP thin films, the S/Metal ratio in FNa1 thin films is higher. Additionally, when compared to pure CTS thin films, the Cu/Sn ratio decreased from 2.36 to 2.18 while the Sn concentration in both thin films remained the same. As a result, it can be assumed that Na doping improves the integration of S and Sn atoms by inhibiting the re-evaporation of Sn-S during the sulfurization treatment (Chantana ve ark., 2017a). As a conclusion, FNa1 thin films exhibit improved composition for upcoming PV application.

4.4.2.3. Na doped CTS Thin films RAMAN analyses

The Raman plot of Figure 4.22 has exhibited two Raman analyse results of FP and FNa1 thin films. FP thin film presented three different Raman peaks that can be referred to tow different Cu-Sn-S ternary alloys. The first and second peaks at wavenumbers of 295 cm^{-1}, 331 cm^{-1} can be assigned to Raman spectra of tetragonal (I-42m) phase of Cu_2SnS_3 (Wang ve ark., 2016; Chaudhari ve Joshi, 2018; Joshi ve Bhosale, 2019). As for the last one at 348 cm^{-1} wavenumber, it belongs to Raman spectra of orthorhombic (Pmn21) Cu_3SnS_4 phase (Fernandes ve ark., 2010).

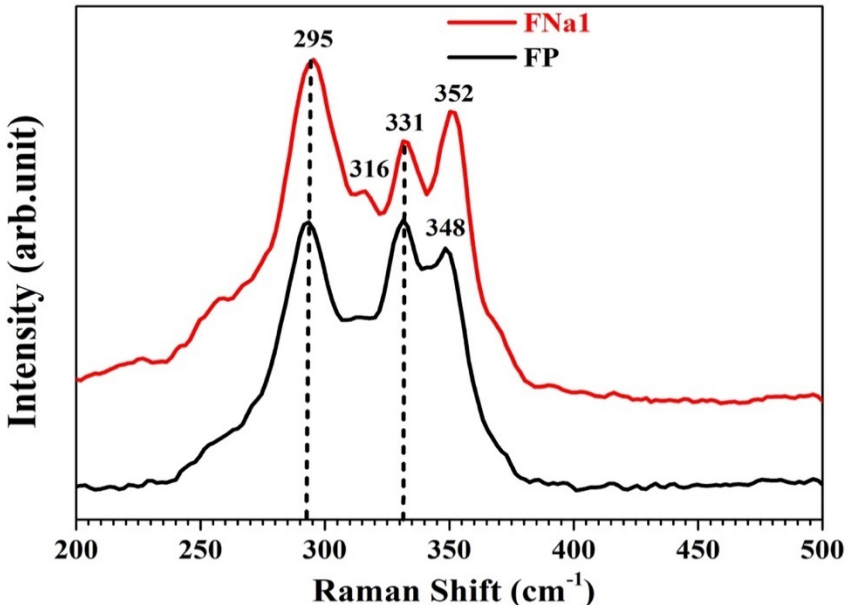

Figure 4. 22. Raman plot of FP and FNa1

These results are in a good accordance with the ones reviled in XRD analyse where two phases (Cu_2SnS_3 and Cu_3SnS_4) were detected. The existence of Cu_3SnS_4 is due to the copper rich composition of FP thin films as revealed in EDX analyses (Cu/Sn = 2.36). FNa1 thin film also presents three well defined peaks at 295 cm^{-1}, 331 cm^{-1} and 352 cm^{-1}. The first two peaks are situated at the same wavenumber as FP thin films. However, the third one at 352 cm^{-1} can be referred to the tetragonal phase of Cu_2SnS_3 Raman spectra. Furthermore, a shoulder like peak at 316 cm^{-1} appeared at FNa1 Raman spectra. This peaks stated in some previous publication as an evidence of a potential existence of Na_xCuSnS_3 secondary phase and/or $Cu_2Sn_3S_7$ phase (Chantana ve ark., 2017b; Tanaka ve ark., 2020).

4.4.2.4. Na doped CTS Thin films morphologic properties

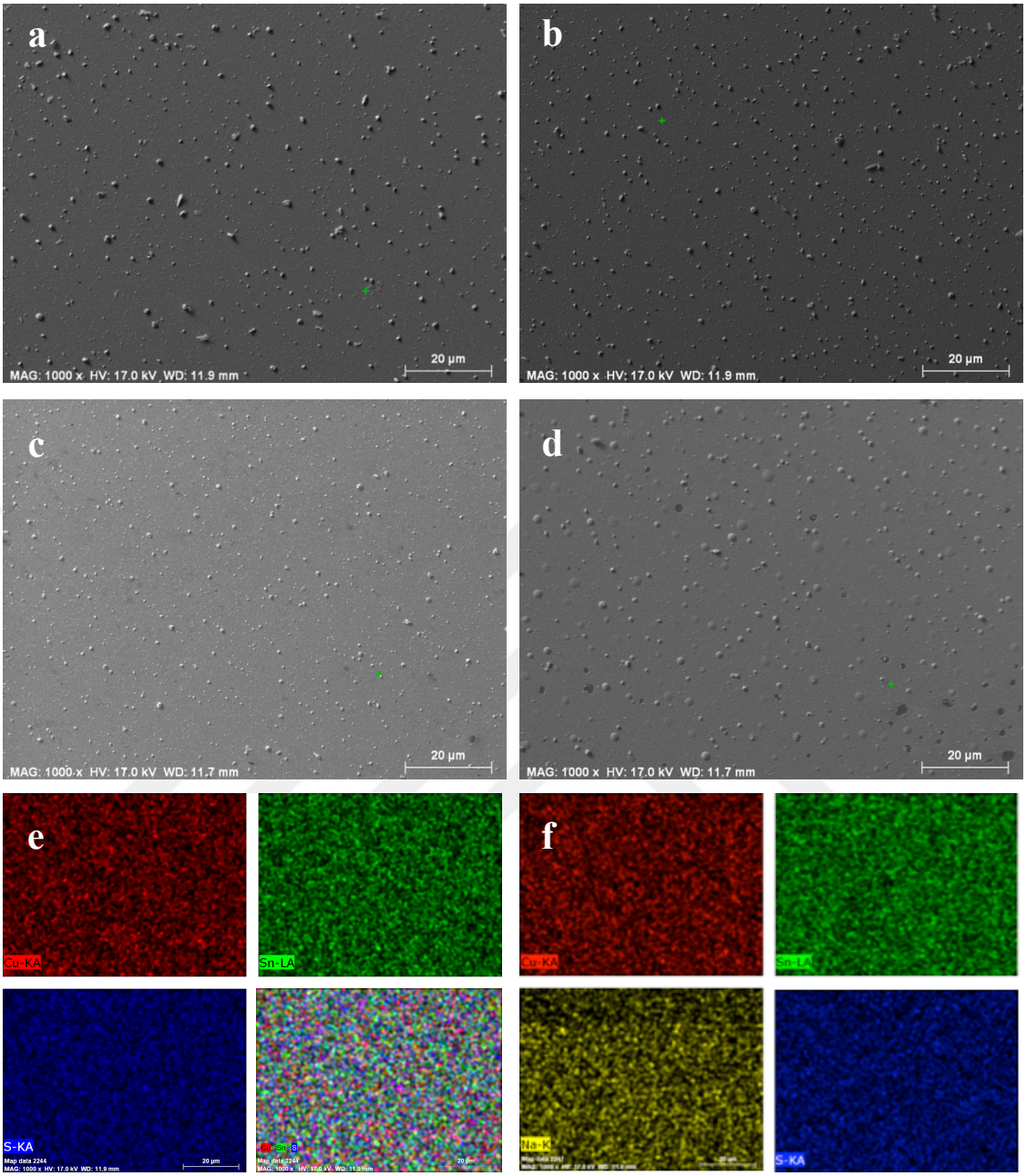

Figure 4. 23. SEM images of a) FP, b) FNa1, c) FNa3 and d) FNa5 thin films in addition of EDX mapping images of e) FP and f) FNa1

In Figure 4.23.a & b, SEM images of FP and FNa1 thin films are presented. The surface of both thin films presents similar features with compact structure and no visible cracks and small dispersed particle with various sizes and shapes. Any different between the two thin films surfaces is fairly noticeable, except that FNa1 presents more particles with relatively smaller sizes. The sizes of these particle continue to decreased in FNa3 (Figure 4.23.c). In FNa5 thin films (Figure 4.23.d), the thin films growth starts to failure and we

observed that some parts of the surface have been removed from the thin films. This indicates that the crystallinity of FNa5 is the lowest just as reported in the XRD analyses.

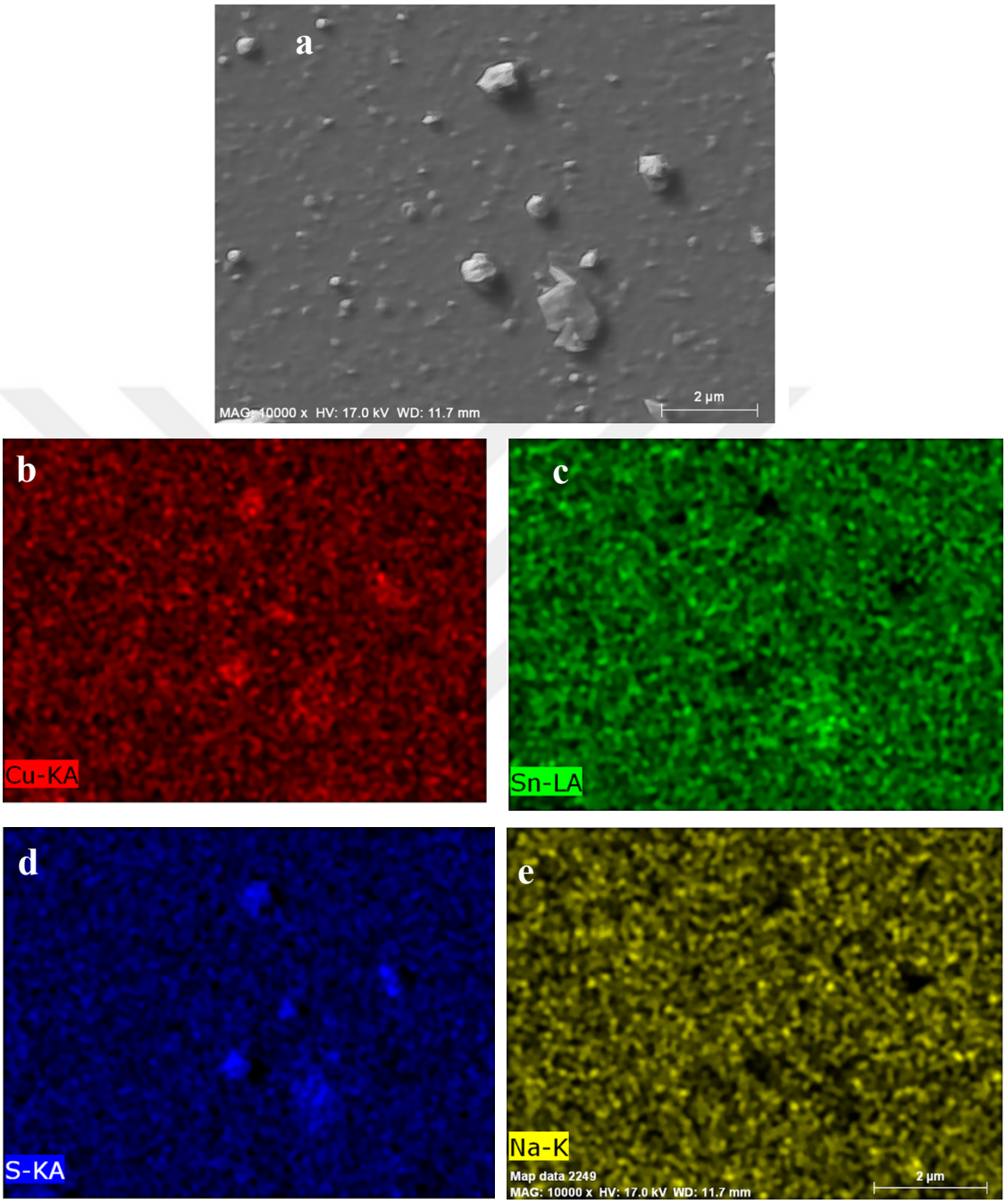

Figure 4. 24. a) SEM and b) EDX mapping images of FNa1 thin film in relatively small area (2µm scale)

The distribution of atoms on the surface of the thin film wax examined using elemental mapping. In Figure 4.23.e & f, the EDX mapping of both films presents uniform dispersion over all the surface of the composing elements; copper, tin, sulfur and sodium.

At a 2µm scale area, we repeated the same investigation of FNa1 thin film and the results are present in Figure 4.24. The different colors that indicate each element (red, green, blue and yellow for Cu, Sn, S and Na, respectively) showed brighter spots in Figure 4.24.b & d and darker ones in Figure 4.24.c & e. These spots match with the small particles dispersed on the surface of the thin films, which means that these particles are Cu and S rich but Sn and Na poor. These observations are explained by the formation of Cu_xS_y secondary phases on top of the thin films even though it wasn't detected by Raman or XRD analyses. These observation was states in previous works on Cu_2ZnSnS_4 (Kermadi ve ark., 2018) and Cu_2SnS_3 (Heidariramsheh ve ark., 2021).

4.4.2.5. Na doped CTS Thin films optical properties

The variation of the absorption spectra according to the wavelength of Na doped CTS thin films is present in Figure 4.25. The absorption of FNa1 thin film increased in the visible range compare to FP. Increasing the doping concentration of Na into CTS thin films is FNa3 and FNa5 thin films decreased the absorption of the thin films. Because introducing Na atoms to the targets before the deposition with PLD system didn't affect the deposition rate and the thickness (see Table 4.8.) of the thin films, it might be attributed the tuning of the absorption edge to a change in crystallinity of the thin films.

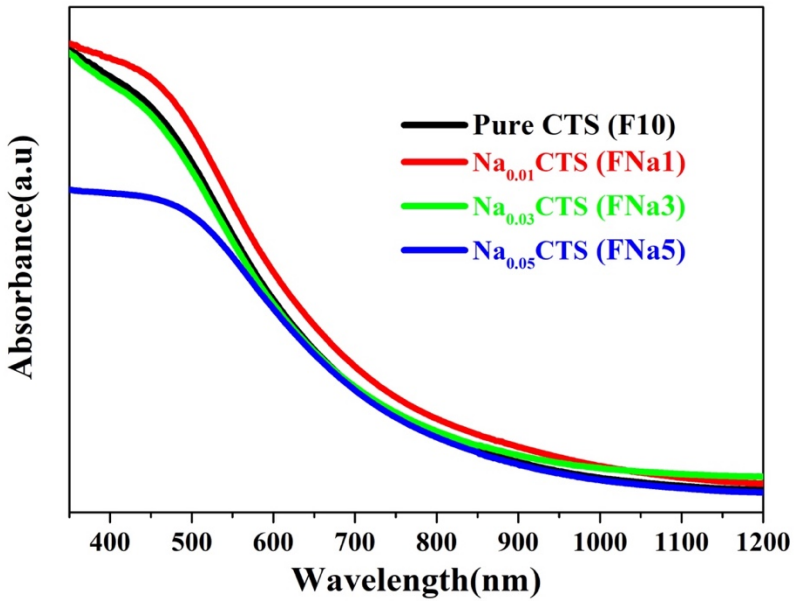

Figure 4. 25. Absorbance spectra of FP, FNa1, FNa3 and FNa5 thin films

With enhanced crystal size and least grain boundaries that serve as scattering centers, FNa1 thin film showed improved optical absorption compare to FP. In FNa3 and FNa5

thin films, the crystallinity on the thin films decreased, this will automatically increase the grain boundaries and reduces the absorption of thin films (Guo ve ark., 2021; Hosseinpour ve ark., 2021). The band gap values present at Table 4.10. and Figure 4.26 have relatively close values to the band gap of FP thin film and also in accordance with the existing values of CTS tetragonal phase (Vanalakar ve ark., 2015a; Kim ve ark., 2016a). With the highest absorption and largest crystal size, FNa1 has the narrowest band gap (Hosseinpour ve ark., 2021).

Table 4. 10. The band gap energies, thicknesses and crystalline sizes FP, FNa1, FNa3 and FNa5 thin films

Samples	Eg (eV)	Thickness (nm)	Crystalline size D (nm)
FP	1.11	458	25.3
FNa1	1.08	489	28.9
FNa3	1.12	480	22.4
FNa5	1.15	458	21.4

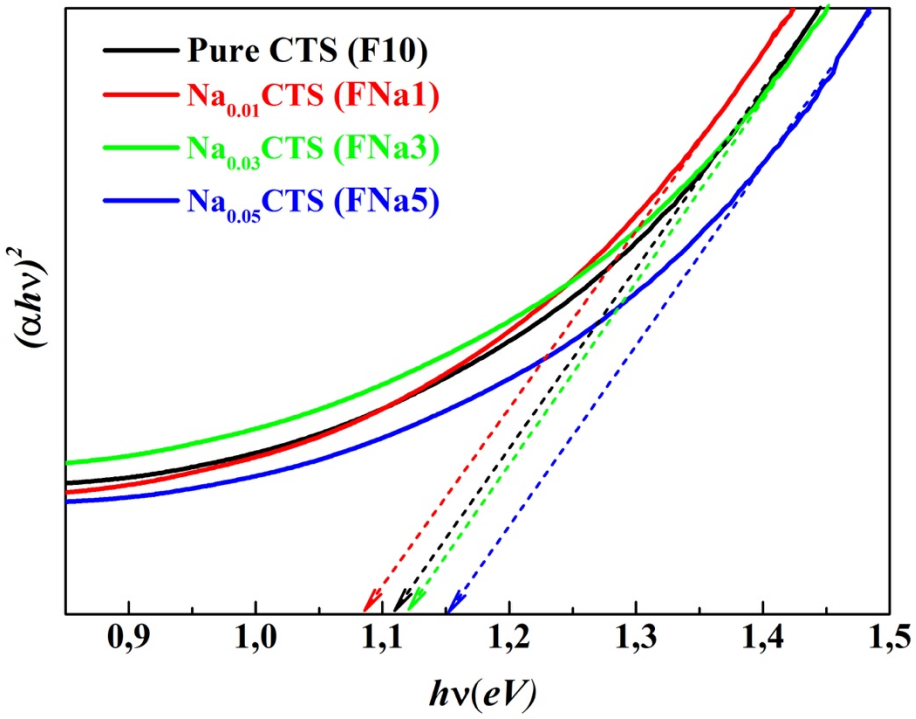

Figure 4. 26. Plot of $(\alpha h\nu)^2$ versus $h\nu$ of FP, FNa1, FNa3 and FNa5 thin films

4.4.3. Effect of Na doping on the characteristics of SNa1, SNa3 and SNa5

4.4.3.1. Properties of Al/Si/CTS/Ag diodes for Na doped and non-doped Cu_2SnS_3 (darkness)

Prior to the presentation of doped and non-doped Cu_2SnS_3 thin films based solar cells we will present the electric properties of the different prepared diodes form the measured I-

V characteristics in darkness. The electric properties that will be extracted are the reversed saturation current I_s , the ideality factor m and the rectification rate R. Theoretically, the current of diode follows the thermionic emission theory or equivalent circuit equation of diodes (Yang ve ark., 2008; Gezgin ve ark., 2020) present in Eq 4.3:

$$I = I_s\,[exp(qV/mKT) - 1] \qquad \textbf{Eq 4. 3}$$

Where I_s is the revers saturation current, q is the electric charge $T$is the temperature in kelvin (Absolut), K is the constant of Boltzman and m is the ideality factor.

The ideality factor can be determined using the Eq 4.4 where I represent the forward bias. In the logarithmic graph I-V, we can calculate m by drawing a straight line in the forward bias of the logarithmic zone.

$$m = \frac{q}{KT}\frac{dV}{d\ln(\mathrm{I})} \qquad \textbf{Eq 4. 4}$$

The rectification rate R is the ratio between I_+/I_- where I_+ and I_- are the values of the forward and reversed current at +1V and -1V, respectively.

The reverse saturation current I_s is related to the recombination mechanism existing in the semiconductor materials. This parameters in related to the intrinsic properties existing in the materials (Werner ve Zdanowicz, 2007; Ferhati ve Djeffal, 2018).

W represent the thickness of thin film.

The ideality factor or quality factor is a constant value specific for each solar cell that signify the quality of the heterojunction, for an ideal junction $m = 1$. If $1 < m < 2$, it indicates that the recombination current is less dominant than the diffusion current in the solar cell. If $2 < m$, it denotes that the dominant current in the transport mechanism is the recombination current (Ismail ve ark., 2019a; Ojeda-Durán ve ark., 2020).

These parameters were calculated from the I-V characteristics (see Figure 4.27 and presented in Table 4.11.

A very obvious rectification behaviour is seen in the four diodes specially in SNa1 that have the best rectification ratio among all the other diodes. The rectification ratios of SP, SNa1, SNa3 and SNa5 are 8.13, 297.44, 90.51 and 15.99, respectively. The reverse saturation currents of CTS solar cells SP, SNa1, SNa3 and SNa5 are 8.89, 6.03, 9.4 and 10.94 10^{-6} A/cm^2, respectively. After doping with Na atom at SNa1 solar cells, an encasement was noticed of the junction quality that can reflected on the diode properties by reducing m and I_s to its lowest values (m = 1.65, I_s = 6.03*10^{-3} mA/cm^2).

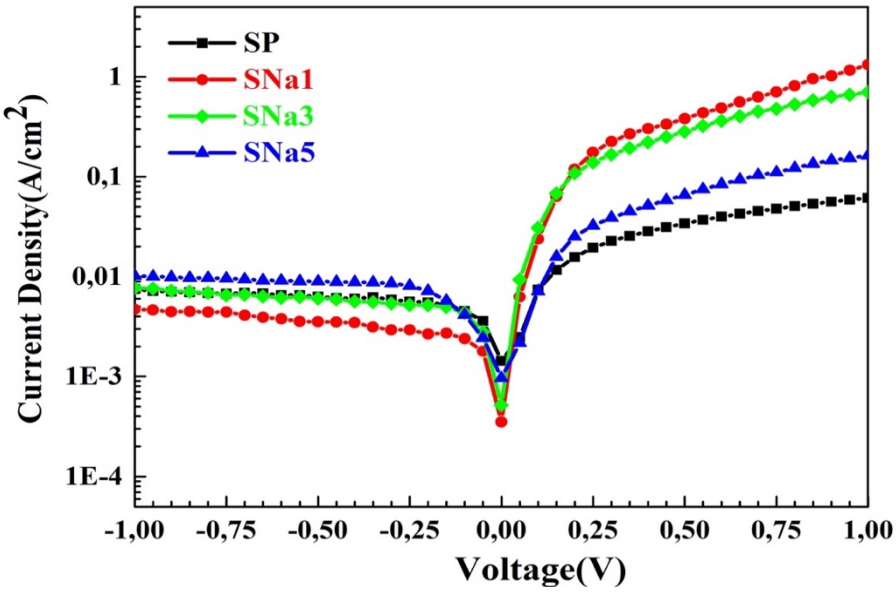

Figure 4. 27. I-V logarithmic plot of SP, SNa1, SNa3 and SNa5 in darkness

However, excess doping of Na in SNa3 and SNa5 diodes increased the ideality factor and saturation current signifying that more recombination events took place in the heterojunction diodes (Zaki ve ark., 2020). The reduction of the grain sizes and the low crystallinity in FNa3 and FNa5 thin films affected negatively on the quality thin films. It will augment the defect concentration while the charge carriers' free path will decrease. And as a result, the value of m and I_s increased scientifically (Yun ve ark., 2007; Kumar ve ark., 2013; Ismail ve ark., 2019b).

Table 4. 11. Electric properties of SP, SNa1, SNa3 and SNa5 solar cells in darkness

Abbreviation of solar cell	R_R	m	J_0*10^{-3} mA/cm^2
SP	8.13	2.41	8.89
SNa1	297.44	1.68	6.03
SNa3	90.51	1.95	9.4
SNa5	15.99	1.91	10.94

4.4.3.2. PV properties of SNa1, SNa3 and SNa5 solar cells (illumination)

The I-V graph of SP, SNa1, SNa3 and SNa5 solar cells under illumination with the values of solar cells parameters are present in Figure 4.28 and Table 4.12, respectively. We saw that adding Na atoms to CTS thin films (FNa1) improves their crystallinity and reduces their grain boundaries, which in turn lowers the number of non-radiative recombination centers (Sheng ve ark., 2013). Therefore, there was an improving of the I_{sc} value from 7.72 mA/cm^2 in SP to 9.89 mA/cm^2 in SNa1.

In numerous studies that investigated chalcogenides semiconductors (CIGS and CZTS), it has been observe that doping with Na atoms neutralizes the intrinsic donor defects at the grain boundaries (Kronik ve ark., 1998; Wei ve ark., 1999; Azulay ve ark., 2016; Chantana ve ark., 2017a) and/or generates new acceptor defects (Schroeder ve Rockett, 1997; Sun ve ark., 2009; Xiao ve ark., 2015). Therefore, it has been claimed that Na incorporation in Cu_2SnS_3 thin films can passivate the Sn_{Cu} donor defects and also the defects relate to oxygen. This can raise the p-type conductivity and boost the hole concentration (Kanai ve Sugiyama, 2021).

Table 4. 12. Optoelectric properties of SP, SNa1, SNa3 and SNa5 solar cells under illumination

Abbreviation of solar cell	V_{oc}(mV)	I_{sc} (mA/cm^2)	FF (%)	η (%)
SP	240	7.72	19.4	0.45
SNa1	290	9.89	28.67	1.03
SNa3	220	5.27	32.06	0.46
SNa5	180	3.89	19.46	0.17

On the other hand, when the number of non-radiative recombination sites reduces, the lifetime of charge carriers increases, improving in general the J-V parameters of the solar cell.

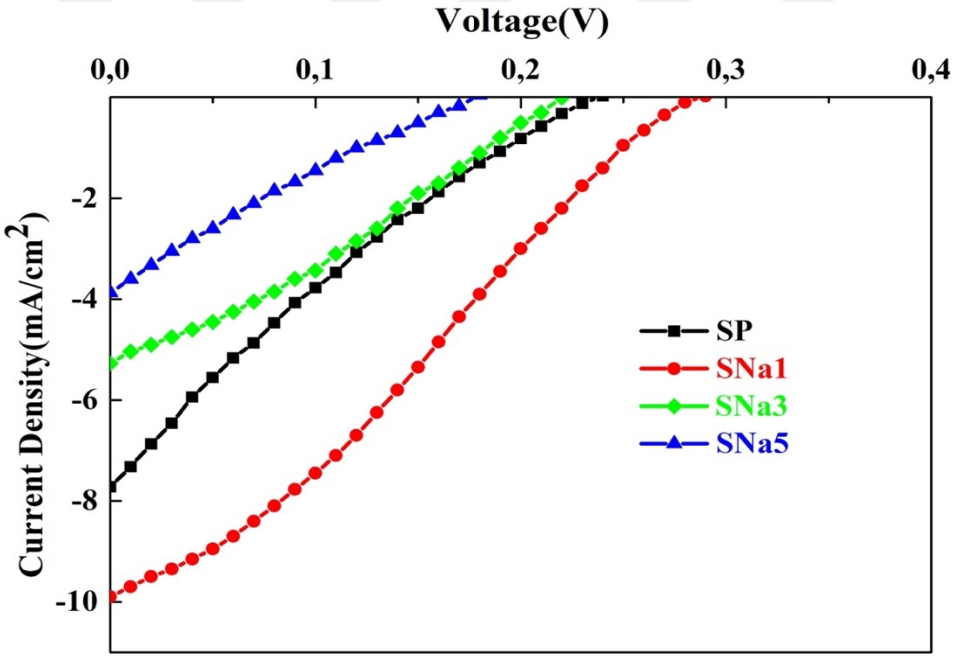

Figure 4. 28. I-V logarithmic plot of SP, SNa1, SNa3 and SNa5 solar cells under 1.5GAM illumination

In SNa1 solar cells, V_{oc} and FF values are raised from 240 mV to 290 mV and from 19.4% to 28.67%, respectively. Additionally, short circuit current I_{sc} increased its values from

7.72 mA/cm^2 to 9.89 mA/cm^2. The ideality factor m and the saturation current I_s are also at their lowest values for SNa1 solar cells, which point to excellent diode quality and less charge carrier recombination. And as a result, we saw an increase in the η from 0.45% to 1.03%. In Figure 4.29, the boxplot presents the result of different I-V measurements done on SP, SNa1, SNa3 and SNa5 solar cells. At higher doping concertation of Na (SNa3 and SNa5), we can clearly see the decline in the performance of the solar cell along with the reduction of the crystalline size and the absorption in FNa3 and FNa5. There was a decrease of the V_{oc} and I_{sc} to 0.22 V & 0.18 V and 5.27 mA/cm^2 and 3.89 mA/cm^2, respectively. The decline in the quality of the films in general causes the reduction of η to a very low value of 0.17% for SNa5 (Shin ve ark., 2011).

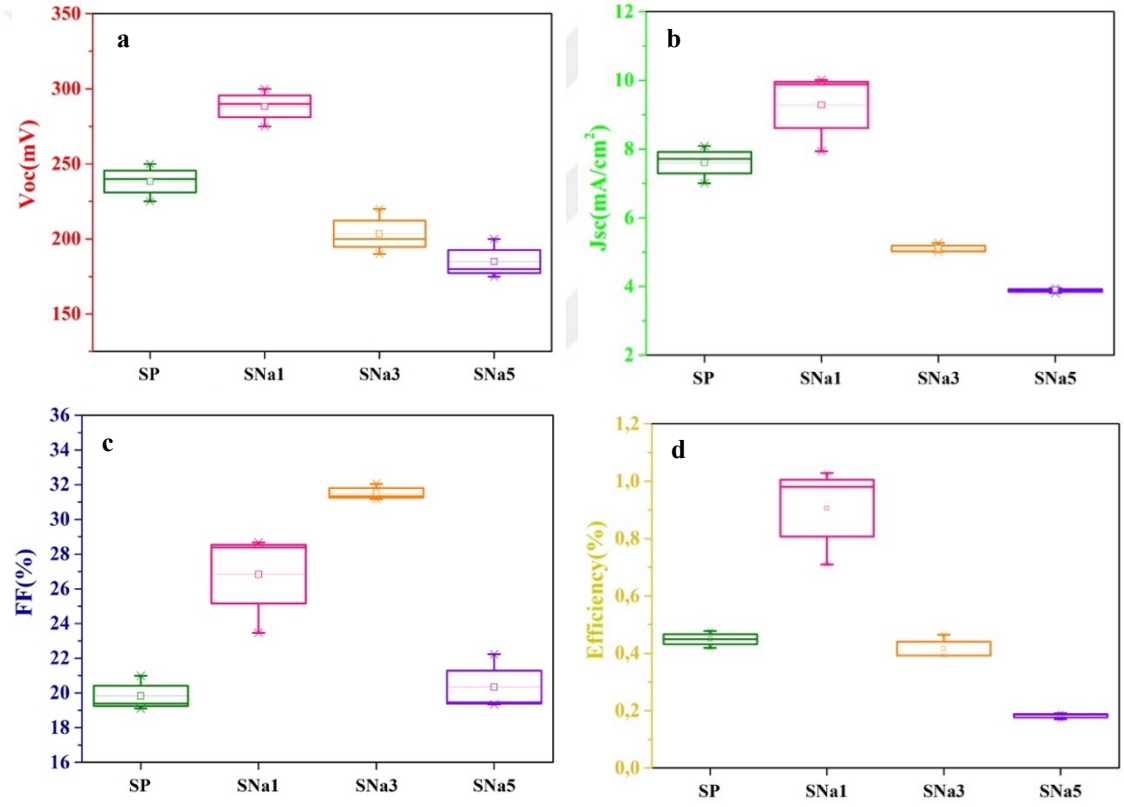

Figure 4. 29. Boxplot of SP, SNa1, SNa3 and SNa5 solar cells parameters

To further understand this decrease we refer to the work done by Kanai *et al.*(Kanai ve Sugiyama, 2021). It was claimed in this work (Kanai ve Sugiyama, 2021) that excess incorporation of N atom might be lead to additional production of Na-S-O based phases. These materials Na-S-O negatively affect the growth of CTS thin films and decline the performance of the solar cell. Another study done by Chantana *et al.*(Chantana ve ark., 2017a; Chantana ve ark., 2017b), indicated that CTS-based solar cells values have been

decreased as a result of further Na doping. They linked this deterioration to the development of the secondary phases Na_xCuSnS_3, Sn_3S_2, and Na_2S. This might be the cause in our CTS thin films because Raman analysis allowed us to observe the beginning of Na_xCuSnS_3 secondary phase production in CTSN1 thin films. As a result, we saw a dramatic drop of the efficiency from to 1.03% for SNa1 to 0.17% for SNa5.

4.4.4. Li Doping effect on CTS thin films

As we mentioned in the previous section, doping had many good effects on the general properties on thin films. Compare to Na, Li atom wasn't as extensively studied in the literature as possible doping agent for the chalcogenide's thin films and specifically for CTS phases.

4.4.4.1. Li doped CTS Thin films structural properties (XRD)

In Figure 4.30, XRD pattern of Li doped CTS thin films with different concentrations is presented. It is very obvious that the position peaks in the X-ray diffraction plot didn't change when introducing Li atoms to the lattice of CTS materials without any secondary phases or impurities. The tetragonal Cu_2SnS_3 or orthorhombic Cu_3SnS_4 phases are the most probable existing phases just as previously mentioned. The crystallinity of the thin films witnessed an overall diminution when doping it with Li atoms.

In Figure 4.31.a, the crystalline size decreases by introducing Li atoms which confirm the integration of Li atoms into the lattice of CTS. The deposition rate of Li doped and non-doped thin films is also present in Figure 4.31.a. The reduction of the thin films deposition rate is very clear when the Li atoms incorporation increases. As it is sited previously, the augmentation of the doping concentration didn't enhance the crystalline sizes leading to the supposition that Li atoms introduces defects to the structure. These defects prevent the thin films from growing and increased the grain boundaries reducing by that the deposition rate (Roselin ve ark., 2019). This conception can be supported by the augmentation of the dislocation densities and the micro-strain in the Li doped CTS thin films present in Figure 4.31.b (Roselin ve ark., 2019).

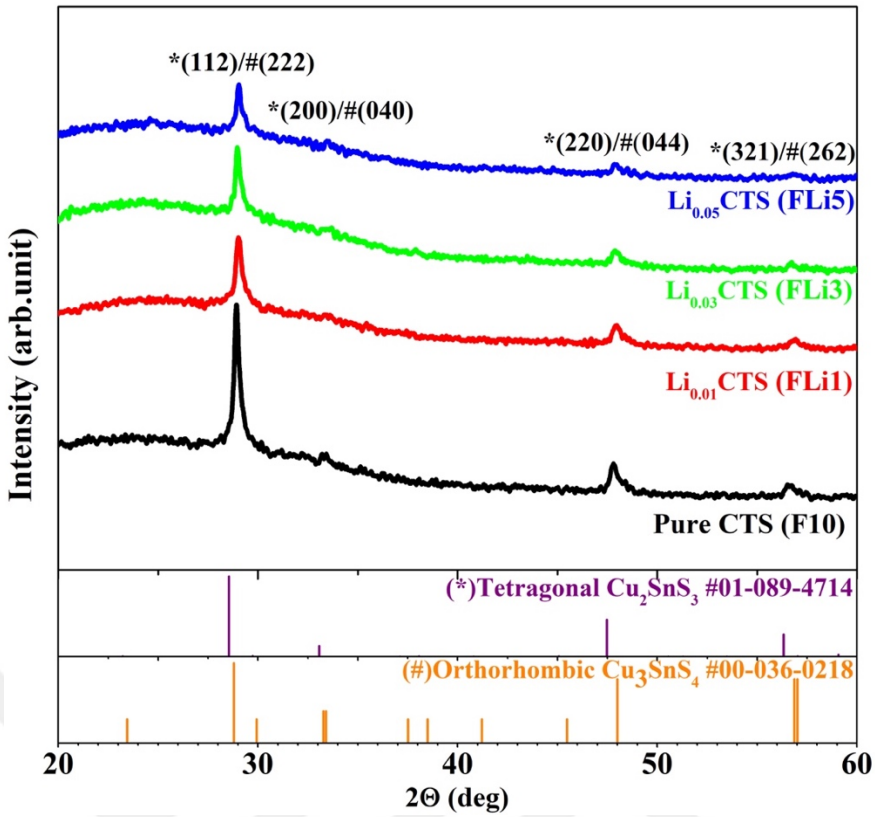

Figure 4. 30. X-ray diffraction of CTS thin films with different Li doping concentrations

Very few numbers of publication pointed the changing of thin film's thickness (increase (Rajeswari ve ark., 2021) or decrease (Huhtinen ve ark., 2012)) according to the doping concentration. In the work done by Peurla *et al.*(Peurla ve ark., 2007), they observe a noticeable drop in crystallinity of YBCO thin films deposited by PLD due to doping the targets. In the majority studies that mentioned the variation of the thickness due to the doping of thin films, we notice that the doping atoms are introduced to the films during the deposition process. This means that the doping atom exist in the precursors whether the deposition method in physical (Peurla ve ark., 2007; Huhtinen ve ark., 2009; Huhtinen ve ark., 2012) or chemical (M Hashem, 2016; Roselin ve ark., 2019; Sanchez ve ark., 2020).

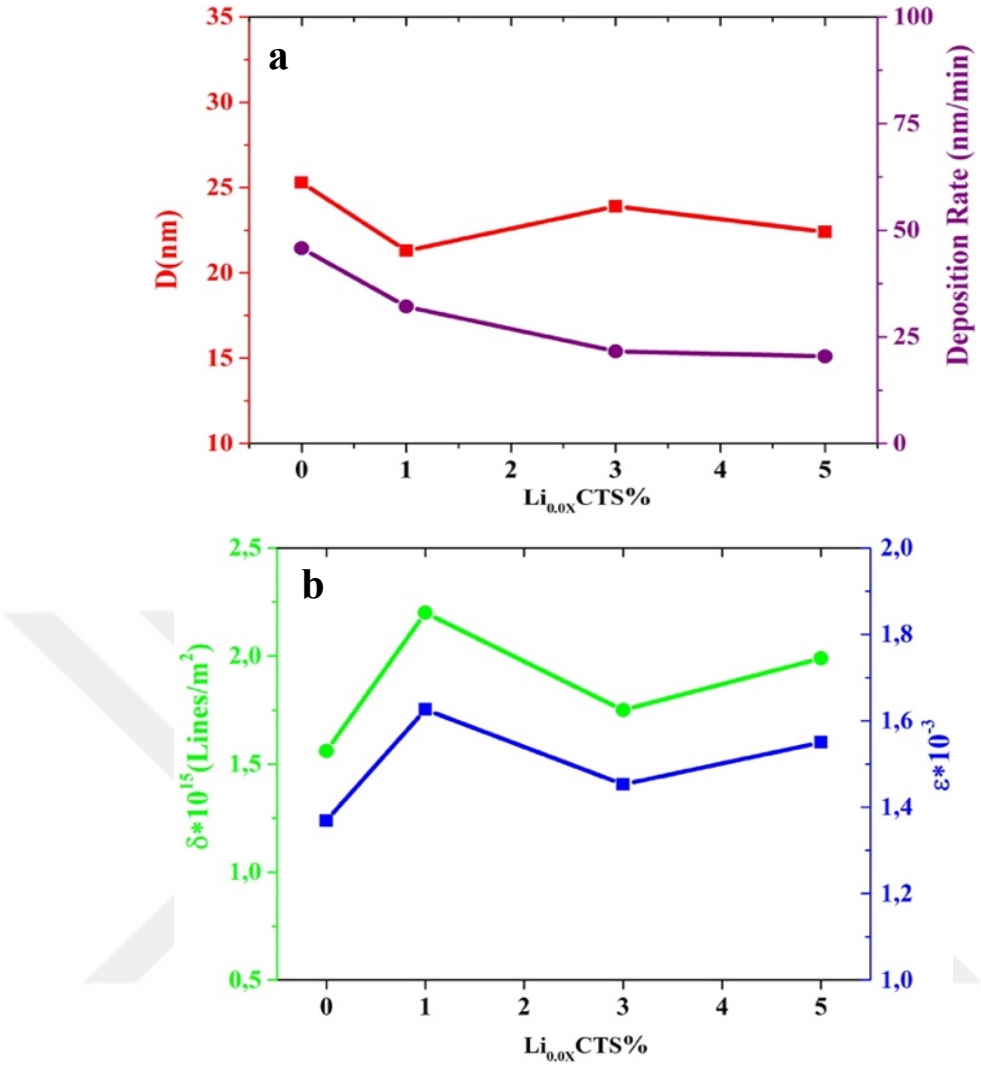

Figure 4. 31. a) Crystal size and deposition rate and b) density of dislocations and microstrain of CTS thin films with different Li doping concentrations

In our case, Li doping had in general effected the growth of the thin films and decrease its thickness. However, the crystalline size of FLi3 is still good compare to the big difference in the thickness between FP and FLi3 (see Table 4.13).

Table 4. 13. The thicknesses and crystalline sizes of FP, FLi1, FLi3 and FLi5 thin films

Samples	Thickness (nm)	Crystalline size D (nm)
FP	458	25.3
FLi1	321	21.3
FLi3	270	23.9
FLi5	204	22.4

4.4.4.2. Li doped CTS Thin films compositional properties

In Table 4.14, the ratios 'Cu/Sn and S/Metal' of the Li doped CTS thin films have been presented. It can be observed that the ratio Cu/Sn has the lowest values in FLi3 thin film

and in FLi1 thin film it has the highest one. The ratio of S/Metal is the lowest in FLi5 thin film. Regardless of the doping concentration of Li atom, FLi3 thin film presents the closest values to the stochiometric composition of CTS thin films. Furthermore, the Cu/Sn ratio in the FLi3 thin film falls from 2.36 to 2.12 when compared to pure CTS.

Table 4. 14. The atomic concentration of Li doped CTS thin film

Samples	Cu/Sn	S/Metal
FP	2.36	0.80
FLi1	2.81	0.76
FLi3	2.12	0.76
FLi5	2.36	0,74

4.4.4.3. Li doped CTS Thin films morphologic properties

In Figure 4.32. we presented the surface of CTS thin film with different Li doping concentrations. The particle on top of the surface that might represent Cu_xS_y secondary phases are decreasing in number and size when we introduced Li atoms.

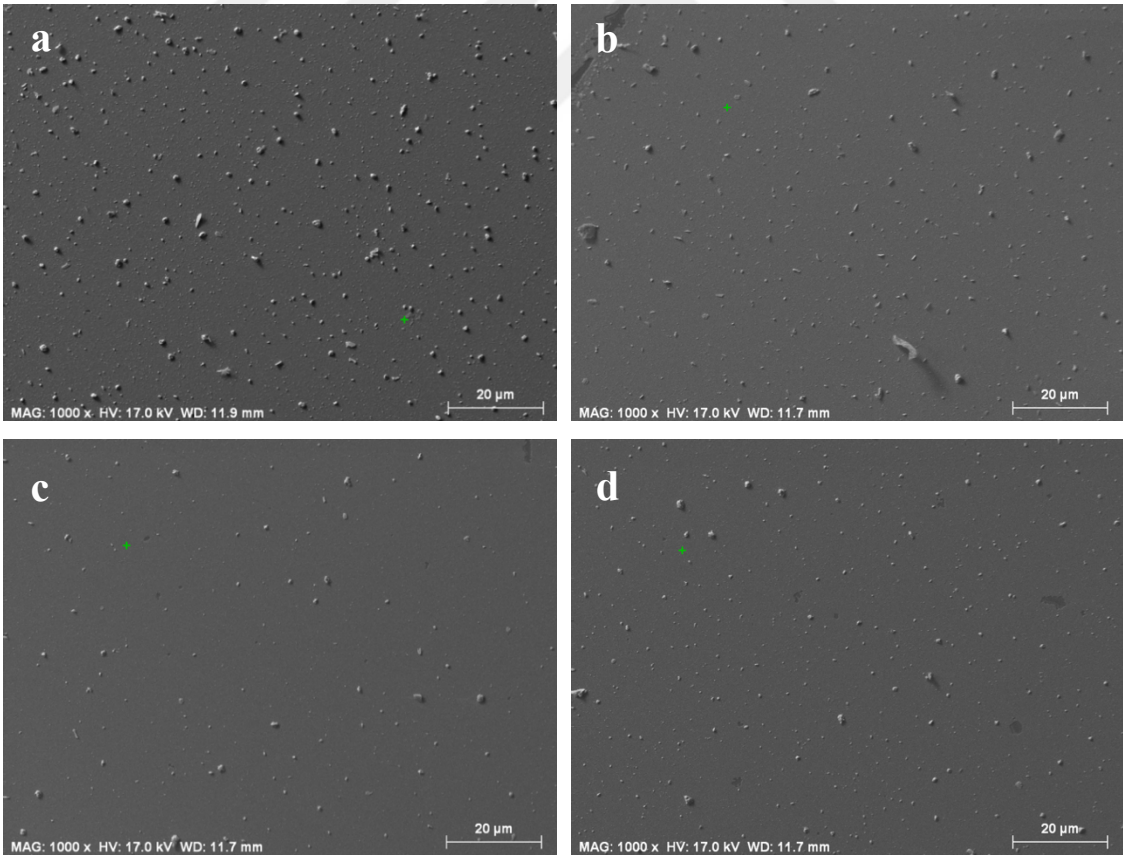

Figure 4. 32. SEM images of a) FP, b) FLi1, c) FLi3 and d) FLi5 thin films

FLi1 thin film (Figure 4.32.b) presents some cracks on its surface while FLi5 had some removed parts from its surface. These defects reduced the quality of the thin films as already seen in structural analyse. Among all Li doped thin films, FLi3 presents the smoothest surface with no visible defects. The crystalline size of FLi3 (23.9 nm) is close to the crystalline size of FP (25.3 nm) despite the large difference in their thicknesses. This shows that FLi3 is has the best quality in Li doped CTS fin films.

4.4.4.4. Li doped CTS Thin films optic properties

The absorption spectra of Li doped CTS thin films are present in Figure 4.33. In general, the absorption of CTS thin films decreased when we dope it with Li atoms at different concentration. This is an obvious outcome given that the thickness of $Li_{0.0X}$CTS thin films (see. Table 4.15) decreased significantly compare to FP thin films. The absorption of light photons by thin films is decreased as their thickness drops (Houimi ve ark., 2021).

We also notice that the absorption of FLi3 is higher than that of FLi1 irrespective to its smaller thickness. The enhancement of the crystallinity in FLi1 compare to FLi3 thin films reduced the grain boundaries and increased the optic absorption (Guo ve ark., 2021; Hosseinpour ve ark., 2021).

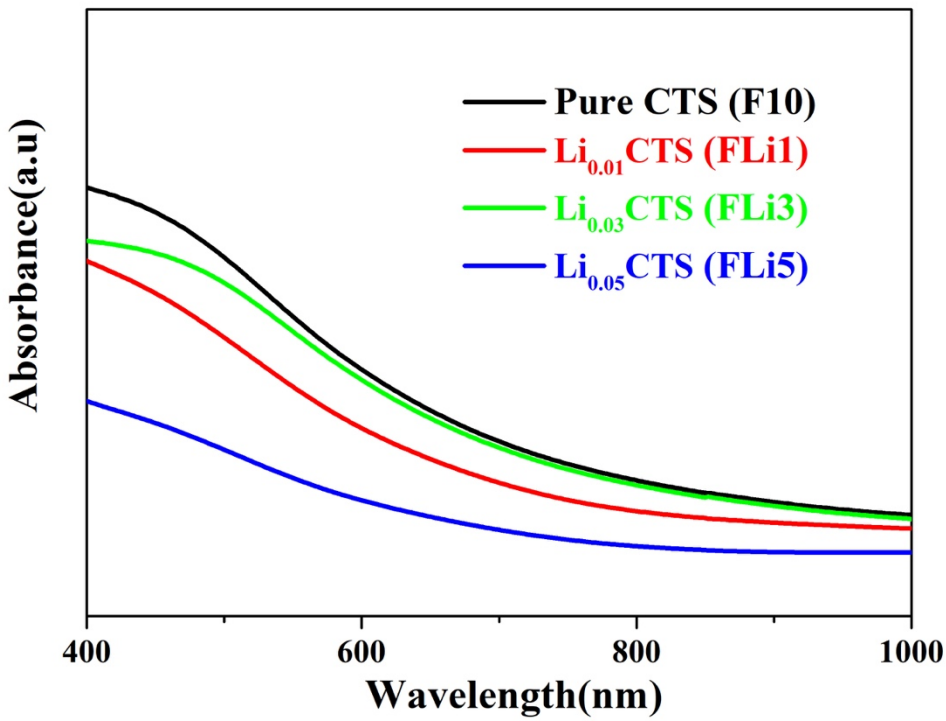

Figure 4. 33. Absorbance spectra of FP, FLi1, FLi3 and FLi5 thin films

Table 4. 15. The band gap energies, thicknesses and crystalline sizes FP, FLi1, FLi3 and FLi5 thin films

Samples	Eg (eV)	Thickness (nm)	Crystalline size D (nm)
FP	1.11	458	25.3
FLi1	1.02	321	21.3
FLi3	1.08	270	23.9
FLi5	1.05	204	22.4

The calculated band gaps of FLi1, FLi3 and FLi5 thin films are present in Table 4.15 and Figure 4.34. The decrease in the band gaps is referred to the diminution of the absorption edge (Guo ve ark., 2021; Hosseinpour ve ark., 2021). In earlier research, in Li doped CZTSSe materials, it was found that the optical band gap values decreased following Li doping concentration (Xin ve ark., 2015; Dong ve ark., 2021; Tong ve ark., 2021).

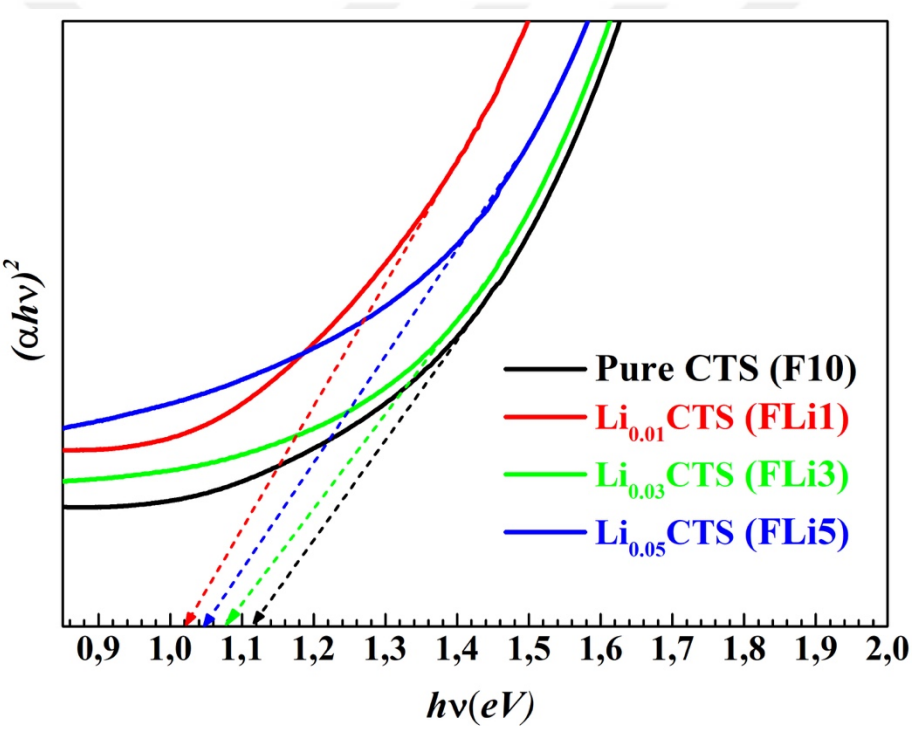

Figure 4. 34. Plot of $(\alpha h\nu)^2$ versus $h\nu$ of FP, FLi1, FLi3 and FLi5 thin films

4.4.5. Effect of Li doping on the characteristics of SLi1, SLi3 and SLi5

4.4.5.1. Properties of Al/Si/CTS/Ag diodes for Li doped and non-doped Cu_2SnS_3 (darkness)

Before we start the analyze of the obtained data in this section, it is very important to signify that each Li doped CTS thin film is incomparable to the other thin films since they have different thickness and different doping concentrations. It is excessive to evaluate the evolution of the different parameters according to the doping concentration or to the

thickness. Thus, the outcomes are explained according to FLi1, FLi3 and FLi5 thin films different properties.

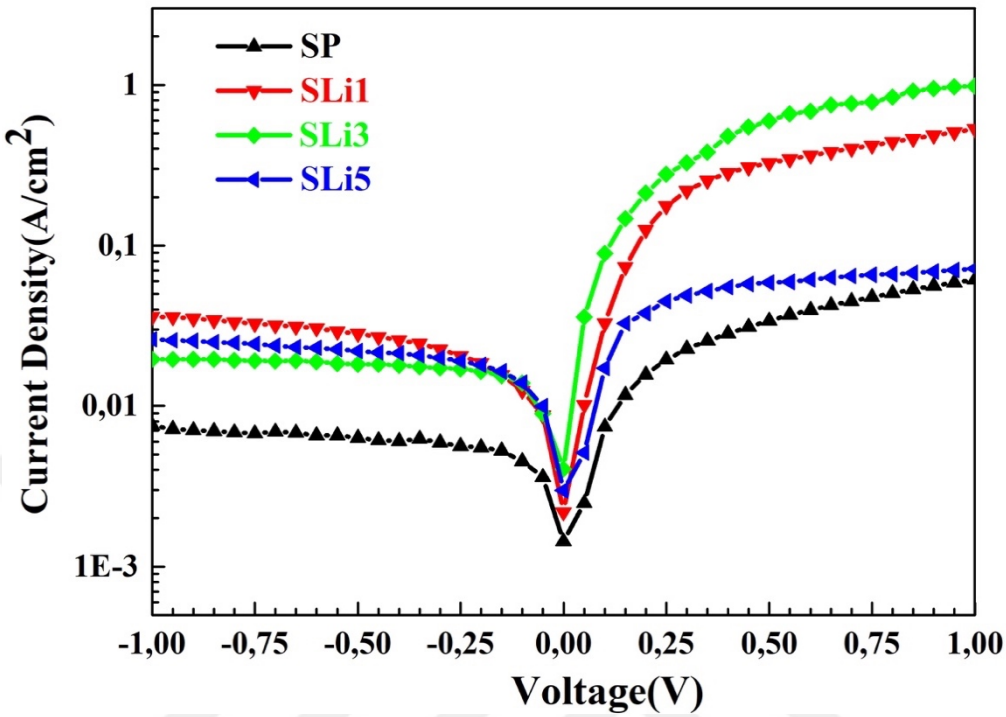

Figure 4. 35. I-V logarithmic plot of SP, SLi1, SLi3 and SLi5 in darkness

The I-V electric characteristics of SLi1, SLi3 and SLi5 diodes are present in Figure 4.35 and Table 4.16. All heterojunction diodes exhibit a distinct rectification behavior. The rectification ratio is maximum at SLi3 diodes (50.27) and minimum at SLi5 (2.75). The low rectification behavior of SLi5 diode might be due to poor crystallinity of the FLi5 thin film. The low crystalline size and the low thickness of the thin film implies bigger defect and traps number that block the charge transition in the heterojunction (Nasir ve Abass, 2016; Chávez-Urbiola ve ark., 2019; Ismail ve ark., 2019b).

Table 4. 16. Electric properties of SP, SLi1, SLi3 and SLi5 solar cells in darkness

Solar cell	R_R	m	J_0*10^{-3} mA/cm^2	Thickness (nm)	Crystalline size D (nm)
SP	8.13	2.41	8.89	458	25.3
SLi1	14.73	2.88	41.21	321	21.3
SLi3	50.27	2.12	20.76	270	23.9
SLi5	2.75	3.67	28.89	204	22.4

The saturation currents J_0 of the prepared diodes increased by decreasing the crystalline size of the thin films regardless of the thickness or the doping concentration. We can referred this comportment the augmentation of the recombination in the thin films due to

the accumulated stress and defects in the thin films samples (Zhang ve ark., 2020; Gezgin ve ark., 2021). Namely, the biggest saturation current was measured in SLi1 where we notice poor morphologic properties and cracks on the surface of the thin film (see section 4.4.4.3).

Generally, the values of the ideality factor are larger than $2(2 < m)$. Ar a result, the dominant current in the transport mechanism is the recombination current (Ismail ve ark., 2019a; Ojeda-Durán ve ark., 2020). The decrease in m of SLi3 (2.12) compare to SP (2.41) denote more ideal behaviour of the diode. As seen in section 4.4.4.3, FLi3 presents the smoother surface with no visible defects (Cu_xS_y secondary phases) if we compare it with FP thin film. The reduction in the interfacial defect states that serve as carriers trapping sites may be responsible for the decreasing of the ideality factor values (Du ve ark., 2014). SLi5 diode, has the bigger ideality factor with the lower rectification rate among all the prepared diodes; 3.67 and 2.75, respectively. This indicates the low quality of this diode (Zhu ve ark., 2005; Bo ve ark., 2009; Gupta ve ark., 2009; 2010; Jing-Jing ve ark., 2010).

4.4.5.2. PV properties SP, SLi1, SLi3 and SLi5 solar cells (illumination)

Figure 4.36 and Table 4.17, respectively, show the I-V characteristics of SP, SLi1, SLi3, and SLi5 solar cells under light with the values of solar cell parameters. According to the reference solar cell SP, only SLi3 solar cell showed an improvement in its performance under illumination. V_{oc}, I_{sc}, FF and η increased from 240 mV, 7.72 mA/cm^2, 19.4 % and 0.45 % to 265 mV, 10.28 mA/cm^2, 22.97 % and 0.78 %.

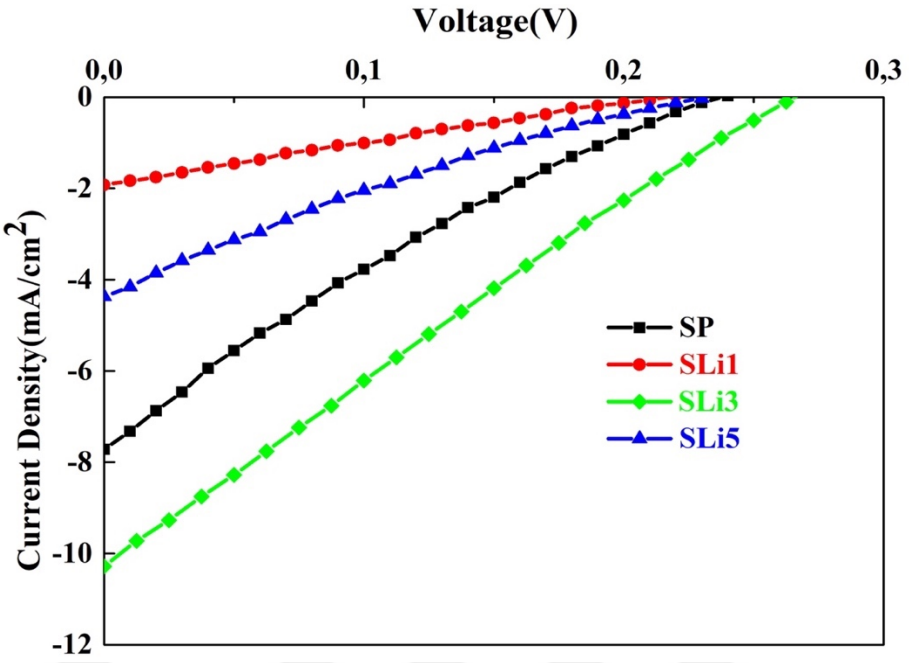

Figure 4. 36. I-V logarithmic plot of SP, SLi1, SLi3 and SLi5 solar cells under AM 1.5G. illumination

The causes for the increase of solar cells in this instance might be classified into two main reasons:

- We have shown in prior analyses of the characteristics of Li doped CTS thin films (FLi3) that, despite the decreasing of thickness, the crystalline size did not significantly decrease, while the surface morphology was remarkably improved with less visible defects (Cu_xS_y secondary phases). This will reduces the interfacial defect states that serve as carriers trapping sites (Du ve ark., 2014). Prior studies on the integration of Li in kesterite materials has confirmed some excellent improvements in the solar cell performance. Li doping reduced the grain boundaries that declined the number of the scattering centers of charge carriers (Hsieh ve ark., 2016; Wang ve ark., 2018; Dong ve ark., 2021; Tong ve ark., 2021). This is further supported by the decline in Li doped CTS crystal number. It is firmly believed that these improvements would unquestionably increase the PV characteristics of our Li doped heterojunction solar cell. Not to mention that the SLi3 diode outperformed the SP diode with a lower ideality factor (2.12) and a greater rectification ratio (50.27).
- The reduction in CTS thin film thickness also has a significant impact on the performance of our products. At thicker CTS layer, the majority of photons are absorbed far from the space-charge (depletion) region (CTS/n-Si interface). As a result, a greater distance must be travelled by photo-generated electrons before they

can arrive to depletion arrive at the region, which increases the likelihood of recombination. When we compared the thickness of FP to FLi3 thin film, the diffusion length of charge carriers with photoelectrons is longer. Thus, before reaching the depletion zone, these charge carriers may undergo recombination at trap sites inside the CTS thin film or on Ag front contact (Wei-Ying ve ark., 2008; Moon ve ark., 2014; Deng ve ark., 2017).

Table 4. 17. Optoelectric properties of SP, SLi1, SLi3 and SLi5 solar cells in illumination

Abbreviation of solar cell	V_{oc} (mV)	I_{sc} (mA/cm^2)	FF (%)	η (%)
SP	240	7.72	19.4	0.45
SLi1	215	1.92	26.14	0.14
SLi3	265	10.28	22.97	0.78
SLi5	230	4.37	18.61	0.24

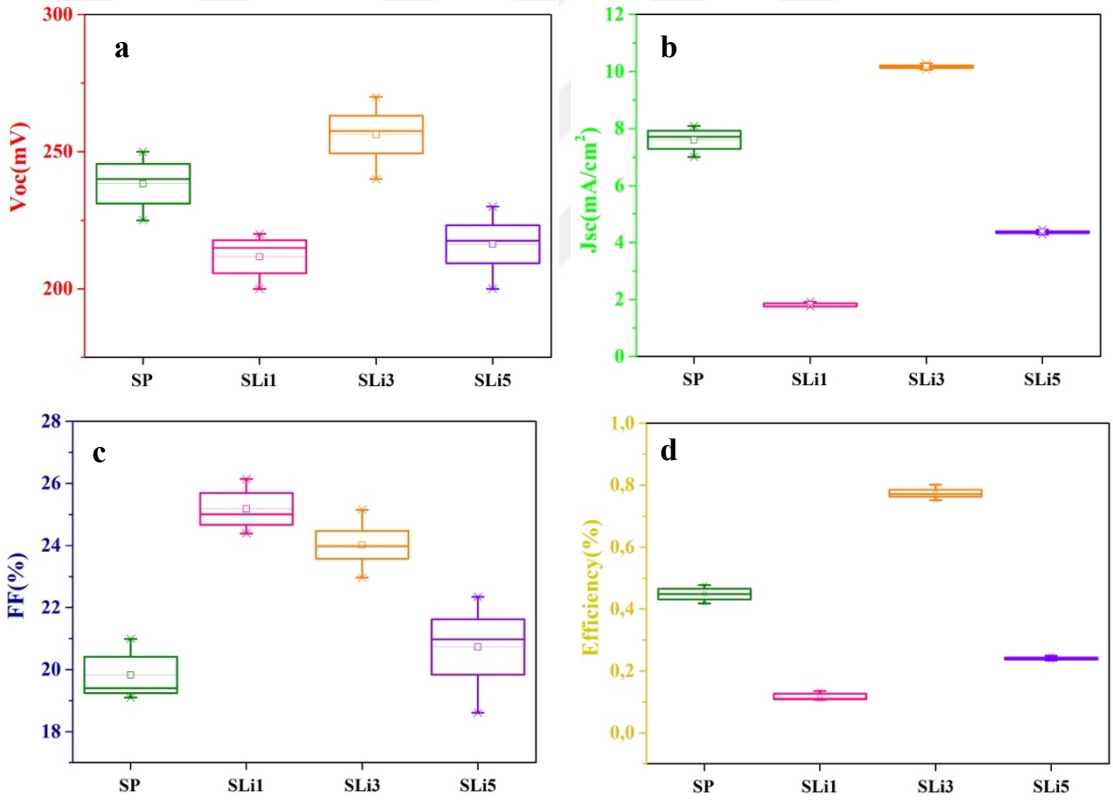

Figure 4. 37. Boxplot of SP, SLi1, SLi3 and SLi5 solar cells parameters

As for SLi1 and SLi5, their performance was poor compare to SP solar cells (see Figure 4.37) with a remarkable drop of η to 0.14% and 0.24, respectively. This decline in their performance was expected due to the poor crystallinity of both thin films FLi1 and FLi5. This will increase the probability of electro hole recombination which will augment the

saturation current and the ideality factor . on the other hand, the poor surface of FLi1 and FLi5 thin films reduced the quality of the junction and decreased the collection of charge which will decrease the short circuit current and eventually the efficiency of solar cells (Shin ve ark., 2011; Shin ve ark., 2013; Kim ve ark., 2016b).

5. GENERAL CONCLUSION

This thesis illustrates the deposition and analyse of Alkali atoms doped Cu_2SnS_3 thin films for photovoltaic applications. The production of CTS thin films was done using PLD technique using home-made targets. The home-made targets were prepared using mechanical alloying process.

CTS powder was formed by means of mechanical alloying technique “ball milling” using elemental powder (Cu, Sn, S) in wet medium. The wet ball milling obstructs the formation of Cu-Sn-S ternary phases and instead we only notice the formation of CuS hexagonal phase and Sn tetragonal phase in the XRD pattern. This indicate a non-complete mechanical alloying.

For CTS target, the prepared CTS powder was pressed into 12 mm target and then sintered for 2h at 600°C and 700°C. At 600°C, the XRD analyse shown the formation of the wanted Cu_2SnS_3 with tetragonal structure while the EDX analyse resulted in near stochiometric atomic composition that confirm the XRD results. Annealing the CTS target at 700°C revealed copper rich phases (CuS and Cu_3SnS_4) that were formed due to the diminution of Sn concentration. The cause of Sn ratio decrease in the target was explain by the evaporation of SnS material during high temperature annealing. As a conclusion, targets annealed at 600°C with Cu_2SnS_3 phase are adopted for further thin films deposition with PLD technique.

The deposition of CTS thin films was conducted in room temperature with different deposition duration. The study concerning the influence of sulfurization temperature showed a very big difference of the resulted properties of CTS thin films. An amorphous structure is what we observed in the as deposited thin films. As the sulfurization temperature augment from 400°C to 550°C we observe a polycrystalline nature of the thin films with a formation of CTS phase. Enhancement of the crystallinity and the stochiometric composition of the CTS thin films was the most notable observation with the increase of the absorbance and thin films texture. When the temperature reached 600°C, the evaporation of SnS material from the thin films influenced the structure and composition of CTS thin films by the presence of CuS phase in XRD results with copper rich composition of F600. The optical analyses revealed a decreasing of the thin film’s absorbance with a big augmentation of the optical band gap energy. At the end, we can conclude that sulfurization process had a good influence at low T. However, as the temperature went high the opposite effect was observe by the appearance of secondary phases and the deficiency of Sn atom.

The deposition time had a very notable impact on increasing the thickness of CTS thin films from 138 nm to 623 nm. The crystallin size also increased with enhancement of the film's crystallinity and diminution of the band gap energy. On the hand the thickness augmentation changed the morphology of CTS thin films, where more textured thin films with larger particles sizes were formed.

Using Na atom for CTS doping with different concentration was largely analyzed and studied. The structural analyzed using XRD and RAMAN shown the existence of two phases of Cu-Sn-S ternary of Cu_2SnS_3 and Cu_3SnS_4 ternary materials. The enhancement of the thin film's quality was only observed at low doping concentration and then the over-doping with Na atoms decreased the particle size with augmentation of the optical band gap.

Doping of thin films is known to change the structure and the grain size of thin films. In our case using four doping atoms (Li, Na) with different concentration resulted in diverse outcome, where the doping influence not only the crystallinity and the morphology but also the thickness of the thin film. This was the case with Li atoms doping. we notice a dramatic drop in the thickness of CTS thin films and diminutions of the crystalline size and the absorbance. However, in the case of FLi3 thin films, the crystalline number was lower and the absorption coefficient was better compared to the non-doped thin film FP. The SEM analyse also showed better surface of FLi3 thin film.

The heterojunction thin film solar cells Al/n-Si/CTS/Ag were produced using different doping concentration of Na and Li atoms into CTS thin films. In the darkness, SP, SNa1, SNa3 and SNa5 diodes showed very noticeable ratification behaviours with a very high rectification ratio in SNa1 of 297.44. The doping with Na atom at 1% ratio improved the quality of the diode by lowering its reversed saturation current and ideality factor while the opposite phenomenon happens due to the excess doping in FNa3 and FNa5. Under illumination conditions, the I-V characteristics of Al/n-Si/CTS/Ag heterojunction solar cells showed an increase at low doping concentration of Na and diminution in high Na doping ratios. The improvement of the crystallinity of FNa1 with passivation of the grain boundaries upgraded in general the J-V parameters of the SNa1 compare to SP solar cells, where V_{oc} and FF values raised from 240 mV to 290 mV and from 19.4% to 28.67%, respectively. Additionally, short circuit current I_{sc} increased its values from 7.72 mA/cm^2 to 9.89 mA/cm^2. Due to that, we saw an increase in the η from 0.45% to 1.03%.

In case of Li doped CTS based solar cells, two outcomes of Li doping were the main factors that affect the performance the devices which were the morphology and the

thickness of the thin films. Doping with Li atom increased only the SLi3 solar cell performance under light compared to the reference solar cell SP. Its optoelectric properties V_{oc}, I_{sc}, FF and η increased to 265 mV, 10.28 mA/cm^2, 22.97 % and 0.78 %, respectively compared to 240 mV, 7.72 mA/cm^2, 19.4 % and 0.45 % of SP of non-doped CTS thin films. It was exhibited that even though the decrease of the crystalline size of the $Li_{0.03}$CTS according to non-doped CTS thin films its surface morphology enhanced. As a result, we saw a decrease in the ideality factor (2.12) and a greater rectification ratio (50.27) of SLi3 diodes. On the other hand, the thickness reduction must have a major effect on the performance of SLi3 solar cell by elevating the collection of the photogenerated charges at the front contact. When compared to SP solar cells, the performance of SLi1 and SLi5 was poor, with η dropping noticeably to 0.14% and 0.24%, respectively. Because both thin films FLi1 and FLi5 have weak crystallinity, this reduction in performance was anticipated. On the other hand, the poor surface of FLi1 and FLi5 thin films reduced the quality of the junction and decreased the collection of charge, which in turn decreased the short circuit current and ultimately the efficiency of solar cells.

REFERENCES

Abdel-Latif, M. S., Magdy, W., Tosuke, T., Kanai, A., Hessein, A., Shaalan, N., Nakamura, K., Sugiyama, M. ve Abdel-Moniem, A., 2020, A comprehensive study on Cu2SnS3 prepared by sulfurization of Cu–Sn sputtered precursor for thin-film solar cell applications, *Journal of Materials Science: Materials in Electronics*, 31 (17), 14577-14590.

Abdel-Latif, M. S., Rezk, A., Abdel-Moniem, A. ve Hessein, A., 2021, Effect of Sulfur Precursors on Crystallographic, Optical, and Electrical Properties of Cu2SnS3 Nanoparticles.

Agrawal, A., Siddiqui, S. A., Soni, A. ve Sharma, G. D., 2022, Advancements, frontiers and analysis of metal oxide semiconductor, dye, electrolyte and counter electrode of dye sensitized solar cell, *Solar Energy*, 233, 378-407.

Aihara, N., Kanai, A., Kimura, K., Yamada, M., Toyonaga, K., Araki, H., Takeuchi, A. ve Katagiri, H., 2014, Sulfurization temperature dependences of photovoltaic properties in Cu2SnS3-based thin-film solar cells, *Japanese journal of applied physics*, 53 (5S1), 05FW13.

Alonso, M. I., Garriga, M., Durante Rincón, C., Hernández, E. ve León, M., 2002, Optical functions of chalcopyrite CuGaxIn1-xSe2 alloys, *Applied Physics A*, 74 (5), 659-664.

Altamura, G., Wang, M. ve Choy, K.-L., 2016, Influence of alkali metals (Na, Li, Rb) on the performance of electrostatic spray-assisted vapor deposited Cu 2 ZnSn (S, Se) 4 solar cells, *Scientific reports*, 6, 22109.

Angleraud, B., Garrelie, F., Tetard, F. ve Catherinot, A., 1999, Study of particles ejected after pulsed laser ablation of a graphite target, *Applied Surface Science*, 138, 507-511.

Antar, E., 2014, Effect of γ-ray on optical characteristics of dyed PVA films, *Journal of Radiation Research and Applied Sciences*, 7 (1), 129-134.

Ashfold, M. N., Claeyssens, F., Fuge, G. M. ve Henley, S. J., 2004, Pulsed laser ablation and deposition of thin films, *Chemical Society Reviews*, 33 (1), 23-31.

Avellaneda, D., Nair, M. ve Nair, P., 2010, Cu2SnS3 and Cu4SnS4 thin films via chemical deposition for photovoltaic application, *Journal of the Electrochemical Society*, 157 (6), D346-D352.

Avellaneda, D., Paul, A., Shaji, S. ve Krishnan, B., 2022, Synthesis of Cu2SnS3, Cu3SnS4, and Cu4SnS4 thin films by sulfurization of SnS-Cu layers at a selected temperature and/or Cu layers thickness, *Journal of Solid State Chemistry*, 306, 122711.

Azulay, D., Abou-Ras, D., Popov, I., Balberg, I. ve Millo, O., 2016, The effect of Na on the electronic properties of Cu (In, Ga) Se2 thin films: A local-probe study, *physica status solidi (RRL)–Rapid Research Letters*, 10 (6), 448-452.

Baláž, M., Zorkovská, A., Urakaev, F., Baláž, P., Briančin, J., Bujňáková, Z., Achimovičová, M. ve Gock, E., 2016, Ultrafast mechanochemical synthesis of copper sulfides, *RSC Advances*, 6 (91), 87836-87842.

Baláž, M., Daneu, N., Rajňák, M., Kurimský, J., Hegedüs, M., Dutková, E., Fabián, M., Kaňuchová, M. ve Baláž, P., 2018, Rapid mechanochemical synthesis of nanostructured mohite Cu 2 SnS 3 (CTS), *Journal of materials science*, 53 (19), 13631-13642.

Baranowski, L. L., Zawadzki, P., Christensen, S., Nordlund, D., Lany, S., Tamboli, A. C., Gedvilas, L., Ginley, D. S., Tumas, W. ve Toberer, E. S., 2014, Control of

doping in Cu2SnS3 through defects and alloying, *Chemistry of Materials*, 26 (17), 4951-4959.

Baranowski, L. L., 2015, Combinatorial development of Cu_2SnS_3 as an earth abundant photovoltaic absorber, *2015-Mines Theses & Dissertations*.

Baranowski, L. L., Zawadzki, P., Lany, S., Toberer, E. S. ve Zakutayev, A., 2016, A review of defects and disorder in multinary tetrahedrally bonded semiconductors, *Semiconductor Science and Technology*, 31 (12), 123004.

Basak, A., Deka, H., Mondal, A. ve Singh, U. P., 2018, Impact of post-deposition annealing in Cu2SnS3 thin film solar cells prepared by doctor blade method, *Vacuum*, 156, 298-301.

Belaqziz, M., Medjnoun, K., Djessas, K., Chehouani, H. ve Grillo, S., 2018, Structural and optical characterizations of Cu2SnS3 (CTS) nanoparticles synthesized by one-step green hydrothermal route, *Materials Research Bulletin*, 99, 182-188.

Benjamin, J. S., 1970, Dispersion strengthened superalloys by mechanical alloying, *Metallurgical transactions*, 1 (10), 2943-2951.

Berg, D. M., Djemour, R., Gütay, L., Siebentritt, S., Dale, P. J., Fontane, X., Izquierdo-Roca, V. ve Pérez-Rodriguez, A., 2012, Raman analysis of monoclinic Cu2SnS3 thin films, *Applied Physics Letters*, 100 (19), 192103.

Bisquert, J., 2017, The physics of solar cells: perovskites, organics, and photovoltaic fundamentals, CRC press, p.

Bo, H., Quan, M. Z., Jing, X., Lei, Z., Sheng, Z. N., Feng, L., Cheng, S., Ling, S., Yue, Z. C. ve Shan, Y. Z., 2009, Characterization of AZO/p-Si heterojunction prepared by DC magnetron sputtering, *Materials science in semiconductor processing*, 12 (6), 248-252.

Boch, P., 2001, Matériaux et processus céramiques, *Hermes Science, Paris*, 109-139.

Bodeux, R., Leguay, J. ve Delbos, S., 2015, Influence of composition and annealing on the characteristics of Cu2SnS3 thin films grown by cosputtering at room temperature, *Thin Solid Films*, 582, 229-232.

Bouaziz, M., Amlouk, M. ve Belgacem, S., 2009, Structural and optical properties of Cu2SnS3 sprayed thin films, *Thin Solid Films*, 517 (7), 2527-2530.

Bouaziz, M., Ouerfelli, J., Srivastava, S., Bernède, J. ve Amlouk, M., 2011, Growth of Cu2SnS3 thin films by solid reaction under sulphur atmosphere, *Vacuum*, 85 (8), 783-786.

Breeh, F. ve Cross, K., 1962, Optical Microemission stimulated by a ruby laser", *Appl Spectrsc*, 16, 59.

Cabas-Vidani, A., Haass, S. G., Andres, C., Caballero, R., Figi, R., Schreiner, C., Márquez, J. A., Hages, C., Unold, T. ve Bleiner, D., 2018, High-Efficiency (LixCu1− x) 2ZnSn (S, Se) 4 Kesterite Solar Cells with Lithium Alloying, *Advanced Energy Materials*, 8 (34), 1801191.

Chantana, J., Suzuki, K. ve Minemoto, T., 2017a, Introduction of Na into Cu2SnS3 thin film for improvement of its photovoltaic performances, *Solar Energy Materials and Solar Cells*, 168, 207-213.

Chantana, J., Uegaki, H. ve Minemoto, T., 2017b, Influence of Na in Cu2SnS3 film on its physical properties and photovoltaic performances, *Thin Solid Films*, 636, 431-437.

Chaudhari, J. ve Joshi, U., 2018, Fabrication of high quality Cu2SnS3 thin film solar cell with 1.12% power conversion efficiency obtain by low cost environment friendly sol-gel technique, *Materials Research Express*, 5 (3), 036203.

Chávez-Urbiola, I. R., Willars-Rodríguez, F., Bon, R. R., Vorobiev, P. ve Vorobiev, Y. V., 2019, Development and characterization of photodiode n-ZnO/p-Si by Radio

Frecuency Sputtering, a sensor with low voltage operation and its response to visible and UV light, *Thin Solid Films*, 669, 364-370.

Chen, Q., Dou, X., Ni, Y., Cheng, S. ve Zhuang, S., 2012, Study and enhance the photovoltaic properties of narrow-bandgap Cu2SnS3 solar cell by p–n junction interface modification, *Journal of colloid and interface science*, 376 (1), 327-330.

Chen, S., Yang, J.-H., Gong, X.-G., Walsh, A. ve Wei, S.-H., 2010, Intrinsic point defects and complexes in the quaternary kesterite semiconductor Cu 2 ZnSnS 4, *Physical Review B*, 81 (24), 245204.

Chen, S., Walsh, A., Gong, X. G. ve Wei, S. H., 2013, Classification of lattice defects in the kesterite Cu2ZnSnS4 and Cu2ZnSnSe4 earth-abundant solar cell absorbers, *Advanced Materials*, 25 (11), 1522-1539.

Chino, K., Koike, J., Eguchi, S., Araki, H., Nakamura, R., Jimbo, K. ve Katagiri, H., 2012, Preparation of Cu2SnS3 thin films by sulfurization of Cu/Sn stacked precursors, *Japanese journal of applied physics*, 51 (10S), 10NC35.

Cho, Y., Kim, D.-W., Ahn, S., Nam, D., Cheong, H., Jeong, G. Y., Gwak, J. ve Yun, J. H., 2013, Recombination in Cu (In, Ga) Se2 thin-film solar cells containing ordered vacancy compound phases, *Thin Solid Films*, 546, 358-361.

Dahman, H. ve El Mir, L., 2015, Cu2SnS3 thin films deposited by spin coating route: a promise candidate for low cost, safe and flexible solar cells, *Journal of Materials Science: Materials in Electronics*, 26 (8), 6032-6039.

Deng, T., Gotoh, K., Takabe, R., Xu, Z., Yachi, S., Yamashita, Y., Toko, K., Usami, N. ve Suemasu, T., 2017, Boron-doped p-BaSi2/n-Si solar cells formed on textured n-Si (0 0 1) with a pyramid structure consisting of {1 1 1} facets, *Journal of Crystal Growth*, 475, 186-191.

Dijkkamp, D., Venkatesan, T., Wu, X., Shaheen, S., Jisrawi, N., Min-Lee, Y., McLean, W. ve Croft, M., 1987, Preparation of Y-Ba-Cu oxide superconductor thin films using pulsed laser evaporation from high T c bulk material, *Applied Physics Letters*, 51 (8), 619-621.

Dong, X.-F., Zheng, T.-T., Yang, F.-X., Sun, X.-D., Yu, L., Chen, J.-T., Wang, C.-W., Zhao, Y. ve Li, Y., 2021, An effective Li-containing interfacial-treating strategy for performance enhancement of air-processed CZTSSe solar cells, *Solar Energy Materials and Solar Cells*, 227, 111102.

Dong, Y., He, J., Sun, L., Chen, Y., Yang, P. ve Chu, J., 2015, Effect of sulfurization temperature on properties of Cu2SnS3 thin films and solar cells prepared by sulfurization of stacked metallic precursors, *Materials Science in Semiconductor Processing*, 38, 171-176.

Dong, Y., He, J., Li, X., Chen, Y., Sun, L., Yang, P. ve Chu, J., 2016, Study on the preheating duration of Cu2SnS3 thin films using RF magnetron sputtering technique for photovoltaics, *Journal of Alloys and Compounds*, 665, 69-75.

Du, W., Baba, M., Toko, K., Hara, K. O., Watanabe, K., Sekiguchi, T., Usami, N. ve Suemasu, T., 2014, Analysis of the electrical properties of Cr/n-BaSi2 Schottky junction and n-BaSi2/p-Si heterojunction diodes for solar cell applications, *Journal of applied physics*, 115 (22), 223701.

Ettlinger, R. B., Cazzaniga, A., Canulescu, S., Pryds, N. ve Schou, J., 2015, Pulsed laser deposition from ZnS and Cu2SnS3 multicomponent targets, *Applied Surface Science*, 336, 385-390.

Ettlinger, R. B., Crovetto, A., Canulescu, S., Cazzaniga, A., Ravnkilde, L., Youngman, T., Hansen, O., Pryds, N. ve Schou, J., 2016, Formation of copper tin sulfide films by pulsed laser deposition at 248 and 355 nm, *Applied Physics A*, 122 (4), 466.

Fang, S., Tao, T., Cao, H., Zheng, X., Hu, Y., Zhang, Y. ve Sun, Z., 2019, Selective Recovery of Gallium (Indium) from Metal Organic Chemical Vapor Deposition Dust—A Sustainable Process, *ACS Sustainable Chemistry & Engineering*, 7 (10), 9646-9654.

Ferhati, H. ve Djeffal, F., 2018, Graded band-gap engineering for increased efficiency in CZTS solar cells, *Optical Materials*, 76, 393-399.

Fernandes, P., Salomé, P. ve Da Cunha, A., 2010, A study of ternary Cu2SnS3 and Cu3SnS4 thin films prepared by sulfurizing stacked metal precursors, *Journal of Physics D: Applied Physics*, 43 (21), 215403.

Feurer, T., Fu, F., Weiss, T. P., Avancini, E., Löckinger, J., Buecheler, S. ve Tiwari, A. N., 2019, RbF post deposition treatment for narrow bandgap Cu (In, Ga) Se2 solar cells, *Thin Solid Films*, 670, 34-40.

Fiechter, S., Martinez, M., Schmidt, G., Henrion, W. ve Tomm, Y., 2003, Phase relations and optical properties of semiconducting ternary sulfides in the system Cu–Sn–S, *Journal of Physics and Chemistry of Solids*, 64 (9-10), 1859-1862.

Fujioka, H., 2015, Pulsed laser deposition (PLD), In: Handbook of Crystal Growth, Eds: Elsevier, p. 365-397.

Gers, R., 2009, Analyse locale de l'hydrodynamique d'un broyeur à billes agité pour le traitement de dispersions solide-liquide.

Gezgin, S. Y., Kılıç, H. Ş., Kepceoğlu, A., Bayır, S., Nalbantoğlu, İ. E. ve Toprak, A., 2016, Plasmonic tuning of gold doped thin films for layers of photovoltaic devices, *AIP Conference Proceedings*, 200013.

Gezgin, S. Y., Kepceoğlu, A., Toprak, A., Gündoğdu, Y. ve Kılıç, H. Ş., 2018, Diode property of n-ZnO/p-Si heterojunction structure in the dark and illumination condition.

Gezgin, S. Y. ve Kılıç, H. Ş., 2019, The electrical characteristics of ITO/CZTS/ZnO/Al and ITO/ZnO/CZTS/Al heterojunction diodes, *Optik*, 182, 356-371.

Gezgin, S. Y., Houimi, A., Mercimek, B. ve Kiliç, H. Ş., 2020, The Effect of CZTS Ultrathin Film Thickness on the Electrical Characteristic of CZTS/Si Heterojunction Solar Cells in the Darkness and under the Illumination Conditions, *Silicon*, 1-13.

Gezgin, S. Y., Houimi, A., Gündoğdu, Y., Mercimek, B. ve Kiliç, H. Ş., 2021, Determination of photovoltaic parameters of CIGS hetero junction solar cells produced by PLD technique, using SCAPS simulation program, *Vacuum*, 110451.

Gezgin, S. Y., Houimi, A., Mercimek, B. ve Kiliç, H. Ş., 2022, The Investigation of Photovoltaic and Electrical Properties of Bi Doped CTS/Si Hetero-Junction Structure for the Solar Cell Application, *Cumhuriyet Science Journal*, 43 (1), 137-145.

Green, M., Dunlop, E., Hohl-Ebinger, J., Yoshita, M., Kopidakis, N. ve Hao, X., 2021, Solar cell efficiency tables (version 57), *Progress in Photovoltaics: Research and Applications*, 29 (1), 3-15.

Guan, H., Shen, H., Gao, C. ve He, X., 2013, Structural and optical properties of Cu 2 SnS 3 and Cu 3 SnS 4 thin films by successive ionic layer adsorption and reaction, *Journal of Materials Science: Materials in Electronics*, 24 (5), 1490-1494.

Guddeti, P. R., Gedi, S. ve Reddy, K. R., 2018, Sulfurization temperature dependent physical properties of Cu2SnS3 films grown by a two-stage process, *Materials Science in Semiconductor Processing*, 86, 164-172.

Guitouni, S. ve Attaf, N., 2017, Elaboration et étude de structures à base de couches minces de ZnO et de chalcogénures (CIS, CZTS) pour des applications photovoltaïques, جامعة الإخوة منتوري قسنطينة.

Guo, J., Sun, S., Liu, B., Hao, R. ve Sun, L., 2021, Influence of Na2S treatment on CZTS/Mo interface in Cu2ZnSnS4 solar cells annealed in sulfur-free atmosphere, *Optik*, 242, 166998.

Gupta, R., Ghosh, K. ve Kahol, P., 2009, Fabrication and electrical characterization of Au/p-Si/STO/Au contact, *Current Applied Physics*, 9 (5), 933-936.

Gupta, R., Ghosh, K. ve Kahol, P., 2010, Temperature dependence of current–voltage characteristics of gold–strontium titanate thin film Schottky diode, *Physica E: Low-dimensional Systems and Nanostructures*, 42 (5), 1509-1512.

Han, J., Zhou, Y., Tian, Y., Huang, Z., Wang, X., Zhong, J., Xia, Z., Yang, B., Song, H. ve Tang, J., 2014, Hydrazine processed Cu2SnS3 thin film and their application for photovoltaic devices, *Frontiers of Optoelectronics*, 7 (1), 37-45.

He, M., Lokhande, A., Kim, I. Y., Ghorpade, U., Suryawanshi, M. ve Kim, J. H., 2017, Fabrication of sputtered deposited Cu2SnS3 (CTS) thin film solar cell with power conversion efficiency of 2.39%, *Journal of Alloys and Compounds*, 701, 901-908.

He, Q., Hu, Z., Yu, X., Hang, P., Song, L., Lin, D., Yang, L. ve Yang, D., 2022, Light soaking-induced performance enhancement in a-Si: H/c-Si heterojunction solar cells, *Science China Materials*, 1-5.

Hegedüs, M., Baláž, M., Tešinský, M., Sayagues, M. J., Siffalovic, P., Kruľaková, M., Kaňuchová, M., Briančin, J., Fabián, M. ve Baláž, P., 2018, Scalable synthesis of potential solar cell absorber Cu2SnS3 (CTS) from nanoprecursors, *Journal of Alloys and Compounds*, 768, 1006-1015.

Heidariramsheh, M., Gharabeiki, S., Mahdavi, S. M. ve Taghavinia, N., 2021, Optoelectrical and structural characterization of Cu2SnS3 thin films grown via spray pyrolysis using stable molecular ink, *Solar Energy*, 224, 218-229.

Hosseinpour, R., Izadifard, M. ve Ghazi, M., 2021, Study of Alkali (Na, K)-Doped Cu 2 ZnSnS 4 Thin Films Prepared by Sol–Gel Method, *Semiconductors*, 55 (2), 179-193.

Houimi, A., Yiğit Gezgin, S. ve Kılıç, H. Ş., Theoretical analysis of solar cell performance with different BSF layers utilizing experimental results of CdS films deposit by pulsed laser, *physica status solidi (a)*.

Houimi, A., Gezgin, S. Y., Mercimek, B. ve Kılıç, H. Ş., 2021, Numerical analysis of CZTS/n-Si solar cells using SCAPS-1D. A comparative study between experimental and calculated outputs, *Optical Materials*, 121, 111544.

Hsieh, Y. T., Han, Q., Jiang, C., Song, T. B., Chen, H., Meng, L., Zhou, H. ve Yang, Y., 2016, Efficiency enhancement of Cu2ZnSn (S, Se) 4 solar cells via alkali metals doping, *Advanced Energy Materials*, 6 (7), 1502386.

Huhtinen, H., Schlesier, K. ve Paturi, P., 2009, Growth and c-axis flux pinning of nanostructured YBCO/BZO multilayers, *Superconductor Science and Technology*, 22 (7), 075019.

Huhtinen, H., Irjala, M., Paturi, P. ve Falter, M., 2012, The effect of BZO doping concentration and thickness dependent properties of YBCO films grown by PLD on buffered NiW substrates, *Physica C: Superconductivity*, 472 (1), 66-74.

Ismail, R. A., Abeduljabbar, N. F. ve Fatehi, M. W., 2019a, Effect of dipping time on the properties of Sb2S3/Si heterojunction prepared by chemical bath deposition, *Materials Research Express*, 6 (4), 045915.

Ismail, R. A., Abeduljabbar, N. H. ve Fatehi, M., 2019b, Effect of dipping time on the properties of Sb 2 S 3/Si heterojunction prepared by chemical bath deposition, *Materials Research Express*.

Jackson, P., Hariskos, D., Wuerz, R., Wischmann, W. ve Powalla, M., 2014, Compositional investigation of potassium doped Cu (In, Ga) Se2 solar cells with

efficiencies up to 20.8%, *physica status solidi (RRL)–Rapid Research Letters*, 8 (3), 219-222.

Jackson, P., Wuerz, R., Hariskos, D., Lotter, E., Witte, W. ve Powalla, M., 2016, Effects of heavy alkali elements in Cu (In, Ga) Se2 solar cells with efficiencies up to 22.6%, *physica status solidi (RRL)–Rapid Research Letters*, 10 (8), 583-586.

Jiang, F., Shen, H., Wang, W. ve Zhang, L., 2011, Preparation and properties of Cu2ZnSnS4 absorber and Cu2ZnSnS4/amorphous silicon thin-film solar cell, *Applied Physics Express*, 4 (7), 074101.

Jing-Jing, M., Ke-Xin, J., Bing-Cheng, L., Fei, F., Hui, X., Chao-Chao, Z. ve Chang-Le, C., 2010, Rectifying and photovoltage properties of ZnO: A1/p-Si heterojunction, *Chinese Physics Letters*, 27 (10), 107304.

Jo, E., Kim, S. G., Gour, K. S., Jang, S., Jang, J. S. ve Kim, J. H., 2022, Improved Jsc by Increasing the Absorber Layer Thickness of Monoclinic-Dominated Cu2SnS3 Thin Film Solar Cells Fabricated on Flexible Mo Foil, *Solar RRL*, 6 (4), 2100743.

Joshi, M. P. ve Bhosale, P. N., 2019, Probing the role of deposition time in tuning the physico-chemical, optoelectronic performance of Cu2SnS3 thin films, *Materials Letters*, 255, 126526.

Joshi, M. P. ve Bhosale, P. N., 2021, Exploring the microstructural, optoelectronic properties of deposition time dependent Cu2Sn (S, Se) 3 thin film synthesized by non-vacuum arrested precipitation technique, *Superlattices and Microstructures*, 150, 106785.

Kanai, A., Araki, H., Takeuchi, A. ve Katagiri, H., 2015, Annealing temperature dependence of photovoltaic properties of solar cells containing Cu2SnS3 thin films produced by co-evaporation, *physica status solidi (b)*, 252 (6), 1239-1243.

Kanai, A. ve Sugiyama, M., 2021, Na induction effects for J–V properties of Cu2SnS3 (CTS) solar cells and fabrication of a CTS solar cell over-5.2% efficiency, *Solar Energy Materials and Solar Cells*, 231, 111315.

Katagiri, H., Sasaguchi, N., Hando, S., Hoshino, S., Ohashi, J. ve Yokota, T., 1997, Preparation and evaluation of Cu2ZnSnS4 thin films by sulfurization of E□ B evaporated precursors, *Solar Energy Materials and Solar Cells*, 49 (1-4), 407-414.

Katagiri, H., Jimbo, K., Yamada, S., Kamimura, T., Maw, W. S., Fukano, T., Ito, T. ve Motohiro, T., 2008, Enhanced conversion efficiencies of Cu2ZnSnS4-based thin film solar cells by using preferential etching technique, *Applied Physics Express*, 1 (4), 041201.

Kato, T., Wu, J.-L., Hirai, Y., Sugimoto, H. ve Bermudez, V., 2019, Record Efficiency for Thin-Film Polycrystalline Solar Cells Up to 22.9% Achieved by Cs-Treated Cu (In, Ga)(Se, S) 2, *IEEE Journal of Photovoltaics*, 9 (1), 325-330.

Kermadi, S., Sali, S., Zougar, L., Boumaour, M., Gunder, R., Schorr, S., Izquierdo-Roca, V. ve Pérez-Rodríguez, A., 2018, An in-depth investigation on the grain growth and the formation of secondary phases of ultrasonic-sprayed Cu2ZnSnS4 based thin films assisted by Na crystallization catalyst, *Solar Energy*, 176, 277-286.

Khatri, I., Matsuura, J., Sugiyama, M. ve Nakada, T., 2019, Effect of heat-bias soaking on cesium fluoride-treated CIGS thin film solar cells, *Progress in Photovoltaics: Research and Applications*.

Khattak, Y. H., Baig, F., Toura, H., Ullah, S., Marí, B., Beg, S. ve Ullah, H., 2018, Effect of CZTSe BSF and minority carrier life time on the efficiency enhancement of CZTS kesterite solar cell, *Current Applied Physics*, 18 (6), 633-641.

Khoshsirat, N., Yunus, N. A. M., Hamidon, M. N., Shafie, S. ve Amin, N., 2015, Analysis of absorber layer properties effect on CIGS solar cell performance using SCAPS, *Optik*, 126 (7-8), 681-686.

Kilmametov, A., Kulagin, R., Mazilkin, A., Seils, S., Boll, T., Heilmaier, M. ve Hahn, H., 2019, High-pressure torsion driven mechanical alloying of CoCrFeMnNi high entropy alloy, *Scripta Materialia*, 158, 29-33.

Kim, I. Y., Lee, J. Y., Ghorpade, U. V., Suryawanshi, M., Lee, D. S. ve Kim, J. H., 2016a, Influence of annealing temperature on the properties and solar cell performance of Cu2SnS3 (CTS) thin film prepared using sputtering method, *Journal of Alloys and Compounds*, 688, 12-17.

Kim, J.-S., Kang, J.-K. ve Hwang, D.-K., 2016b, High efficiency bifacial Cu2ZnSnSe4 thin-film solar cells on transparent conducting oxide glass substrates, *APL Materials*, 4 (9), 096101.

Kim, Y., Choi, I.-H. ve Park, S. Y., 2018, Characterization of Cu2SnS3 thin films prepared by sulfurization of co-evaporated Cu–SnS precursor layers, *Thin Solid Films*, 666, 61-65.

Kobayashi, T., Jimbo, K., Tsuchida, K., Shinoda, S., Oyanagi, T. ve Katagiri, H., 2005, Investigation of Cu2ZnSnS4-based thin film solar cells using abundant materials, *Japanese journal of applied physics*, 44 (1S), 783.

Kodalle, T., Heinemann, M. D., Greiner, D., Yetkin, H. A., Klupsch, M., Li, C., van Aken, P. A., Lauermann, I., Schlatmann, R. ve Kaufmann, C. A., 2018, Elucidating the mechanism of an RbF post deposition treatment in CIGS thin film solar cells, *Solar RRL*, 2 (9), 1800156.

Koike, J., Chino, K., Aihara, N., Araki, H., Nakamura, R., Jimbo, K. ve Katagiri, H., 2012, Cu2SnS3 thin-film solar cells from electroplated precursors, *Japanese journal of applied physics*, 51 (10S), 10NC34.

Kozawa, T., Fukuyama, K., Kushimoto, K., Ishihara, S., Kano, J., Kondo, A. ve Naito, M., 2021, Effect of ball collision direction on a wet mechanochemical reaction, *Scientific reports*, 11 (1), 1-8.

Kronik, L., Cahen, D. ve Schock, H. W., 1998, Effects of sodium on polycrystalline Cu (In, Ga) Se2 and its solar cell performance, *Advanced Materials*, 10 (1), 31-36.

Kuku, T. A. ve Fakolujo, O. A., 1987, Photovoltaic characteristics of thin films of Cu2SnS3, *Solar energy materials*, 16 (1-3), 199-204.

Kumar, M., Kanjilal, A. ve Som, T., 2013, Effect of grain-boundaries on electrical properties of n-ZnO: Al/p-Si heterojunction diodes, *AIP Advances*, 3 (9), 092126.

Kumar, M., Dubey, A., Adhikari, N., Venkatesan, S. ve Qiao, Q., 2015, Strategic review of secondary phases, defects and defect-complexes in kesterite CZTS–Se solar cells, *Energy & Environmental Science*, 8 (11), 3134-3159.

Laemmle, A., Wuerz, R. ve Powalla, M., 2015, Investigation of the effect of potassium on Cu (In, Ga) Se2 layers and solar cells, *Thin Solid Films*, 582, 27-30.

Lany, S. ve Zunger, A., 2005, Anion vacancies as a source of persistent photoconductivity in II-VI and chalcopyrite semiconductors, *Physical Review B*, 72 (3), 035215.

Lee, E., Cho, J. W., Kim, J., Yun, J., Kim, J. H. ve Min, B. K., 2010, Synthesis of CIGS powders: transition from binary to quaternary crystalline structure, *Journal of Alloys and Compounds*, 506 (2), 969-972.

Lee, J. Y., Kim, I. Y., Surywanshi, M. P., Ghorpade, U. V., Lee, D. S. ve Kim, J. H., 2017, Fabrication of Cu2SnS3 thin film solar cells using Cu/Sn layered metallic precursors prepared by a sputtering process, *Solar Energy*, 145, 27-32.

Li, W., Su, Z., Tan, J. M. R., Chiam, S. Y., Seng, H. L., Magdassi, S. ve Wong, L. H., 2017, Revealing the Role of Potassium Treatment in CZTSSe Thin Film Solar Cells, *Chemistry of Materials*, 29 (10), 4273-4281.

Lohani, K., Isotta, E., Ataollahi, N., Fanciulli, C., Chiappini, A. ve Scardi, P., 2020a, Ultra-low thermal conductivity and improved thermoelectric performance in disordered nanostructured copper tin sulphide (Cu2SnS3, CTS), *Journal of Alloys and Compounds*, 830, 154604.

Lohani, K., Nautiyal, H., Ataollahi, N., Fanciulli, C., Sergueev, I., Etter, M. ve Scardi, P., 2020b, Experimental and Ab initio study of Cu2SnS3 (CTS) polymorphs for thermoelectric applications, *The Journal of Physical Chemistry C*, 125 (1), 178-188.

Lokhande, A., Chalapathy, R., He, M., Jo, E., Gang, M., Pawar, S., Lokhande, C. ve Kim, J. H., 2016a, Development of Cu2SnS3 (CTS) thin film solar cells by physical techniques: A status review, *Solar Energy Materials and Solar Cells*, 153, 84-107.

Lokhande, A., Gurav, K., Jo, E., Lokhande, C. ve Kim, J. H., 2016b, Chemical synthesis of Cu2SnS3 (CTS) nanoparticles: A status review, *Journal of Alloys and Compounds*, 656, 295-310.

M Hashem, H., 2016, Performance of transparent conducting fluorine-doped tin oxide films for applications in energy efficient devices, *International Journal of Thin Film Science and Technology*, 5 (1), 9.

Magdy, W., Kanai, A., Abdel-Latif, M. S., Mahmoud, F. A., El Shenawy, E. T., Khairy, S. A., Hassan, H. H. ve Sugiyama, M., 2021, Impact of Na and/or Sb on the CTS thin films and solar cell performance, *Japanese journal of applied physics*, 60 (10), 105506.

Marzougi, M., Rabeh, M. B. ve Kanzari, M., 2019, Effect of Na doping on structural and optical properties in Cu2ZnSnS4 thin films synthesized by thermal evaporation method, *Thin Solid Films*, 672, 41-46.

Masson-Delmotte, V., Zhai, P., Pirani, A., Connors, S. L., Péan, C., Berger, S., Caud, N., Chen, Y., Goldfarb, L. ve Gomis, M., 2021, Climate change 2021: the physical science basis, *Contribution of working group I to the sixth assessment report of the intergovernmental panel on climate change*, 2.

Miyata, Y., Nakamura, S. ve Akaki, Y., 2015, Effects of H2S annealing on Cu-Sn-S thin films prepared from vacuum-evaporated Cu-Sn precursor, *physica status solidi (c)*, 12 (6), 765-768.

Mohamed, A., Afify, R., Omar, W. A., Okonkwo, P. C. ve Boshta, M., 2020, Influence of deposition temperature and time on the optical behavior of sprayed Cu2SnS3 thin films, *Emergent Materials*, 3 (1), 15-24.

Moholkar, A., Shinde, S., Babar, A., Sim, K.-U., Kwon, Y.-b., Rajpure, K., Patil, P., Bhosale, C. ve Kim, J., 2011, Development of CZTS thin films solar cells by pulsed laser deposition: influence of pulse repetition rate, *Solar Energy*, 85 (7), 1354-1363.

Moon, S. H., Park, S. J., Hwang, Y. J., Lee, D.-K., Cho, Y., Kim, D.-W. ve Min, B. K., 2014, Printable, wide band-gap chalcopyrite thin films for power generating window applications, *Scientific reports*, 4 (1), 1-6.

Mule, A., Vermang, B., Sylvester, M., Brammertz, G., Ranjbar, S., Schnabel, T., Gampa, N., Meuris, M. ve Poortmans, J., 2017, Effect of different alkali (Li, Na, K, Rb, Cs) metals on Cu2ZnSnSe4 solar cells, *Thin Solid Films*, 633, 156-161.

Mustafa, F. A., 2013, Optical properties of NaI doped polyvinyl alcohol films, *Physical Sciences Research International*, 1 (1), 1-9.

Nakashima, M., Fujimoto, J., Yamaguchi, T. ve Izaki, M., 2015a, Cu2SnS3 thin-film solar cells fabricated by sulfurization from NaF/Cu/Sn stacked precursor, *Applied Physics Express*, 8 (4), 042303.

Nakashima, M., Yamaguchi, T., Itani, H., Sasano, J. ve Izaki, M., 2015b, Cu2SnS3 thin film solar cells prepared by thermal crystallization of evaporated Cu/Sn precursors in sulfur and tin atmosphere, *physica status solidi (c)*, 12 (6), 761-764.

Nakashima, M., Fujimoto, J., Yamaguchi, T., Sasano, J. ve Izaki, M., 2017, KF addition to Cu2SnS3 thin films prepared by sulfurization process, *Japanese journal of applied physics*, 56 (4S), 04CS02.

Nakata, S., Maeda, T. ve Wada, T., 2019, Crystallographic and Optical Properties of (Cu1− xLix) 2SnS3 Photovoltaic Semiconductor, *physica status solidi (a)*, 216 (15), 1800889.

Nasir, E. ve Abass, M., 2016, Characterization, Morphology and Electrical Properties of Chemically Deposited Nanocrystalline PbS/Si Heterojunction Thin Films, *Chalcogenide Letters*, 13 (6), 271-279.

Neamţu, B., Chicinaş, H., Marinca, T., Isnard, O., Pană, O. ve Chicinaş, I., 2016, Amorphisation of Fe-based alloy via wet mechanical alloying assisted by PCA decomposition, *Materials Chemistry and Physics*, 183, 83-92.

Nelson, J. A., 2003, The physics of solar cells, World Scientific Publishing Company, p.

Neves, F., Correia, J., Hanada, K., Santos, L., Gunder, R. ve Schorr, S., 2016, Structural characterization of Cu2SnS3 and Cu2 (Sn, Ge) S3 compounds, *Journal of Alloys and Compounds*, 682, 489-494.

Niles, D. W., Al-Jassim, M. ve Ramanathan, K., 1999, Direct observation of Na and O impurities at grain surfaces of CuInSe 2 thin films, *Journal of Vacuum Science & Technology A: Vacuum, Surfaces, and Films*, 17 (1), 291-296.

Nishihara, H., Maeda, T., Shigemi, A. ve Wada, T., 2017, First-principles study of defect formation in the photovoltaic semiconductors Cu2GeS3 and Cu2ZnGeS4 for comparison with Cu2SnS3, Cu2ZnSnS4, and CuInSe2, *Japanese journal of applied physics*, 56 (4S), 04CS08.

Nomura, T., Maeda, T. ve Wada, T., 2013, Preparation of narrow band-gap Cu2Sn (S, Se) 3 and fabrication of film by non-vacuum process, *Japanese journal of applied physics*, 52 (4S), 04CR08.

Nouri, A. ve Wen, C., 2014, Surfactants in mechanical alloying/milling: a catch-22 situation, *Critical reviews in solid state and materials sciences*, 39 (2), 81-108.

Ojeda-Durán, E., Monfil-Leyva, K., Andrade-Arvizu, J., Becerril-Romero, I., Sánchez, Y., Fonoll-Rubio, R., Guc, M., Jehl, Z., Luna-López, J. ve Muñoz-Zurita, A., 2020, CZTS solar cells and the possibility of increasing VOC using evaporated Al2O3 at the CZTS/CdS interface, *Solar Energy*, 198, 696-703.

Okada, K., Kikuchi, S., Ban, T. ve Ōtsuka, N., 1992, Difference of mechanochemical factors for Al2O3 powders upon dry and wet grinding, *Journal of materials science letters*, 11 (12), 862-864.

Orlianges, J., Champeaux, C., Catherinot, A., Merle, T. ve Angleraud, B., 2004, Pulsed laser deposition of tetrahedral amorphous carbon films from glassy carbon and graphite targets: a comparative study, *Thin Solid Films*, 453, 285-290.

Orlianges, J.-C., 2003, Optimisation du dépôt par ablation laser de films minces d'alumine et de carbone tétraédrique amorphe pure et dopé; propriétés des couches et intégration dans le fabrication de composants MEMS RF, *Université de Limoges*.

Ozsoy, E. K., Atay, F. ve Buyukgungor, O., 2021, Production and characterization of Cu2SnS3 films for solar cell applications: The effect of the sulfurization temperature on CuS secondary phase, *Solar Energy*, 214, 179-188.

Pallavolu, M. R., Reddy, V. R. M., Pejjai, B., Jeong, D.-s. ve Park, C., 2018, Effect of sulfurization temperature on the phase purity of Cu2SnS3 thin films deposited via high vacuum sulfurization, *Applied Surface Science*, 462, 641-648.

Patel, B., Waldiya, M. ve Ray, A., 2018, Highly phase-pure spray-pyrolysed Cu2SnS3 thin films prepared by hybrid thermal treatment for photovoltaic applications, *Journal of Alloys and Compounds*, 745, 347-354.

Patil, S. S., Mane, R. M., Mali, S. S., Hong, C. K. ve Bhosale, P. N., 2020, Facile designing and assessment of photovoltaic performance of hydrothermally grown kesterite Cu2ZnSnS4 thin films: influence of deposition time, *Solar Energy*, 201, 102-115.

Peurla, M., Huhtinen, H., Tse, Y., Raittila, J. ve Paturi, P., 2007, Structural properties of YBCO thin films deposited from different kinds of targets, *IEEE transactions on applied superconductivity*, 17 (2), 3608-3611.

Prabhakar, T. ve Jampana, N., 2011, Effect of sodium diffusion on the structural and electrical properties of Cu2ZnSnS4 thin films, *Solar Energy Materials and Solar Cells*, 95 (3), 1001-1004.

Prabhu, Y., Rao, K. V., Kumari, B. S., Kumar, V. S. S. ve Pavani, T., 2015, Synthesis of Fe 3 O 4 nanoparticles and its antibacterial application, *International Nano Letters*, 5 (2), 85-92.

Raadik, T., Grossberg, M., Krustok, J., Kauk-Kuusik, M., Crovetto, A., Bolt Ettlinger, R., Hansen, O. ve Schou, J., 2017, Temperature dependent photoreflectance study of Cu2SnS3 thin films produced by pulsed laser deposition, *Applied Physics Letters*, 110 (26), 261105.

Rajesh, G., Muthukumarasamy, N., Subramaniam, E., Agilan, S. ve Velauthapillai, D., 2013, Synthesis of Cu2ZnSnS4 thin films by dip-coating method without sulphurization, *Journal of sol-gel science and technology*, 66 (2), 288-292.

Rajeswari, R., Venugopal, D., Raj, A. D., Arumugam, J., Sundaram, S. J. ve Kaviyarasu, K., 2021, Effect of doping concentration for the properties of Fe doped TiO2 thin films applications, *Materials Today: Proceedings*, 36, 468-474.

Reddy, G. P. ve Reddy, K. R., 2017, Preparation and characterization of Cu2SnS3 thin films by two stage process for solar cell application, *Materials Today: Proceedings*, 4 (13), 12401-12406.

Reddy, T. ve KUMAR, M. S., 2019, FABRICATION OF VISIBLE LIGHT PHOTODETECTOR USING CO-EVAPORAED Cu 2 SnS 3 THIN FILMS, *Journal of Ovonic Research*, 15 (6).

Reddy, T. S., Amiruddin, R. ve Kumar, M. S., 2015, Deposition and characterization of Cu2SnS3 thin films by co-evaporation for photovoltaic application, *Solar Energy Materials and Solar Cells*, 143, 128-134.

Reddy, V. R. M., Pallavolu, M. R., Guddeti, P. R., Gedi, S., Reddy, K. K. Y. B., Pejjai, B., Kim, W. K., Kotte, T. R. R. ve Park, C., 2019, Review on Cu2SnS3, Cu3SnS4, and Cu4SnS4 thin films and their photovoltaic performance, *Journal of Industrial and Engineering Chemistry*, 76, 39-74.

Reed, J. S., 1995, Principles of ceramics processing.

Regulacio, M. D., Ye, C., Lim, S. H., Bosman, M., Ye, E., Chen, S., Xu, Q. H. ve Han, M. Y., 2012, Colloidal nanocrystals of Wurtzite-type Cu2ZnSnS4: facile noninjection synthesis and formation mechanism, *Chemistry–A European Journal*, 18 (11), 3127-3131.

Rehan, S., Moon, J., Kim, T. G., Gwak, J., Kim, J., Kim, J. W., Jo, W., Ahn, S. K. ve Ahn, S., 2018, Role of Na in solution-processed CuInSe2 (CISe) devices: A different story for improving efficiency, *Nano Energy*, 48, 401-412.

Robles, V., Trigo, J., Guillén, C. ve Herrero, J., 2015, Copper tin sulfide (CTS) absorber thin films obtained by co-evaporation: Influence of the ratio Cu/Sn, *Journal of Alloys and Compounds*, 642, 40-44.

Roselin, A. A., Anandhan, N., Gopu, G., Doss, I. J. P., Ganesan, K., Selvam, R. P., Marimuthu, T. ve Sivakumar, G., 2019, Electrochemical sensor for the detection of lead ions of B-site-doped bismuth titanate perovskite thin film, *Applied Physics A*, 125 (9), 1-15.

Salome, P. M., Hultqvist, A., Fjällström, V., Edoff, M., Aitken, B., Zhang, K., Fuller, K. ve Williams, C. K., 2014, Incorporation of Na in Cu (In, Ga) Se $ _ {\bf 2} $ Thin-Film Solar Cells: A Statistical Comparison Between Na From Soda-Lime Glass and From a Precursor Layer of NaF, *IEEE Journal of Photovoltaics*, 4 (6), 1659-1664.

Salomé, P. M., Hultqvist, A., Fjällström, V., Edoff, M., Aitken, B., Vaidyanathan, K., Zhang, K., Fuller, K. ve Williams, C. K., 2013, Cu (In, Ga) Se $ _ {\bf 2} $ Solar Cells With Varying Na Content Prepared on Nominally Alkali-Free Glass Substrates, *IEEE Journal of Photovoltaics*, 3 (2), 852-858.

Sanchez, H., Esparza, D., Lopez-Luke, T., Castañeda-Contreras, J., Marañon-Ruiz, V., Zarazúa, I. ve Rodriguez, R., 2020, Effect of Al3+ doping concentration and film thickness of ZnO nanoparticles over the TiO2 photoelectrode in CdS quantum dots sensitized solar cells, *Solar Energy*, 197, 154-162.

Sasagawa, S., Nishida, G., Takeuchi, A., Katagiri, H. ve Araki, H., 2018, Effect of sodium addition on Cu2SnS3 thin-film solar cells fabricated on alkali-free glass substrates, *Japanese journal of applied physics*, 57 (8S3), 08RC11.

Schou, J., Gansukh, M., Ettlinger, R. B., Cazzaniga, A., Grossberg, M., Kauk-Kuusik, M. ve Canulescu, S., 2018, Pulsed laser deposition of chalcogenide sulfides from multi-and single-component targets: the non-stoichiometric material transfer, *Applied Physics A*, 124 (1), 78.

Schroeder, D. J. ve Rockett, A. A., 1997, Electronic effects of sodium in epitaxial CuIn 1− x Ga x Se 2, *Journal of applied physics*, 82 (10), 4982-4985.

Schurr, R., Hölzing, A., Jost, S., Hock, R., Voβ, T., Schulze, J., Kirbs, A., Ennaoui, A., Lux-Steiner, M. ve Weber, A., 2009, The crystallisation of Cu2ZnSnS4 thin film solar cell absorbers from co-electroplated Cu–Zn–Sn precursors, *Thin Solid Films*, 517 (7), 2465-2468.

Shaftel, H., 2022, Climate Change: Vital Signs of the Planet - NASA, California Institute of Technology https://climate.nasa.gov/:

Sharma, K., Williams, B., Mittal, A., Knoops, H., Kniknie, B., Bakker, N., Kessels, W., Schropp, R. ve Creatore, M., 2014, Expanding thermal plasma chemical vapour deposition of ZnO: Al layers for CIGS solar cells, *International Journal of Photoenergy*, 2014.

Shelke, H. D., Lokhande, A. C., Raut, V. S., Patil, A. M., Kim, J. H. ve Lokhande, C. D., 2017, Facile synthesis of Cu2SnS3 thin films grown by SILAR method: effect of film thickness, *Journal of Materials Science: Materials in Electronics*, 28 (11), 7912-7921.

Shelke, H. D., Lokhande, A. C., Kim, J. H. ve Lokhande, C. D., 2020, Influence of deposition temperature on the structural, morphological, optical and photoelectrochemical properties of CBD deposited Cu2SnS3 thin films, *Journal of Alloys and Compounds*, 831, 154768.

Shen, Y., Li, C., Huang, R., Tian, R., Ye, Y., Pan, L., Koumoto, K., Zhang, R., Wan, C. ve Wang, Y., 2016, Eco-friendly p-type Cu2SnS3 thermoelectric material: crystal structure and transport properties, *Scientific reports*, 6 (1), 1-8.

Sheng, X., Wang, L., Tian, Y., Luo, Y., Chang, L. ve Yang, D., 2013, Low-cost fabrication of Cu 2 ZnSnS 4 thin films for solar cell absorber layers, *Journal of Materials Science: Materials in Electronics*, 24 (2), 548-552.

Sheng, Y., Deng, T., Qiu, P., Shi, X., Xi, J., Han, Y. ve Yang, J., 2021, Accelerating the Discovery of Cu–Sn–S Thermoelectric Compounds via High-Throughput Synthesis, Characterization, and Machine Learning-Assisted Image Analysis, *Chemistry of Materials*, 33 (17), 6918-6924.

Shin, B., Gunawan, O., Zhu, Y., Bojarczuk, N. A., Chey, S. J. ve Guha, S., 2013, Thin film solar cell with 8.4% power conversion efficiency using an earth-abundant Cu2ZnSnS4 absorber, *Progress in Photovoltaics: Research and Applications*, 21 (1), 72-76.

Shin, D., Lee, S., Kim, D. R., Park, J. H., Kim, Y., Choi, W.-J., Son, C. S., Son, Y. G. ve Hwang, D., 2020, Effect of RF Power on the Properties of Sputtered-CuS Thin Films for Photovoltaic Applications, *Energies*, 13 (3), 688.

Shin, Y. M., Shin, D. H., Kim, J. H. ve Ahn, B. T., 2011, Effect of Na doping using Na2S on the structure and photovoltaic properties of CIGS solar cells, *Current Applied Physics*, 11 (1), S59-S64.

Singh, O. P., Gour, K. S., Parmar, R. ve Singh, V. N., 2016, Sodium induced grain growth, defect passivation and enhancement in the photovoltaic properties of Cu2ZnSnS4 thin film solar cell, *Materials Chemistry and Physics*, 177, 293-298.

Smith, H. M. ve Turner, A., 1965, Vacuum deposited thin films using a ruby laser, *Applied optics*, 4 (1), 147-148.

Su, Z., Yan, C., Sun, K., Han, Z., Liu, F., Liu, J., Lai, Y., Li, J. ve Liu, Y., 2012, Preparation of Cu2ZnSnS4 thin films by sulfurizing stacked precursor thin films via successive ionic layer adsorption and reaction method, *Applied Surface Science*, 258 (19), 7678-7682.

Sun, X., Jiang, F. ve Feng, J., 2009, Roles of sodium induced defects in CuInSe2 by first principles calculation, *Computational Materials Science*, 47 (1), 31-34.

Suryanarayana, C., 2001, Mechanical alloying and milling, *Progress in materials science*, 46 (1-2), 1-184.

Suryanarayana, C., Ivanov, E. ve Boldyrev, V., 2001, The science and technology of mechanical alloying, *Materials Science and Engineering: A*, 304, 151-158.

Suryanarayana, C., 2008, Recent developments in mechanical alloying, *Rev. Adv. Mater. Sci*, 18 (3), 203-211.

Suryanarayana, C., 2019, Mechanical alloying: a novel technique to synthesize advanced materials, *Research*, 2019.

Suryawanshi, M., Agawane, G., Bhosale, S., Shin, S. W., Patil, P., Kim, J.-H. ve Moholkar, A., 2013, CZTS based thin film solar cells: a status review, *Materials Technology*, 28 (1-2), 98-109.

Suryawanshi, P., Babar, B., Mohite, A., Pawar, U., Bhosale, A. ve Shelke, H., 2021, A simple chemical approach for the deposition of Cu2SnS3 (CTS) thin films, *Materials Today: Proceedings*, 43, 2682-2688.

Swartz, C., LeBlanc, E., Perkins, C., McGott, D., Reese, M., Nichols, A. ve Myers, T., 2022, Evaluation of PbTe and SnTe as ohmic contact layers in CdTe solar cell devices, *Applied Surface Science*, 153656.

Sze, S. M., 2008, Semiconductor devices: physics and technology, John wiley & sons, p.

Tan, X., Zhang, D., Li, Z., Liu, G. ve Fan, R., 2007, Ionization effect to plasma expansion study during nanosecond pulsed laser deposition, *Physics Letters A*, 370 (1), 64-69.

Tanaka, K., Maeda, T. ve Araki, H., 2020, Photoluminescence observation of the effects of Cu/Sn ratio and Na addition on Cu2SnS3, *Solar Energy*, 199, 143-151.

Tang, D., Wang, Q., Liu, F., Zhao, L., Han, Z., Sun, K., Lai, Y., Li, J. ve Liu, Y., 2013, An alternative route towards low-cost Cu2ZnSnS4 thin film solar cells, *Surface and Coatings Technology*, 232, 53-59.

Thota, N., Kumar, M., Vishwakarma, M. ve Mehta, B., 2019, Structural, electronic and optical properties of pulsed laser deposited Cu2SnS3 photo absorber thin films: A combined experimental and computational study, *Thin Solid Films*, 677, 62-67.

Tiwari, D., Koehler, T., Klenk, R. ve Fermin, D. J., 2017, Solution processed single-phase Cu 2 SnS 3 films: structure and photovoltaic performance, *Sustainable Energy & Fuels*, 1 (4), 899-906.

Tong, J., Wang, S., Wang, G., Liu, Y., Wang, Y., Chen, L., Wang, L., Pan, D., Zhang, X. ve Liu, Y., 2021, Li+ &Ag+ and Li+ &Cd2+ double-ion-doping strategy to improve the efficiency of Cu2ZnSn (S, Se) 4 solar cells, *Solar Energy*, 220, 882-889.

Tong, Z., Yan, C., Su, Z., Zeng, F., Yang, J., Li, Y., Jiang, L., Lai, Y. ve Liu, F., 2014, Effects of potassium doping on solution processed kesterite Cu2ZnSnS4 thin film solar cells, *Applied Physics Letters*, 105 (22), 223903.

Ullah, M., Ali, M. ve Hamid, S. B. A., 2014, SURFACTANT-ASSISTED BALL MILLING: A NOVEL ROUTE TO NOVEL MATERIALS WITH CONTROLLED NANOSTRUCTURE-A REVIEW, *Reviews on Advanced Materials Science*, 37.

Umehara, M., Takeda, Y., Motohiro, T., Sakai, T., Awano, H. ve Maekawa, R., 2013, Cu2Sn1-xGexS3 (x= 0.17) thin-film solar cells with high conversion efficiency of 6.0%, *Applied Physics Express*, 6 (4), 045501.

Vaidya, M., Muralikrishna, G. M. ve Murty, B. S., 2019, High-entropy alloys by mechanical alloying: A review, *Journal of Materials Research*, 34 (5), 664-686.

Vanalakar, S., Agawane, G., Kamble, A., Hong, C., Patil, P. ve Kim, J., 2015a, Fabrication of Cu2SnS3 thin film solar cells using pulsed laser deposition technique, *Solar Energy Materials and Solar Cells*, 138, 1-8.

Vanalakar, S., Agawane, G., Shin, S., Suryawanshi, M., Gurav, K., Jeon, K., Patil, P., Jeong, C., Kim, J. ve Kim, J., 2015b, A review on pulsed laser deposited CZTS thin films for solar cell applications, *Journal of Alloys and Compounds*, 619, 109-121.

Vanalakar, S., Agawane, G., Shin, S., Yang, H., Patil, P., Kim, J. ve Kim, J., 2015c, Non-vacuum mechanochemical route to the synthesis of Cu2SnS3 nano-ink for solar cell applications, *Acta Materialia*, 85, 314-321.

Voevodin, A. ve Donley, M., 1996, Preparation of amorphous diamond-like carbon by pulsed laser deposition: a critical review, *Surface and Coatings Technology*, 82 (3), 199-213.

Wang, P., Li, Y. ve Lu, Y., 2011, Enhanced piezoelectric properties of (Ba0. 85Ca0. 15)(Ti0. 9Zr0. 1) O3 lead-free ceramics by optimizing calcination and sintering temperature, *Journal of the European Ceramic Society*, 31 (11), 2005-2012.

Wang, W., Winkler, M. T., Gunawan, O., Gokmen, T., Todorov, T. K., Zhu, Y. ve Mitzi, D. B., 2014, Device characteristics of CZTSSe thin-film solar cells with 12.6% efficiency, *Advanced Energy Materials*, 4 (7), 1301465.

Wang, Y., Li, J., Xue, C., Zhang, Y., Jiang, G., Liu, W. ve Zhu, C., 2016, Investigation of the sulfurization process of Cu2SnS3 thin films with stacked layers CBD-Cu/SnS by rapid thermal process, *Materials Letters*, 178, 104-106.

Wang, Y., Li, J., Xue, C., Zhang, Y., Jiang, G., Liu, W. ve Zhu, C., 2017, Fabrication of Cu 2 SnS 3 thin-film solar cells with oxide precursor by pulsed laser deposition, *Journal of materials science*, 52 (11), 6225-6234.

Wang, Y., Lv, S. ve Li, Z., 2022, Review on incorporation of alkali elements and their effects in Cu (In, Ga) Se2 solar cells, *Journal of Materials Science & Technology*, 96, 179-189.

Wang, Z., Brodusch, N., Gauvin, R. ve Demopoulos, G. P., 2018, Lithium-doped Cu2ZnSnS4 superstrate solar cells with 5% efficiency–An alternative to thin film kesterite photovoltaics, *Nano Energy*, 53, 130-134.

Wei, S.-H., Zhang, S. ve Zunger, A., 1999, Effects of Na on the electrical and structural properties of CuInSe 2, *Journal of applied physics*, 85 (10), 7214-7218.

Wei-Ying, Z., Sheng, Z., Li-Jie, S. ve Zhu-Xi, F., 2008, Dependence of photovoltaic property of ZnO/Si heterojunction solar cell on thickness of ZnO films, *Chinese Physics Letters*, 25 (5), 1829.

Wen, Q., Li, Y., Yan, J. ve Wang, C., 2015, Crystal size-controlled growth of Cu2ZnSnS4 films by optimizing the Na doping concentration, *Materials Letters*, 140, 16-19.

Werner, B. ve Zdanowicz, T., 2007, Experimental determination of physical parameters in CIGS solar cells, *2007 International Students and Young Scientists Workshop on Photonics and Microsystems*, 84-86.

Werner, M., Sutter-Fella, C. M., Romanyuk, Y. E. ve Tiwari, A. N., 2015, 8.3% efficient Cu2ZnSn (S, Se) 4 solar cells processed from sodium-containing solution precursors in a closed reactor, *Thin Solid Films*, 582, 308-312.

Willmott, P. ve Huber, J., 2000, Pulsed laser vaporization and deposition, *Reviews of Modern Physics*, 72 (1), 315.

Wu, C., Hu, Z., Wang, C., Sheng, H., Yang, J. ve Xie, Y., 2007, Hexagonal Cu 2 Sn S 3 with metallic character: Another category of conducting sulfides, *Applied Physics Letters*, 91 (14), 143104.

Wubet, W. ve Kuo, D.-H., 2015, Structural and electrical properties of Si-and Ti-doped Cu2SnSe3 bulks, *Journal of Solid State Chemistry*, 227, 239-246.

Würfel, P. ve Würfel, U., 2016, Physics of solar cells: from basic principles to advanced concepts, John Wiley & Sons, p.

Xiao, W., Wang, J., Zhao, X., Wang, J., Huang, G., Cheng, L., Jiang, L. ve Wang, L., 2015, Intrinsic defects and Na doping in Cu2ZnSnS4: A density-functional theory study, *Solar Energy*, 116, 125-132.

Xin, H., Vorpahl, S., Collord, A., Braly, I., Uhl, A., Krueger, B., Ginger, D. ve Hillhouse, H., 2015, Lithium-doping inverts the nanoscale electric field at the grain boundaries in Cu 2 ZnSn (S, Se) 4 and increases photovoltaic efficiency, *Physical Chemistry Chemical Physics*, 17 (37), 23859-23866.

Xu, X., Wang, S., Ma, X., Yang, M., Lu, Y., Yang, S. ve Tang, Z., 2018, Effects of different precursors on Cu2SnS3 thin film solar cells prepared by sputtering method, *Vacuum*, 157, 223-228.

Xue, H., Lu, W., Tang, F., Li, X., Zhang, Y. ve Feng, Y., 2014, Phase diagram of the CulnSe2-CuGaSe2 pseudobinary system studied by combined ab initio density functional theory and thermodynamic calculation, *Journal of applied physics*, 116 (5), 053512.

Yadav, R. J., 2018, Complex oxides for dielectric resonator applications.

Yang, G., Li, X., Ji, X., Xu, X., Wang, A., Huang, J., Zhu, Y., Pan, G. ve Cui, S., 2020, Phase composition of the earth-abundant Cu2SnS3 thin films with different annealing temperature and its effects on the performance of the related solar cells, *Solar Energy*, 208, 206-211.

Yang, H., Luo, H., Wang, H., Usov, I., Suvorova, N., Jain, M., Feldmann, D., Dowden, P., DePaula, R. ve Jia, Q., 2008, Rectifying current-voltage characteristics of Bi Fe O 3⁄ Nb-doped Sr Ti O 3 heterojunction, *Applied Physics Letters*, 92 (10), 102113.

Yang, J., Lim, E. L., Tan, L. ve Wei, Z., 2022, Ink Engineering in Blade-Coating Large-Area Perovskite Solar Cells, *Advanced Energy Materials*, 2200975.

Yang, W.-C., Miskin, C. K., Hages, C. J., Hanley, E. C., Handwerker, C., Stach, E. A. ve Agrawal, R., 2014, Kesterite Cu2ZnSn (S, Se) 4 absorbers converted from metastable, wurtzite-derived Cu2ZnSnS4 nanoparticles, *Chemistry of Materials*, 26 (11), 3530-3534.

Yang, Y., Kang, X., Huang, L. ve Pan, D., 2016, Tuning the band gap of Cu2ZnSn (S, Se) 4 thin films via lithium alloying, *ACS applied materials & interfaces*, 8 (8), 5308-5313.

Yuan, Z. K., Chen, S., Xie, Y., Park, J. S., Xiang, H., Gong, X. G. ve Wei, S. H., 2016, Na-diffusion enhanced p-type conductivity in Cu (In, Ga) Se2: A new mechanism for efficient doping in semiconductors, *Advanced Energy Materials*, 6 (24), 1601191.

Yun, J. H., Kim, K. H., Kim, M. S., Ahn, B. T., Ahn, S. J., Lee, J. C. ve Yoon, K. H., 2007, Fabrication of CIGS solar cells with a Na-doped Molayer on a Na-free substrate, *Thin Solid Films*, 515 (15), 5876-5879.

Zaki, S. A., Abd-Elrahman, M., Abu-Sehly, A., Shaalan, N. ve Hafiz, M., 2020, Solar cell fabrication from semiconducting Cu3SbS3 on n-Si: Parameters evolution, *Materials Science in Semiconductor Processing*, 115, 105123.

Zawadzki, P., Baranowski, L. L., Peng, H., Toberer, E. S., Ginley, D. S., Tumas, W., Zakutayev, A. ve Lany, S., 2013, Evaluation of photovoltaic materials within the Cu-Sn-S family, *Applied Physics Letters*, 103 (25), 253902.

Zhai, Y.-T., Chen, S., Yang, J.-H., Xiang, H.-J., Gong, X.-G., Walsh, A., Kang, J. ve Wei, S.-H., 2011, Structural diversity and electronic properties of Cu 2 Sn X 3 (X= S, Se): A first-principles investigation, *Physical Review B*, 84 (7), 075213.

Zhang, J. ve Shao, L., 2009, Cu2ZnSnS4 thin films prepared by sulfurizing different multilayer metal precursors, *Science in China Series E: Technological Sciences*, 52 (1), 269-272.

Zhang, Q., Deng, H., Yu, J., Xu, B., Tao, J., Yang, P., Sun, L. ve Chu, J., 2018, Effect of sulfurization temperature of solution-processed Cu 2 SnS 3 absorber for low cost photovoltaic cells, *Materials Letters*, 228, 447-449.

Zhang, S., Wei, S.-H., Zunger, A. ve Katayama-Yoshida, H., 1998, Defect physics of the CuInSe 2 chalcopyrite semiconductor, *Physical Review B*, 57 (16), 9642.

Zhang, Y., Tse, K., Xiao, X. ve Zhu, J., 2017, Controlling defects and secondary phases of CZTS by surfactant potassium, *Physical Review Materials*, 1 (4), 045403.

Zhang, Y., Zhuang, Y., Liu, L., Qiu, P., Su, L., Teng, X., Fu, G. ve Yu, W., 2020, The microstructure evolution during MoS2 films growth and its influence on the MoS2 optical-electrical properties in MoS2/p-Si heterojunction solar cells, *Superlattices and Microstructures*, 137, 106352.

Zhao, P. ve Cheng, S., 2013, Influence of sulfurization temperature on photoelectric properties Cu2SnS3 thin films deposited by magnetron sputtering, *Advances in Materials Science and Engineering*, 2013.

Zhao, Y., Chang, L., Dong, X.-F., Zhang, H.-X., Li, Y. ve Chen, J.-B., 2020, Effect of Ag doping on the performance of Cu2SnS3 thin-film solar cells, *Solar Energy*, 201, 190-194.

Zheng, Z., Wang, J., Bi, P., Ren, J., Wang, Y., Yang, Y., Liu, X., Zhang, S. ve Hou, J., 2022, Tandem organic solar cell with 20.2% efficiency, *Joule*, 6 (1), 171-184.

Zhou, Z., Wang, Y., Xu, D. ve Zhang, Y., 2010, Fabrication of Cu2ZnSnS4 screen printed layers for solar cells, *Solar Energy Materials and Solar Cells*, 94 (12), 2042-2045.

Zhu, J., Lin, B., Sun, X., Yao, R., Shi, C. ve Fu, Z., 2005, Heteroepitaxy of ZnO film on Si (111) substrate using a 3C–SiC buffer layer, *Thin Solid Films*, 478 (1-2), 218-222.